

# UC San Diego

## UC San Diego Electronic Theses and Dissertations

### Title

Hybrid Structures of PbS Quantum Dots and Single Layer Graphene for the Photodetector:  
Interface and Architecture

### Permalink

<https://escholarship.org/uc/item/7fq869mc>

### Author

Ahn, Seungbae

### Publication Date

2021

Peer reviewed|Thesis/dissertation

UNIVERSITY OF CALIFORNIA SAN DIEGO

**Hybrid Structures of PbS Quantum Dots and Single Layer Graphene for the  
Photodetector: Interface and Architecture**

A dissertation submitted in partial satisfaction of the  
requirements for the degree Doctor of Philosophy

in

Nanoengineering

by

Seungbae Ahn

Committee in Charge:

Professor Oscar Vazquez-Mena, Chair  
Professor Prabhakar Bandaru  
Professor Ertugrul Cubukcu  
Professor David Fenning  
Professor Tse Nga Ng

2021

Copyright

Seungbae Ahn, 2021

All rights reserved

The Dissertation of Seungbae Ahn is approved, and it is acceptable in quality and form for publication on microfilm and electronically.

University of California San Diego

2021



## **DEDICATION**

To my family

## TABLE OF CONTENTS

<b>DISSERTATION APPROVAL PAGE .....</b>	<b>III</b>
<b>DEDICATION .....</b>	<b>IV</b>
<b>TABLE OF CONTENTS .....</b>	<b>V</b>
<b>LIST OF FIGURES.....</b>	<b>IX</b>
<b>LIST OF TABLES .....</b>	<b>XIV</b>
<b>ACKNOWLEDGEMENTS.....</b>	<b>XV</b>
<b>VITA.....</b>	<b>XVIII</b>
<b>ABSTRACT OF THE DISSERTATION.....</b>	<b>XXII</b>
<b>CHAPTER 1 INTRODUCTION .....</b>	<b>1</b>
1.1 Background .....	1
1.2 Hybrid structure of quantum dots and two-dimensional materials.....	5
1.3 Thesis objectives and outlines .....	8

<b>CHAPTER 2 OPTOELECTRONIC RESPONSE OF HYBRID PBS-QD/GRAPHENE PHOTODETECTORS.....</b>	<b>9</b>
2.1 Introduction.....	10
2.2 Experimental methods.....	12
2.3 Structural properties of PbS QDs.....	15
2.4 Optical properties of PbS QDs.....	18
2.5 Photoresponse of hybrid graphene – PbS photodetectors.....	23
<b>CHAPTER 3 MEASURING THE CARRIER DIFFUSION LENGTH IN QUANTUM DOT FILMS USING GRAPHENE AS PHOTOCARRIER DENSITY PROBE .....</b>	<b>32</b>
3.1 Introduction.....	33
3.2 Results and Discussion.....	33
3.3 Conclusions.....	49
3.4 Fabrication process.....	49
<b>CHAPTER 4 II -II INTERACTIONS MEDIATED PYRENE BASED LIGAND ENHANCED PHOTORESPONSE IN HYBRID GRAPHENE/PBS QUANTUM DOTS PHOTODETECTORS.....</b>	<b>51</b>

4.1 Introduction.....	51
4.2 Results and Discussion.....	58
4.3 Conclusion.....	73

**CHAPTER 5 ENHANCED CHARGE TRANSFER AND RESPONSIVITY IN HYBRID QUANTUM DOT/GRAPHENE PHOTODETECTORS USING ZNO AS INTERMEDIATE ELECTRON-COLLECTING LAYER ..... 79**

5.1 Introduction.....	79
5.2 Results and Discussion.....	82
5.2.1 Device Fabrication and Material Characterization .....	82
5.2.2 Charge Transfer to Gr .....	84
5.2.3 Photoresponse of PbS/Gr and PbS/ZnO/Gr Devices .....	89
5.2.4 Enhanced Photoresponsivity and Charge Collection .....	96
5.3 Conclusion.....	102

**CHAPTER 6 HIGH RESOLUTION PATTERNING OF PBS QUANTUM  
DOTS/GRAPHENE PHOTODETECTORS WITH HIGH RESPONSIVITY VIA  
PHOTOLITHOGRAPHY WITH TOP GRAPHENE LAYER TO PROTECT SURFACE  
LIGANDS..... 106**

6.1 Introduction..... 107

6.2 Results and Discussion..... 108

6.3 Conclusion..... 122

6.4 Experimental section..... 122

**BIBLIOGRAPHY ..... 126**

## LIST OF FIGURES

Figure 1 Photodetector depending on the spectral bands from UV, Vis, to the broad IR including NIR, SWIR, MWIR, LWIR, and FIR&THz can be useful various applications. <sup>[1]</sup> .....	1
Figure 2 Timeline showing the development of two dimensional materials and hybrid structure of quantum dots and two dimensional materials in photodetectors <sup>[14]</sup> .....	4
Figure 3 Operating mechanism for hybrid structure of quantum dots and two-dimensional materials .....	6
Figure 4 Structural models of hybrid structure of graphene and QDs.....	8
Figure 5. Schematics of hybrid Gr/QD device and operation. QDs absorb light and generate photocarriers. Single Layer Graphene (SLG) behaves as a p-type channel and PbS QDs as the n-type material, sending photoholes to graphene for current generation while photoelectrons accumulate in the QD film, generating a photogating effect. <sup>[13, 18, 34, 35]</sup> .....	11
Figure 6. 5 layers of 2.65 nm (left) and 3.16 nm (right) PbS QDs. Single coating layer of PbS QDs is ~30 to 35 nm, which is similar with the data from Ellipsometry.....	14
Figure 7. Optical images showing device geometry. Active area defined between electrodes is 100x500 $\mu\text{m}^2$ . .....	15
Figure 8. Structural information of PbS QDs.....	17
Figure 9. TEM size histograms for various PbO:OA ratio.....	18
Figure 10. Optical properties of PbS QDs of different sizes.....	21
Figure 11. Transmission data. (a) Transmission versus wavelength with different thickness. The transmission becomes decreased as thicker. Below first extinction peak, there is sinuous waves due to the interference. (b) Transmission versus thickness. ....	22
Figure 12. Refractive index (n,k) of QD films with QD sizes of d=2.65, 3.16, 3.90 and 4.96 nm as function of wavelength obtained by ellipsometry.....	22
Figure 13. Absorption coefficients. Comparison of absorption coefficients obtained by UV/Vis spectroscopy and by Ellipsometry showing show similar behaviors. ....	23
Figure 14. Photoresponse of hybrid Gr/QD photodetectors. ....	25

Figure 15 Time response fittings. Exponential fitting for response and recovery time for various QD size.....	26
Figure 16 I/V curves. I/V curves under $\lambda=635$ illumination for various powers and QD size.....	27
Figure 17 Effect of thickness.....	30
Figure 18 Light penetration and carrier diffusion.....	36
Figure 19 Absorption spectrum and TEM of PbS QDs.....	37
Figure 20 Device structure.....	39
Figure 21 SEM Cross sections.....	39
Figure 22 Photoresponse and charge transfer.....	41
Figure 23 Transconductance devices.....	42
Figure 24 Light penetration depths.....	43
Figure 25 Holes and electron diffusion length.....	46
Figure 26 a) Principle of operation in hybrid SLG/QD photoconductive detectors based on carrier photogeneration in QDs and charge transfer to SLG to produce a photocurrent under the bias voltage VDS across SLG.....	57
Figure 27 TEM micrographs of (a) OLEA- and (b) PBA-QDs.....	60
Figure 28 Raman spectra of SLG and OLEA-QDs onto SLG before and after treatment with TBAI.....	61
Figure 29 measurements (I vs VG @ VDS=1 V) for a) bare SLG (grey curve), after deposition of OLEA-QDs (blue curve), after TBAI ligand exchange (black curve), and under illumination ( $\lambda=635$ nm) (red curve), and b) SLG (grey curve), after deposition of PBAQDs (blue curve), after TBAI ligand exchange (black curve), and under illumination ( $\lambda=635$ nm).....	63
Figure 30 Models of the energy levels behavior trends depicted for SLG a) after deposition of OLEA-QDs, b) after TBAI ligand exchange, and c) upon illumination, on the basis of the transconductance measurements reported in Figure 29 (a) and relative QDs energy levels position from the references <sup>[13, 90-92]</sup> and for SLG d) after deposition of PBA-QDs.....	65

Figure 31 I/V measurements for bare SLG, SLG/OLEA/TBAI, and SLG/PBA/TBAI samples, showing reduction in conductance after QD deposition. ....	67
Figure 32 a) Photoresponse of the SLG/OLEA/TBAI and SLG/PBA/TBAI devices collected under ON/OFF light stimulation ( $\lambda=635\text{ nm}$ , $14.33\text{ mWcm}^{-2}$ , $V_{\text{bias}}=1\text{ V}$ ). ....	68
Figure 33 SLG/OLEA/TBAI rising time (Light OFF $\rightarrow$ ON) achieved by fitting the transient photocurrent time response of Figure 32. ....	70
Figure 34 SLG/OLEA/TBAI recovery time (Light ON $\rightarrow$ OFF) achieved by fitting the transient photocurrent time response of Figure 32. ....	70
Figure 35 SLG/PBA/TBAI rising time (Light OFF $\rightarrow$ ON) achieved by fitting the transient photocurrent time response of Figure 32. ....	70
Figure 36 PBA/TBAI recovery time (Light ON $\rightarrow$ OFF) achieved by fitting the transient photocurrent time response of Figure 32. ....	71
Figure 37 Raw data from the spectral response measurement. The current under 40 mV bias is measured for each wavelength step with an integration time of 10 s. ....	72
Figure 38 I/V curves of SLG/QD devices at different light intensities ( $\lambda=635\text{ nm}$ ) ....	73
Figure 39 a) I vs $V_G$ for a bare graphene sample, showing the Dirac peak at $V_{\text{DP}}\sim 90\text{ V}$ and that graphene is p-type. ....	83
Figure 40 a) Five layers of PbS QDs coated on 285 nm of $\text{SiO}_2$ . ....	84
Figure 41 a) PbS/Gr device schematics. ....	86
Figure 42 a) Resistance as a function of thickness for PbS/Gr and ZnO/Gr. For PbS/Gr the resistance increases from $R \approx 250$ to $900\ \Omega$ as the thickness increases from $t = 0$ to $120\text{ nm}$ . For ZnO/Gr the resistance increases from $R \approx 220\ \Omega$ to $500\ \Omega$ as the thickness increases from $t = 0$ to $35\text{ nm}$ but remains constant from $t = 35$ to $140\text{ nm}$ . ....	88
Figure 43. Full I vs $V_G$ curves for ZnO/Gr and PbS/Gr as function of ZnO and PbS thickness respectively from which $V_{\text{DP}}$ is extracted for Figure 42 ....	89
Figure 44 Current response under a $\lambda=635\text{ nm}$ laser of a ZnO/Gr structure, showing the zero response of the system since $\lambda = 635$ laser cannot create photocarriers in ZnO due to its high band gap. ....	92



Figure 45 a) $I_{ph}$ versus $V_G$ for PbS(30 nm)/Gr. At $V_G = 0$ , the photoresponse is positive due to photoholes transferred to p-type Gr. ....	93
Figure 46 Band diagrams of PbS/Gr and PbS/ZnO/Gr showing the shift in Fermi level under illumination for representative $V_G$ . ....	94
Figure 47 Time response for ON/OFF light switching for PbS/Gr and PbS/ZnO/Gr (a) with long time exposure (>1 hour), (b) and (c) 5 cycles, and (d) and (e) one cycle. Illumination: $\lambda=635$ nm and light frequency modulation: 10 mHz. ....	96
Figure 48 a) Responsivity as function of wavelength, showing a $10\times$ higher response for intercalated devices with ZnO. ....	99
Figure 49. Full set of I vs $V_G$ and I vs $V_{DS}$ plots for different light intensities for PbS/Gr and PbS/ZnO/Gr. This data is used to generate plots in Figure 48.(b and.c). ....	100
Figure 50. Dark current traces. The detectivity was calculated by $D = \Delta f \cdot ANEP$ , $NEP = \text{Noiserms}/R$ , $R = \text{Responsivity}$ , $A = 0.001 \text{ cm}^2$ , and $\Delta f = 20\text{Hz}$ ....	101
Figure 51 Schematic diagram of the patterning process for PbS CQDs using PGPL. ....	111
Figure 52 a) Optical images of patterned SLG. The length of SLG is 500, 200, and 100 $\mu\text{m}$ in first row from top to bottom, respectively, and 50, 20, and 10 $\mu\text{m}$ in second row, from top to bottom, respectively, and 5 $\mu\text{m}$ in third row and the width of all SLG channel is 100 $\mu\text{m}$ . b) Optical images of patterned PbS CQDs on patterned SLG. ....	112
Figure 53 (a) UV-vis absorption spectra of PbS CQDs without PGPL, showing the shift of a resonance peak from 930 nm to 895 nm. (b) UV-vis absorption spectra of PbS CQDs with PGPL, representing the shift of a resonance peak from 930 nm to 924 nm. (c) FTIR spectra of photoresist, pristine PbS CQDs, and the patterned PbS CQDs with and without PGPL. ....	113
Figure 54 Light is absorbed by QDs generating photocarriers, followed by charge separation. In the specific case of Gr and PbS-QDs, due to band alignment and interface built-in potential, electrons stay in the QDs while holes are transferred to graphene. The transferred holes change the graphene (p-type) conductivity while the electrons generate a photogating effect. ....	116
Figure 55 (a) Time response for on/off light switching for pristine PbS CQDs/patterned SLG, patterned PbS CQDs/SLG with PGPL, and without PGPL ( $V_{bias}= 5 \text{ V}$ , $\lambda=635 \text{ nm}$ , $17 \text{ mW}/\text{cm}^2$ ). (b) Responsivity as function of wavelength, showing the highest response for patterned PbS CQDs/SLG with PGPL (Hg-Xe lamp with monochromator). ....	117
Figure 56 The resistance of various lengths SLG before and after lithography process. ....	118

Figure 57 Photoresponse: PGPL before and after lithography. These results clearly show the use of lithography without the PGPL result in significant degradation of the photoresponse. Adding the PGPL with the top graphene layer after the lithography does not show any significant enhancement since the QD ligands are already damaged. .... 118

Figure 58 The 60-seconds time traces show the stability of the photoresponse. .... 118

Figure 59 (a) Optical images of 100  $\mu\text{m}$  by 100  $\mu\text{m}$  patterned SLG. .... 120

Figure 60 Calculation of detectivity at incident light power of  $1.6 \times 10^{-8}$  mW at 40, 10 and 2 Hz. 121

Figure 61 UV/Vis absorption and photocurrent before and after ligand exchange from oleic acid (OA) to TBAI. Ligand exchange is crucial to facilitate the charge transport along the QD film and therefore the charge collection by the SLG. .... 124

## LIST OF TABLES

Table 1 Current photodetector technologies and their wavelength range, advantage, and disadvantage .....	2
Table 2 Tunable bandgap depending on the size and composition of the materials .....	4
Table 3 Summary of penetration depth results .....	44
Table 4 Summary of diffusion length results .....	47
Table 5. Summary of recent reports on established advances on hybrid photodetectors combining 2D materials and QDs. Continued. ....	54
Table 6 Rise and Recovery times of SLG/OLEA/TBAI and SLG/PBA/TBAI devices. ....	71
Table 7 Comparison of responsivity for PbS based photodetectors. ....	103

## ACKNOWLEDGEMENTS

First of all, I would like to express my greatest appreciation to anyone who help and support my research while pursuing Ph.D. I would like to appreciate my advisor Professor Vazquez-Mena. Without his constant guidance over the years, this work would not be achieved successfully. I was enlightened and inspired by his profound knowledge, acute insights, intelligence, and deep understanding of sense of humor, the philosophy of research, and most importantly, passion for science.

I would like to thank my dissertation committee, Professor David Fenning, Professor Prabhakar Bandaru, Professor Ertugrul Cubukcu and Professor Tse Nga Ng for instructions and suggestions to improve this dissertation. I have learned a lot from Professor David Fenning and Professor Ertugrul Cubukcu, not only critical thinking for doing research but also to be creative.

I want to express my appreciation to my previous and current lab members at UC San Diego. Dr. Wenjun Chen, Dr. Jiaying Wang, Dr. Malcolm Lockett, Mr. Miguel Moreno, Ms. Ju Ying Shang, thanks for their collaborations and helps during my PhD period.

I am lucky to work and collaborate with many members with their support in University of Bari (Dr. Chiara Ingrosso, Dr. Marinella Striccoli, and Professor Lucia Curri), National Institute of Health (Dr. Bruce Hope), and Galianatechnology (Mr. Mark Wells and Mr. Gregory Sutton). The support from National Science Foundation Award No. 1710472 and No. 2046176 are gratefully acknowledged. I also would like to thank the KWANJEONG Fellowship from KWANJEONG Educational Foundation in South Korea, financial support, and training from being research and

teaching assistant at UCSD.

Most importantly, I would never have made through the tough times without the support from my parents, Mr. Sung-Gi Ahn and Mrs. Jum-Hwa Kim, and my wife, Somyi Kim, and, my brother, Sang-Bae Ahn, who are fully support believe in me with decision I made. Without my family, I cannot finish lots of challenges while pursuing doctoral degree. Also, I would like to thank my best friend, Jaewook Oh.

Chapter 2, in full, is a reprint of the material as it appears in “Optoelectronic response of hybrid PbS-QD/graphene photodetectors”. Seungbae Ahn, Hyeseung Chung, Wenjun Chen, Miguel A Moreno-Gonzalez, Oscar Vazquez-Mena, *The Journal of Chemical Physics*, 151, 23, 234705 (2019). The dissertation author was the primary investigator and author of this paper.

Chapter 3, in full, is a reprint of the material as it appears in “Measuring the carrier diffusion length in quantum dot films using graphene as photocarrier density probe”. Seungbae Ahn and Oscar Vazquez-Mena. Submitted. The dissertation author was the primary investigator and author of this paper.

Chapter 4, in full, is a reprint of the material as it appears in “ $\pi$ - $\pi$  Interactions Mediated Pyrene based Ligand Enhanced Photoresponse in Hybrid Graphene/PbS Quantum Dots Photodetectors”. Seungbae Ahn, Chiara Ingrosso, Annamaria Panniello, Marinella Striccoli, Giuseppe Valerio Bianco, Angela Agostiano, Giovanni Brunoc, Maria Lucia Curri, and Oscar Vazquez Mena, *Advanced Electronic Materials*, Accepted. The dissertation author was the primary investigator and author of this paper.

Chapter 5, in full, is a reprint of the material as it appears in “Selectively Electron-transport from PbS quantum dots to single layer graphene with ZnO intermediate layer with Ultrahigh Responsivity”. Seungbae Ahn, Miguel Angel Moreno Gonzalez, Wenjun Chen, Malcolm Lockett, Jiaying Wang, Oscar Vazquez-Mena, *Advanced Electronic Materials* 2020, 6 (6), 2000014. The dissertation author was the primary investigator and author of this paper.

Chapter 6, in full, is a reprint of the material as it appears in “High resolution patterning of PbS quantum dots/Graphene photodetectors with high responsivity via photolithography with graphene passivation layer”, Seungbae Ahn, Wenjun Chen, and Oscar Vazquez-Mena, *Nanoscale advance*, accepted. The dissertation author was the primary investigator and author of this paper.

## VITA

### EDUCATION

**University of California San Diego** Sep. 2017 – Dec. 2021

- Ph.D in Nanoengineering, GPA 3.255/4.0

**Inha University, South Korea** Sep. 2013 – Feb. 2016

- Master degree in Environmental Engineering, GPA 4.0/4.0

**Univesrity of Ulsan, South Korea** Mar. 2007 – Feb. 2013

- B.S degree in Electrical and electronic engineering, GPA 4.27/4.5

### RESEARCH EXPERIENCE

#### **Graduate researcher**

Oscar Vazquez-Mena Lab, *University of California, San Diego* Sep. 2017 – Dec. 2021

*Multispectral photodetector device research project*

- Understanding the behavior of photo-excited carriers on hybrid structure of quantum dots and graphene
- Develop the multispectral photodetectors using intercalated graphene layers

#### **Graduate researcher**

Ki-Joon Jeon Lab, *Inha University, South Korea* Mar. 2013 – Aug. 2017

*Graphene research project*

- Hybrid structure of Inorganic and single layer graphene for gas sensors
- Understanding atomic glues on single layer graphene surface

#### **Researcher**

Smart Sensor Research Center, *Korea Electronics Technology Institute (KETI)*, South Korea

Mar. 2013 – Feb. 2014

*Smart sensor fabrication project*

- Fabrication of Microsensors with a heater

## PROFESSIONAL EXPERIENCE

### **University of California San Diego**

Spring 2018/2019, and Fall 2020

- Teaching Assistant for two dimensional materials.

### **Inha University, South Korea**

2013/2014/2015

- Teaching Assistant for Advanced Air pollution control design.

### **University of Ulsan, South Korea**

2013/2014/2015

- Teaching Assistant for Basic Electrical Engineering Lab.
- Teaching Assistant for Electromagnetic Field Theory

## PATENT

- Inserting interlink atom between hard and soft materials for better performance, Korea Patent, No.1020150100445
- Synthesis of large area single layer graphene oxide, Korea Patent, No. 1020150100443
- Migration of oxygen adatom on single layer graphene oxide for modifying its properties” Korea Patent, No. 1020150100444

## PUBLICATION

- **Seungbae Ahn** and Vazquez-Mena Oscar, “Measuring the carrier diffusion length in quantum dot films using graphene as photocarrier density probe”, The Journal of Chemical Physics, Under Review.
- **Seungbae Ahn**, Wenjun Chen, and Vazquez-Mena Oscar, “High resolution patterning of PbS quantum dots/Graphene photodetectors with high responsivity via photolithography with graphene passivation layer”, Nanoscale advanced, Accepted.
- **Seungbae Ahn**, Chiara Ingrosso, Annamaria Panniello, Marinella Striccoli, Giuseppe Valerio Bianco, Angela Agostiano, Giovanni Brunoc, Maria Lucia Curri, and Oscar Vazquez Mena., “ $\pi$ - $\pi$  Interactions Mediated Pyrene based Ligand Enhanced Photoresponse in Hybrid Graphene/PbS Quantum Dots Photodetectors”, Advanced Electronic Materials, Accepted.
- Lockett, Malcolm; Sarmiento, Viviana; Gonzalez, Matthew; **Ahn, Seungbae**; Wang, Jiaying; Liu, Ping; Vazquez-Mena, Oscar, “Ultrathin 5-micron thick silicon nanowires intercalated with reduced graphene oxide binderless anode for lithium-ion batteries”, ACS applied Energy Materials, 2021.



- Mai, H, Jeong, S, Nguyen, T, Youn, J, **Seungbae Ahn**, Park, C, Jeon, K. “Pd Nanocluster/Monolayer MoS<sub>2</sub> Heterojunctions for Light-Induced Room-Temperature Hydrogen Sensing”, ACS Appl. Mater. Interfaces 2021.
- Nguyen, T, Jeong, S, Youn, J, **Seungbae Ahn**, Nam, K, Park, C, Jeon, K. “Insight into mechanism of temperature-dependent limit of NO<sub>2</sub> detection using monolayer MoS<sub>2</sub>”, Sensors and Actuators: B. Chemical, 2021.
- E. Contreras, C. Palacios, B. Huerta, **Seungbae Ahn**, O. Vazquez-Mena, R. D. Cadena-Nava, G. Alonso-Nunez, O. E. Contreras, M. T. Oropeza-Guzmán, and J. M. Romo-Herrera. “Anodes for Direct Alcohol Fuel Cells Assisted by Plasmon-Accelerated Electrochemical Oxidation Using Gold Nanoparticle-Decorated Bucky papers”, ACS Appl. Energy Mater. 2020.
- **Seungbae Ahn**, Miguel Angel Moreno Gonzalez, Wenjun Chen, Malcolm Lockett, Jiaying Wang, Oscar Vazquez-Mena, “Selectively Electron-transport from PbS quantum dots to single layer graphene with ZnO intermediate layer with Ultrahigh Responsivity”, Adv. Electron. Mater. 2020.
- Wenjun Chen, **Seungbae Ahn**, Marquez Balingit, Jiaying Wang, Malcolm Lockett, Oscar Vazquez-Mena, “Near full light absorption and full charge collection in 1-micron thick quantum dot photodetector using intercalated graphene monolayer electrodes”, Nanoscale, 2020.
- **Seungbae Ahn**, Hyeseung Chung, Wenjun Chen, Miguel A Moreno-Gonzalez, Oscar Vazquez-Mena, “Optoelectronic response of hybrid PbS-QD/graphene photodetectors”, The Journal of Chemical Physics, 2019.
- Viviana Sarmiento, Mercedes Teresita Oropeza-Guzmán, Malcolm Lockett, Wenjun Chen, **Seungbae Ahn**, Jiaying Wang, Oscar Vazquez-Mena, “Electrochemical functionalization strategy for chemical vapor deposited graphene on silicon substrates: grafting, electronic properties and biosensing”, Nanotechnology, 2019.
- Wenjun Chen, **Seungbae Ahn**, Carlos Rangel, Oscar Vazquez Mena, “Implementation of Metallic Vertical Interconnect Access in Hybrid Intercalated Graphene/Quantum Dot Photodetector for Improved Charge Collection”, Frontiers in Materials, 2019.
- Wenjun Chen, Joshua Castro, **Seungbae Ahn**, Xiaochen Li, Oscar Vazquez-Mena, “Improved Charge Extraction Beyond Diffusion Length by Layer-by-Layer Multistacking Intercalation of Graphene Layers inside Quantum Dots Films”, Advanced Materials, 2019.
- Sang Yeon Lee, Jinseo Kim, **Seungbae Ahn**, Ki-Joon Jeon, Hyungtak Seo, “Complementary Schottky diode formation with carbon buffer and p-doped single layer graphene on intrinsic SiC via fluorine intercalation”, Carbon, 2019.
- Young Ho Kim, Phan Duy Thach, **Seungbae Ahn**, Ki-Hun Nam, Cheol-Min Park, and Ki-

- Joon Jeon , “Two-dimensional SnS<sub>2</sub> materials as high-performance NO<sub>2</sub> sensors with fast response and high sensitivity”, *Sensors and Actuators B: Chemical*, 2018.
- **Seungbae Ahn**, K. Vijayarangamuthu, and Ki-Joon Jeon, “Morphological control of zinc oxide nanostructure on single layer graphene”, *Journal of Nanoscience and Nanotechnology*, 2016.
  - Vijayarangamuthu Kalimuthu, **Seungbae Ahn**, Hyungtak Seo, SangHee Yoon, Cheol-Min Park, and KiJoon Jeon, “Temporospatial control of graphene wettability”, *Advanced Materials*, 2016. \*Inside Cover Page.
  - Myeong-Ho Kim, Young-Ahn Lee, Jinseo Kim, Jucheol Park, **Seungbae Ahn**, Ki-Joon Jeon, JeongWon Kim and Duck-Kyun Chol, and Hyungtak Seo, “Photochemical Hydrogen Doping Induced Embedded Two-Dimensional Metallic Channel Formation in InGaZnO at Room Temperature”, *ACS Nano*, 2015.
  - Arunkumar Rengaraj, Yuvaraj Haldorai, B Cheol, Hwan Kwak, **Seungbae Ahn**, Ki-Joon Jeon, Seok Hoon Park, Young-Kyu Han, and Yun Suk Huh, “Electrodeposition of flower-like nickel oxide on CVD-grown graphene to develop an electrochemical non-enzymatic biosensor”, *Journal of Materials Chemistry B*, 2015.
  - Heeyoung Jeon, Jingyu Park, Woochool Jang, Hyunjung Kim, **Seungbae Ahn**, Ki-Joon Jeon, Hyungtak Seo, and Hyeongtag Jeon, “Detection of oxygen ion drift in Pt/Al<sub>2</sub>O<sub>3</sub>/TiO<sub>2</sub>/Pt RRAM using interface-free single-layer graphene electrodes”, *Carbon*, 2014.
  - Hyungtak Seo, **Seungbae Ahn**, Jinseo Kim, Young-Ahn Lee, Koo-Hyun Chung, and Ki-Joon Jeon, “Multi-resistive Reduced Graphene Oxide Diode with Reversible Surface Electrochemical Reaction induced Carrier Control”, *Scientific Reports*, 2014.

#### **HONORS, AWARDS, AND SCHOLORSHIP**

- KWANJEONG FELLOWSHIP 2017 – 2021
- Honor Student, Inha University Graduate School 2016
- Honor Student, University of Ulsan 2011 – 2013

## ABSTRACT OF THE DISSERTATION

Hybrid Structures of PbS Quantum Dots and Single Layer Graphene for The Photodetector:

Interface and Architecture

by

Seungbae Ahn

Doctor of Philosophy in Nanoengineering

University of California San Diego, 2021

Professor Oscar Vazquez-Mena, Chair

Photodetectors that convert light to electrical signals are useful for understanding lots of information containing in the specific wavelength of the light. Depending on the spectral bands, the photodetectors can be used for pollution detection, imaging, bioimaging, telecommunication, chemical analysis, night vision, medical imaging, gas sensing, and astronomy observations. To sense

the above-mentioned signals, the photodetectors with good photon absorption and high charge collection efficiency are required. Quantum dots are promising materials for the photodetectors because of their strong light absorption, direct and size tunable band gap properties, but quantum dots have very poor carrier mobility leading to low charge collection efficiency. Two-dimensional materials such as single layer graphene and MoS<sub>2</sub> have shown extraordinarily high mobilities, but one or few atoms thickness are ultrathin, resulting in poor photon absorption. As a result, novel strategy to overcome such limitations was demonstrated by integrating hybrid quantum dots and two-dimensional materials. The hybrid structure takes advantage of the synergy between two materials, combining the high mobility of two-dimensional materials for collecting charge efficiently, as well as the strong photon absorption and bandgap tunability of quantum dots for carrier photogeneration.

The focus of this dissertation is to understand the hybrid structure of PbS quantum dots and single layer graphene for high performance photodetectors by investigating the interface and structures. We found that the spectral photoresponse of the hybrid structure can be controlled by the size or thickness of PbS quantum dots. Also, we have presented an effective technique to measure the diffusion length of both holes and electrons in the bulk of thick quantum dots. Moreover, we engineered the interface between quantum dots and graphene with pyrene molecules to enhance the coupling between graphene and quantum dots via  $\pi$ - $\pi$  interactions. In addition, we controlled the carrier transfer from PbS quantum dots to graphene via ZnO electron transporting layer. Finally, we successfully fabricated micron size PbS quantum dot patterning on graphene for integrated photodetector chips.

This dissertation demonstrates the fundamental understanding of hybrid structure of quantum dots and graphene. The research results can help to promote technologies and push the limits in hybrid structure of quantum dots and graphene for optoelectronic research area.

# Chapter 1

## Introduction

### 1.1 Background

Light delivers information. The detection for a specific wavelength from gamma ray to long radio waves can be useful for understanding information of the light. The various applications such as pollution detection, imaging, bioimaging, telecommunication, astronomy observations, night vision, chemical analysis, thermal imaging, and medical imaging can be used depending on the spectral bands shown in Figure 1.<sup>[1]</sup> Therefore, the high-performance photodetector, which converts light to electronic signal, is required.

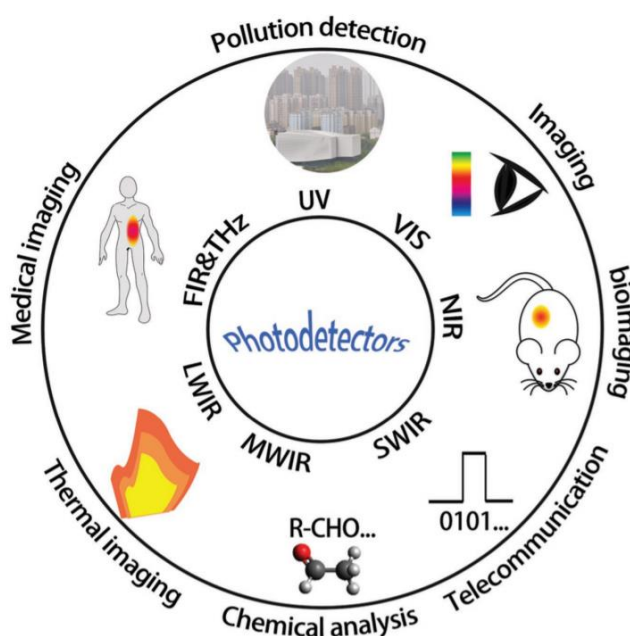


Figure 1 Photodetector depending on the spectral bands from UV, Vis, to the broad IR including NIR, SWIR, MWIR, LWIR, and FIR&THz can be useful various applications.<sup>[1]</sup>

There are currently developed photodetector technologies based on silicon (Si), germanium (Ge), indium gallium arsenide (InGaAs), and mercury cadmium telluride (HgCdTe) materials shown in Table 1.<sup>[2, 3]</sup> Si-based photodetectors are widely used because of their monolithic integrability with the low-cost complementary metal oxide semiconductor technologies, but their detection limit is around 900 nm due to an absorption cutoff wavelength of ~1100 nm, which is relatively large band gap of 1.1 eV. Ge-based photodetectors are one of the candidates to detect longer wavelength (~1800 nm) due to higher optical absorption and lower band gap than Si, but there is a lattice mismatch between Si and Ge challenging obstacle towards monolithic integration. II-VI and III-V compound semiconductors such as HgCdTe and InGaAs are recently promising materials because the detection spectral bands can be extended from UV to the IR region depending on an appropriate material composition, as well as they have high optical absorption due to direct band gap and high carrier mobility, but Ga material is expensive and Hg–Te bond is weak and instable, which is an issue for uniformity.

Table 1 Current photodetector technologies and their wavelength range, advantage, and disadvantage

<b>Materials</b>	<b>Wavelength range</b>	<b>Advantage</b>	<b>Disadvantage</b>
Si	200 – 1100 nm	Good integrability	Limited spectral range
Ge	800 – 1800 nm	High optical absorption	Bad integrability
InGaAs	800 – 1700 nm	Tunable spectrum	Expensive
HgCdTe	2,000 – 20,000 nm	Suitable for longer wavelength	Bad uniformity

Inspired by nanoscience and nanoengineering, various nanomaterials with outstanding electronic and optical properties are emerging for next generation photodetector devices because nanoscale elements such as quantum dots (QDs), layered structures, and nanowires can be manufactured for high performance photodetectors, which exhibit high sensitivity, fast response,

miniaturization potential, high responsivity, and low noise.<sup>[4]</sup> QDs are one of the candidate materials for next generation photodetectors because they offer size-tunable bandgap, easy and low-cost solution-based processing, strong light absorption, and extended wavelength range depending on an appropriate material composition. Due to quantum confinement effect, the bandgap of QDs is dependent on the size and composition of the materials shown in Table 2.<sup>[5, 6]</sup> However, the implementation of QDs into high performing photodetectors faces a significant challenge due to low carrier mobility by the colloidal system. Unsaturated surface atoms of QDs cause to create the dangling bonds, leading to the formation of intermediate states of varying energies near bandgap.<sup>[7]</sup> This may generate various phenomena in QDs such as the formation of midgap trap density, which results in reducing charge carrier mobility, decrease the carrier lifetime, and enhance the recombination of photoexcited carriers. The other candidates for high performance photodetectors are two-dimensional (2D) materials such as MoS<sub>2</sub> and single layer graphene. Recently, single layer MoS<sub>2</sub> has been developed for ultrasensitive photodetectors because of its direct bandgap with a high absorption coefficient, efficient hole-electron pair generation, and high carrier mobility.<sup>[8]</sup> Nonetheless, it is ultrathin, resulting in poor light absorption, and becomes indirect bandgap as thickness thicker. To overcome such limitations of QDs and 2D materials, a novel strategy has been demonstrated by combining two emerging materials into a hybrid structure of QDs and 2D materials for high performance photodetectors shown in Figure 2.<sup>[9-13]</sup>



Table 2 Tunable bandgap depending on the size and composition of the materials

Quantum dots	Size range (nm)	Bandgap range (eV)	Bandgap in bulk (eV)
CdS	2.6 – 5.6	2.49 – 2.78	2.42
CdSe	2.27 – 3.75	2.14 – 2.52	1.74
PbS	1.5 – 5	0.8 – 2.5	0.41
PbSe	8 – 17	0.35 – 0.50	0.28
HgTe	4.8 – 9.6	0.25 – 0.52	~0

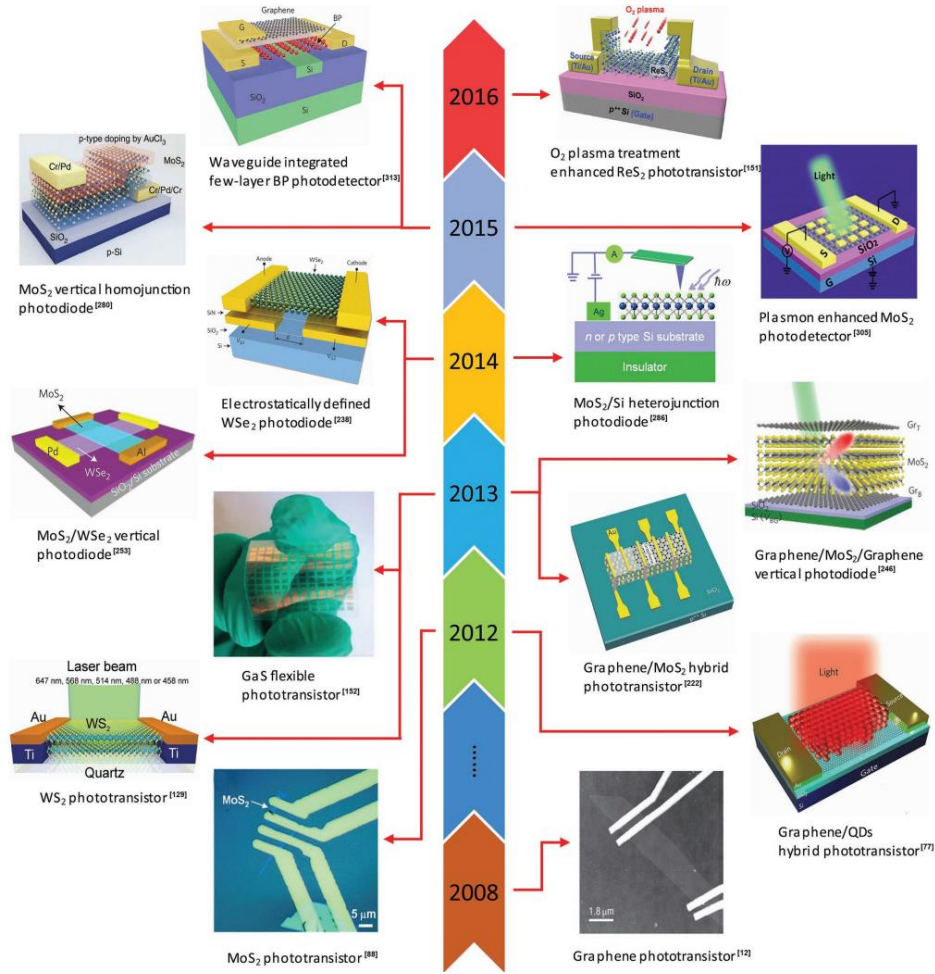


Figure 2 Timeline showing the development of two dimensional materials and hybrid structure of quantum dots and two dimensional materials in photodetectors<sup>[14]</sup>

## 1.2 Hybrid structure of quantum dots and two-dimensional materials

Hybrid structure of QDs and 2D materials has the synergistic effects between these two materials. As mentioned before, QDs provide strong light absorption for carrier generation under the illumination with tunable bandgap, and 2D materials offer a high carrier mobility to collect photoexcited carriers efficiently. Hybrid structure of QDs and 2D materials benefits from both materials that are high light absorption in QDs and high carrier mobility in 2D materials. The operational mechanism of hybrid structure is similar to the field effect transistor (FET). FET uses an electrical potential to control the current flow by manipulating the density of carriers in a channel, and, for hybrid structure, the photoexcited carriers in QDs influence the carrier density in two dimensional materials. Under light illumination, QDs absorb the light, which creates the photoexcited carriers. Spatial separation of carriers in hybrid structure prohibits a fast recombination of photoexcited carriers because of their band structure. At the interface between QDs and 2D materials, an equilibrium condition is reached that built-in potential occurs. It leads to a vertical photo-doping effect. One of photoexcited holes or electrons transfer from QDs to 2D materials depending on the band structure, and the other carrier is trapped in QDs. The transferred holes or electrons from QDs flow laterally through the channel in two dimensional materials shown in Figure 3.<sup>[15]</sup> As long as the electrons (holes) stay trapped within the QDs, holes (electrons) can recirculate in 2D materials and generate gain. In hybrid structure of QDs and 2D materials for photodetector applications, the phenomenon called gain is an important factor to optimize the performance of the photodetectors. If the lifetime, which is caused by a trapped carrier in QDs, is longer than the transit time of free carriers in two dimensional materials, photoconductive gain is generated. It can lead to

a large responsivity because more than a carrier per photon contribute to the current flow but cause slow response time due to trapped carriers.

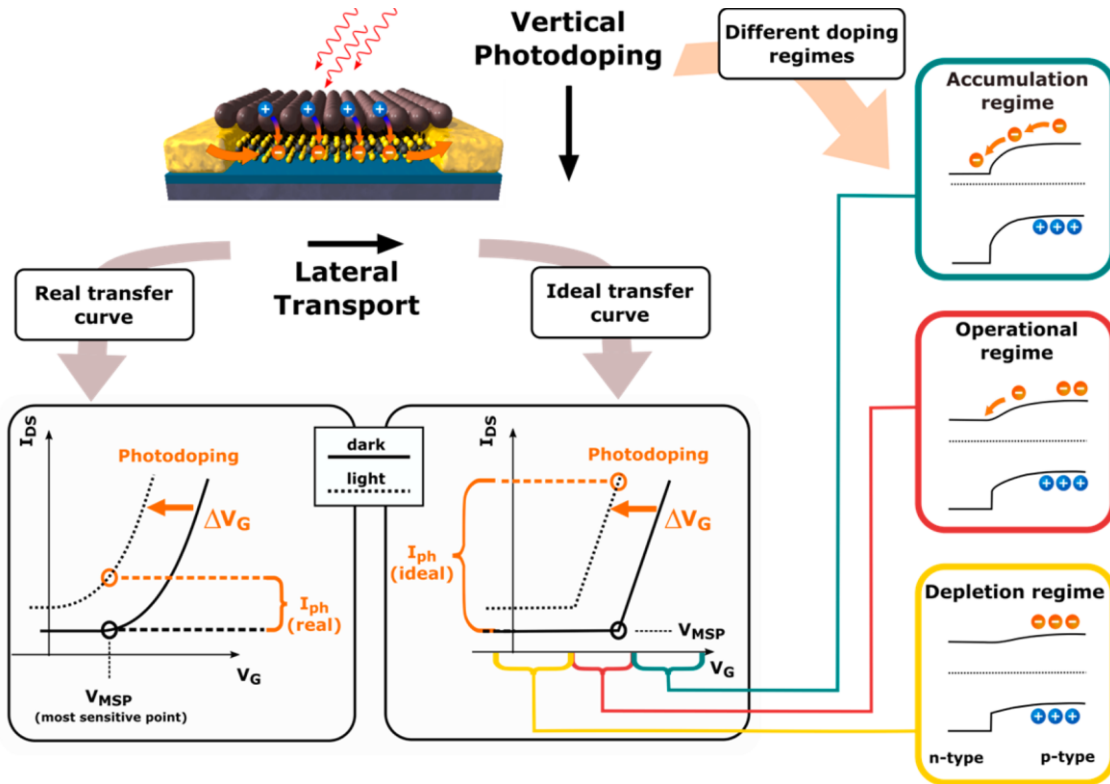


Figure 3 Operating mechanism for hybrid structure of quantum dots and two-dimensional materials

Single layer graphene is one of the most promising materials as a photoexcited carrier transport layer for hybrid structure photodetectors because of its unique properties such as high transparency and superior carrier mobility compared to other 2D materials such as MoS<sub>2</sub>. Even though MoS<sub>2</sub> is a large and direct bandgap, which leads to low dark current and high absorption coefficient, it is not suitable for hybrid structure because limited manipulation of the interface and architecture. For example, first single layer MoS<sub>2</sub> exhibits a photoresponsivity of 7.5 mA/W due to

poor quality of the contact between metal and MoS<sub>2</sub>, and the photoresponsivity is enhanced to 880 A/W after improving the quality between contacts at the interface to reduce the trap states.<sup>[8, 16]</sup> However, there are several issues for engineering the interface of MoS<sub>2</sub>. MoS<sub>2</sub> layers can have several different phases, and phase engineering is difficult to control reliably in one atom thickness. Also, chemical doping methods on MoS<sub>2</sub> to reduce the trap density are difficult to control. Moreover, MoS<sub>2</sub> can be used for photodetector transistor architecture due to limited manufacturing skills. On the other hand, graphene is well studied for the interface engineering and architecture design.<sup>[17]</sup> The bandgap of graphene can be easily manipulated by doping of atomic or molecular bonding. Also, graphene can be used for many structural models such as anchored, wrapped, encapsulated, sandwich-like, layered, and mixed models to transport photoexcited carriers from QDs shown in Figure 4 as a conductive network. For example, the quantum efficiency of hybrid structure of single layer graphene and PbS QDs is 25 percent, but it can be increased in the structure of sandwich-like model to 90 percent.<sup>[13, 18]</sup> The diffusion length of PbS QDs is between 150 – 200 nm, so it is not sufficient to absorb most incoming light, which leads to low quantum efficiency. With multiple intercalated graphene between QDs, the photoexcited carriers are collected in each graphene layers. Finally, photoexcited carriers from the any QDs can be transferred to graphene channel regardless of bandgap of the materials without blocking the transfer of photoexcited carriers.<sup>[12, 19]</sup>

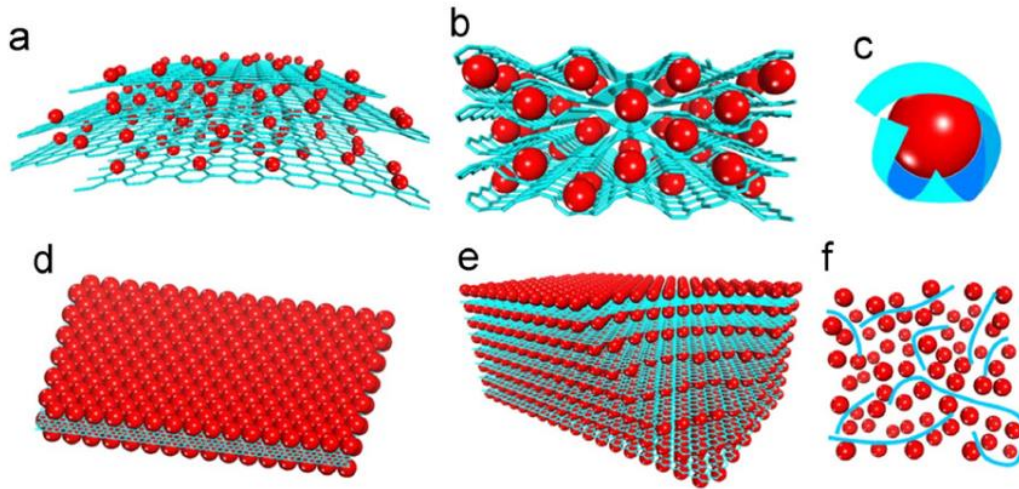


Figure 4 Structural models of hybrid structure of graphene and QDs.

### 1.3 Thesis objectives and outlines

The main objective in this dissertation is to investigate the possibilities of hybrid structure of PbS QDs and single layer graphene for photodetectors. Synthesis of PbS QDs, structure characterization, device fabrication, and performance testing are included in this dissertation.

Chapter 2 will present the fundamental optoelectronic properties of the hybrid structure of PbS QDs and SLG depending on the size and thickness of QDs. An effective method to calculate the diffusion length of photoexcited holes and electrons will be investigated in chapter 3. Chapter 4 will discuss a novel strategy tailoring the surface ligands at the interface and between QDs. Chapter 5 will present the control of photoexcited carriers depending on the structural configuration. Chapter 6 will show the patterning technique to fabricate high resolution photodetector array.

### Optoelectronic response of hybrid PbS-QD/graphene photodetectors

Lead sulfide quantum dots (QDs) have been widely used for various optoelectronic devices due to their high absorption coefficient and tunable bandgap. However, the low mobility of QD films results in poor charge collection and device performance. By combining QDs with graphene into hybrid graphene/QD photodetectors, photocarriers from QDs are transferred to graphene, improving charge collection and transport, drastically increasing the photoresponsivity. Herein, we carry a systematic analysis on how critical tuning parameters such as QD size and QD film thickness affect responsivity, spectral response, and time response. We report the absorption coefficient, refractive index ( $n$ ,  $k$ ), penetration depth, and energy bandgap of PbS QDs of different sizes. We study systematically how the photocurrent, photoresponsivity, time response, and power density dependence vary with QD size in hybrid Gr/QD. The bandgap of lead sulfide quantum dots was size-tuned between 0.86 and 1.39 eV. The time response shows that subsecond modulation can be achieved for different QD sizes with a responsivity up to  $10^7$  A/W at power densities of  $10^{-5}$  mW/cm<sup>2</sup>. We also studied how the performance of the photodetectors is affected by the thickness, discussing the limitations on the thickness by the compromise between light absorption and charge collection. We describe how the optical response shifts toward the infrared as QD films get thicker. Time responses below 1 s are obtained for graphene/QD devices with thickness from 150 nm to 1  $\mu$ m. This systematic study provides important guidelines to design hybrid graphene/QD photodetectors and tune their spectral response and performance.

## 2.1 Introduction

Quantum dots (QDs) are semiconducting optoelectronic nanoparticles that offer significant advantages over their bulk versions due to quantum confinement.<sup>[20, 21]</sup> QDs have shown very high extinction coefficient and tunable bandgap.<sup>[22, 23]</sup> They have been used as active materials in solar cells, light-emitting diodes, and photodetectors in both electronic and medical applications.<sup>[21, 24, 25]</sup> In particular, lead sulfide (PbS) QDs have been widely used due to their high absorption coefficient, direct bandgap, wide spectral range, chemical stability, and affordable synthesis using the hot-injection method.<sup>[6, 26, 27]</sup> PbS QDs have been used for both photodetection and luminescence in the infrared range.<sup>[23, 28]</sup> PbS QDs have also been used for high-resolution *ex vivo* and *in vitro* bioimaging, allowing for the acquisition of deep imaging inside biological tissues.<sup>[29]</sup> PbS QDs have been utilized as active materials in solar cells because of their high visible (vis)-IR light absorption and high chemical stability.<sup>[27, 30]</sup> The power conversion efficiency of PbS QD solar cells has gradually increased to surpass 10%.<sup>[31-33]</sup>

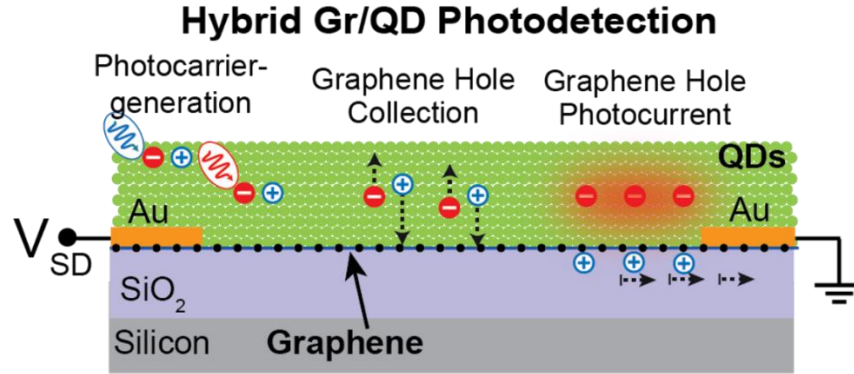


Figure 5. Schematics of hybrid Gr/QD device and operation. QDs absorb light and generate photocarriers. Single Layer Graphene (SLG) behaves as a p-type channel and PbS QDs as the n-type material, sending photoholes to graphene for current generation while photoelectrons accumulate in the QD film, generating a photogating effect.<sup>[13, 18, 34, 35]</sup> The device is built on SiO<sub>2</sub>/Si chips with the prepatterned electrodes.

Recently, hybrid photodetectors combining PbS QDs with single layer graphene (SLG) showed excellent performance reaching a high responsivity ( $>10^7$  A/W).<sup>[13, 15]</sup> This system combines and compensates the advantages and limitations of both nanomaterials. QDs have strong and size tunable light absorption with direct bandgap resulting in high carrier photogeneration, but their charge confinement and nanoparticle composition results in films with very poor conductivity, strongly limiting charge collection and transport.<sup>[36, 37, 38, 39]</sup> On the other hand, graphene has the highest mobility and excellent electrical conductivity, but its one-atom thickness severely limits its light absorption and practical application as an active material in solar cells or photodetectors. The hybrid Gr/QD configuration allows a synergy between materials, using QDs for light absorption to generate photocarriers that are then transferred to graphene for efficient charge transport and photocurrent generation. The Gr/QD device and operation is shown in Figure 5. The operational principle is that under illumination, PbS QDs transfer photoexcited holes to the Gr channel, which



leads to an increase in the hole density of typically p-type graphene on the SiO<sub>2</sub>/Si substrate, leading to an increase in conductivity.<sup>[34]</sup>

In this work, we present a systematic study on how the two main tunable parameters of QD size and QD film thickness affect the spectral response, responsivity, and time response of hybrid PbS QDs and graphene (Gr) photodetectors. Previous reports have focused on maximizing the photoresponse; however, the effect of QD size and film thickness has been not studied in detail. This information is critical to understand and optimize the operation of hybrid Gr/QD photodetectors. We study QD sizes from  $d = 2.65$  nm ( $\lambda = 805$  nm) to  $4.96$  nm ( $\lambda = 1350$  nm), covering a broad spectral response from the visible to the near IR and analyzing how the QD size affects the photoresponsivity of the devices.<sup>[39]</sup> We describe the synthesis of QDs of different sizes, their structural and optical properties, and the fabrication of hybrid Gr/QD devices. We study the spectral and time response as well as the effect of power density. Finally, we also study the effect of thickness on the photoresponse, which provides an alternative way to tune the spectral response of Gr/QD devices.

## 2.2 Experimental methods

PbS QDs synthesis: 0.94 g of lead oxide (PbO) was dissolved in 25 ml of 1-octadecene (ODE) with different concentrations of oleic acid (2.98, 7.45, 11.92, 19.37, and 35.76 ml) to achieve various sizes of PbS QDs.<sup>[40]</sup> After that, it was degassed under vacuum at 90 °C for 2 h to be dissolved. When the color of the solution becomes clear, 420  $\mu$ l of bis(trimethylsilyl) sulfide dissolved in 12.8 ml of ODE was injected into the solution. Next, we waited for 30 s for the reaction to be done and then cooled down by placing the flask in water. The PbS QDs were separated from the raw solution by centrifugation, followed by cleaning with toluene and acetone, and then

dissolved in toluene. The PbS QD solution was filtered with a 0.25  $\mu\text{m}$  pore size filter.

Graphene transfer: Single layer graphene on copper coated with poly-methyl methacrylate (PMMA) was purchased from Graphenea (Spain) and transferred by the wet method using PMMA as the supporting layer.<sup>[41]</sup> The copper layer was removed by wet etching using an ammonium persulfate solution. After the copper layer was completely etched, the transparent PMMA/graphene layer was transferred to deionized (DI) water to remove Cu etching residues. Then, the graphene layer was transferred onto an Au patterned electrode  $\text{SiO}_2/\text{Si}$  substrate and dried for 2 h at room temperature. Finally, PMMA was removed by acetone and cleaned with isopropyl alcohol and DI water.

Material characterization: The absorption and transmission of PbS QDs were measured by UV-vis spectroscopy (UH4150, Hitachi). The crystallographic phase of PbS quantum dots was investigated by X-ray diffraction (XRD) (Smartlab, Rigaku) equipped with Cu  $K\alpha$  radiation. The refractive index and extinction coefficient of PbS quantum dots were analyzed by an ellipsometer (M-2000D, J. A. Woollam). The size of PbS QDs was analyzed by transmission electron microscopy (TEM), and the images were recorded on a field emission gun JEOL-2800 at 200 kV with the Gaten OneView Camera, installed at the UC Irvine Materials Research Institute (IMRI). The average diameter of the particle size was analyzed using Image J software.

Device fabrication: PbS quantum dot films were prepared by a spin coating method. 0.1 ml of PbS quantum dots in toluene was deposited on the substrate by spin coating at 2500 rpm for 10 s. Next, 0.03M tetrabutylammonium iodide (TBAI) solution in methanol was added for ligand exchange by incubation for 30 s and followed by cleaning in methanol. The concentration of PbS

QD solutions for spin coating was 60, 50, 50, 40, and 30 mg/ml for QD sizes of  $d = 2.65, 3.16, 3.62, 3.9,$  and  $4.96$  nm, respectively. The SEM cross sections of the QD films are shown in Figure 6. Their respective thickness for a single coating layer was 30, 30, 30, 17, and 14 nm measured by the ellipsometry. For Gr/QD photodetectors, QDs were deposited on Gr layers on Si/SiO<sub>2</sub> chips with the prepatterned Au electrodes. The active area of the photodetectors is defined by the area between electrodes, which have a width of 500  $\mu\text{m}$  and are separated by 100  $\mu\text{m}$ .

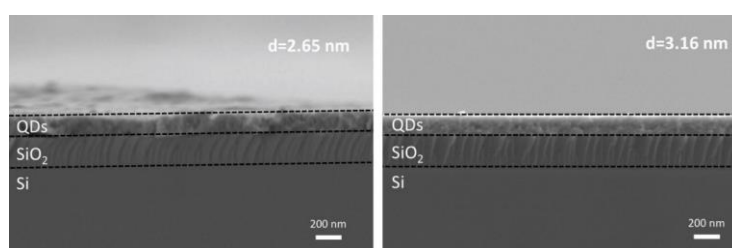


Figure 6. 5 layers of 2.65 nm (left) and 3.16 nm (right) PbS QDs. Single coating layer of PbS QDs is  $\sim 30$  to  $35$  nm, which is similar with the data from Ellipsometry.

The optical images of the Gr/QD devices are shown in Figure 7 of the supplementary material. Optoelectronic characterization: The light power of a 635 nm laser diode (CPS635R, Thorlabs) was measured with a standard silicon photodetector (S120VC, Thorlabs). The power intensity of the 635 nm laser diode was achieved by absorptive neutral density filters (NE503A, NE510A, NE520A, and NE530A, Thorlabs). Current vs voltage and current vs time data were measured using a Keithley 2400 source meter. The spectral response was measured using a Keithley 2400 source meter under a xenon lamp and filters (66485-500HX-R1, USFW-100, Newport) with a monochromator (CS260-RG-3-FH-D, Newport).

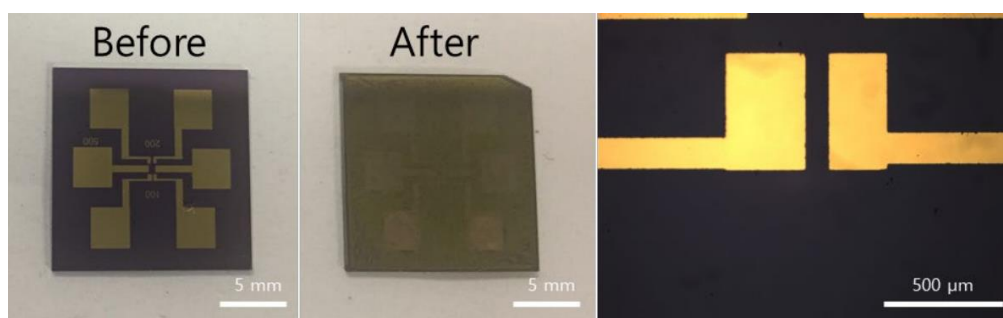


Figure 7. Optical images showing device geometry. Active area defined between electrodes is  $100 \times 500 \mu\text{m}^2$ .

### 2.3 Structural properties of PbS QDs

We synthesized PbS QDs with the ratio of PbO to oleic acid (PbO:OA) of 1:2, 1:5, 1:8, 1:13, and 1:24, resulting in QD sizes of  $d = 2.65, 3.16, 3.62, 3.90,$  and  $4.96$  nm, respectively. The TEM images and their PbO:OA ratios are shown in Figure 8 (a). Histograms with the size distributions of QDs are shown in Figure 9 of the supplementary material. Figure 8 (b) shows the relation between the PbO:OA ratio and the resulting size of the QDs. In addition to the PbO:OA ratio, previous reports show that the injection temperature can also be used to control the size and dispersity of PbS QDs.<sup>[40, 42]</sup> X-ray diffraction (XRD) spectra shown in Figure 8 (c) show the crystallographic phase of the QDs. The peaks are well matched with a cubic PbS structure in accordance with previous reports.<sup>[43]</sup> The broad peaks of the (111), (200), and (220) planes suggest that the size of PbS quantum dots is in the nanometer scale. The full-width-at-half maximum (FWHM) of the diffraction peaks increases as the size of the PbS QDs decreases as shown in Figure 8 (d). For nanocrystal particles, the Scherrer equation below allows us to estimate the particle size from the FWHM,<sup>[44]</sup>

$$d = \frac{K\lambda}{\beta \cos\theta}$$

where  $d$  is the particle size,  $\lambda$  is the wavelength of the radiation,  $\theta$  is the Bragg angle,  $\beta$  is the FWHM on a  $2\theta$  scale, and  $K$  is a dimensionless shape factor. By correlating the QD size extracted from TEM with  $d$  from the Scherrer equation, we can extract a shape factor of  $K = 1.05$  to predict the size of the QDs from the FWHM of XRD data as shown in Figure 8 (e).

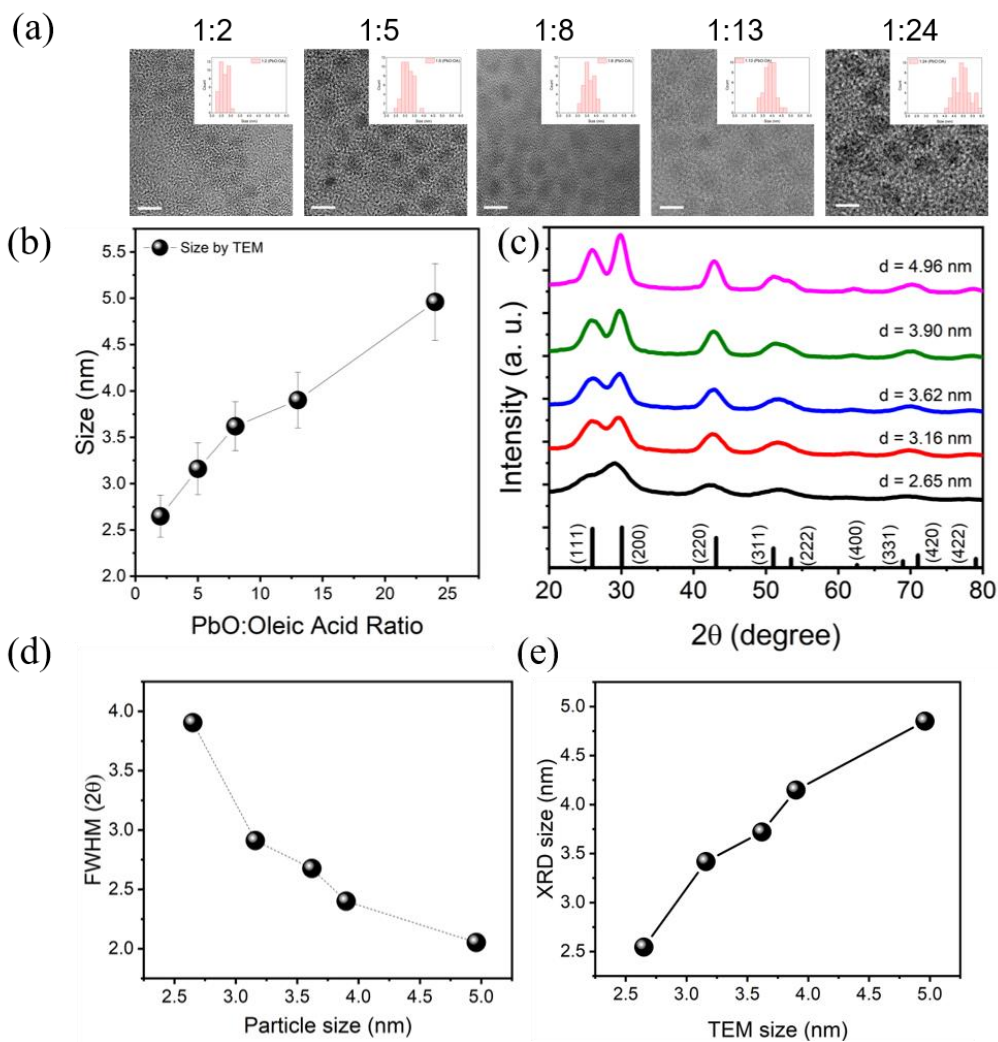


Figure 8. Structural information of PbS QDs. (a) TEM images of PbS QDs with different PbO:OA ratios (1:2, 1:5, 1:8, 1:13, and 1:24) (scale bar is 5 nm). The corresponding size distribution histograms are shown in Figure 9 of the supplementary material. (b) Average size vs PbO:OA ratio. (c) XRD patterns for different sizes (2.65, 3.16, 3.62, 3.90, and 4.96 nm) of PbS QDs. (d) FWHM of the (220) plane of different sizes of PbS QDs. FWHM increases as the QD size decreases. (e) Size estimation from XRD and the Scherrer equation closely matches the size of QDs from TEM images by fitting to  $K = 1.05$ .

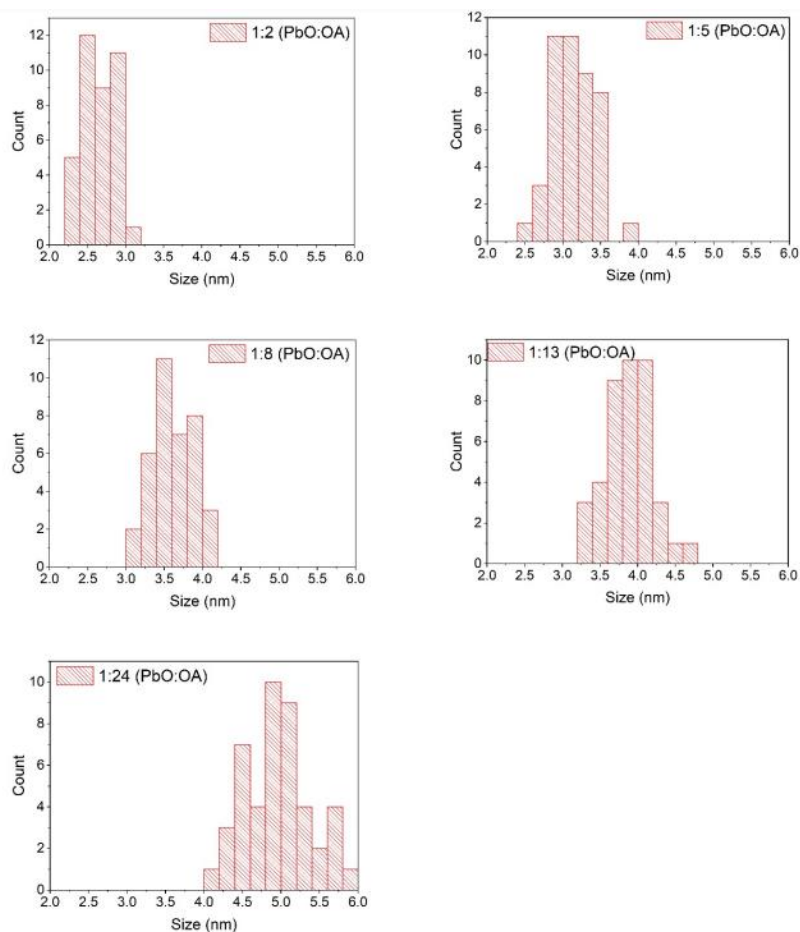


Figure 9. TEM size histograms for various PbO:OA ratio.

#### 2.4 Optical properties of PbS QDs

Figure 10 (a) shows a series of absorption spectra for the PbS QDs of different sizes, showing a clear shift in absorption and its first exciton peak from  $\lambda = 805$  nm for  $d = 2.65$  nm to  $\lambda = 1350$  nm for  $d = 4.96$  nm. As expected from quantum confinement, the first exciton goes to a shorter wavelength (higher energy) as the size of the QD decreases. UV/vis transmission through

QD films with varying thicknesses was performed to extract their absorption coefficients shown in Figure 10 (b). The full set of absorption curves as a function of thickness and wavelength is shown in Figure 11, clearly showing the decrease in absorption as the thickness decreases and as the wavelength increases. The absorption coefficient was calculated by the Beer-Lambert law equation,<sup>[45]</sup>

$$I(\lambda) = I_0 e^{-\alpha(\lambda)t}$$

where  $I(\lambda)$  is the wavelength-dependent transmittance,  $I_0$  is the reference transmittance without the absorption film,  $\alpha(\lambda)$  is the wavelength-dependent absorption coefficient, and  $t$  is the thickness of the absorption film. The absorption coefficients obtained and shown in Figure 10 (b) reach more than  $10^5 \text{ cm}^{-1}$  in the visible range, in good agreement with previous reports. The absorption coefficients also show a peak due to the first exciton level. From ellipsometry measurements, we extracted the refractive index and the extinction coefficient ( $n, k$ ) of PbS QDs in the visible range. The ( $n, k$ ) values for  $d = 3.62 \text{ nm}$  QDs are shown in Figure 10 (c), and the full set of ( $n, k$ ) for the rest of QD sizes is shown in Figure 12. The extinction coefficient ( $k$ ) from ellipsometry provides a second way to extract the absorption coefficient from the following expression:<sup>[46]</sup>

$$\alpha = \frac{4\pi k}{\lambda}$$

The absorption coefficient values from ellipsometry and UV-vis absorption are shown in Figure 10 (d) for  $d = 2.65 \text{ nm}$ , showing similar behavior in the vis range. The absorption coefficients from UV/vis absorption and from  $k$  (ellipsometry) for the rest of the QDs are shown in Figure 13,



which also show similar behavior in the vis range. The penetration depths extracted from UV-vis absorption coefficients are shown in Figure 10 (e). In the visible range (400–700 nm), the absorption levels are very similar for different QD sizes, showing that the most visible light has a penetration depth of 700 nm), the penetration depths increase drastically. IR photons have much larger penetration depths in smaller QDs since photons with large wavelengths do not have enough energy to be absorbed by smaller QDs with higher bandgaps. The penetration depths show a minimum at the first exciton level, which dominates the light absorption in the IR. The bandgap of PbS quantum dots is calculated from the following equation:<sup>[47]</sup>

$$(\alpha h\nu)^{1/r} \sim (h\nu - E_g)$$

where  $\alpha$  is the absorption coefficient,  $h$  is Planck's constant,  $\nu$  is the photon's frequency, and  $E_g$  is the bandgap. The value of the exponent denotes the nature of the electronic transition. PbS is the direct allowed transition, so  $r = 1/2$  is used for the calculation. The bandgaps of PbS quantum dots shown are  $E_g = 1.39, 1.14, 1.07, 0.96,$  and  $0.86$  eV for PbS QDs with respective  $d = 2.65, 3.16, 3.62,$   $3.9,$  and  $4.96$  nm, as shown in Figure 10 (f).

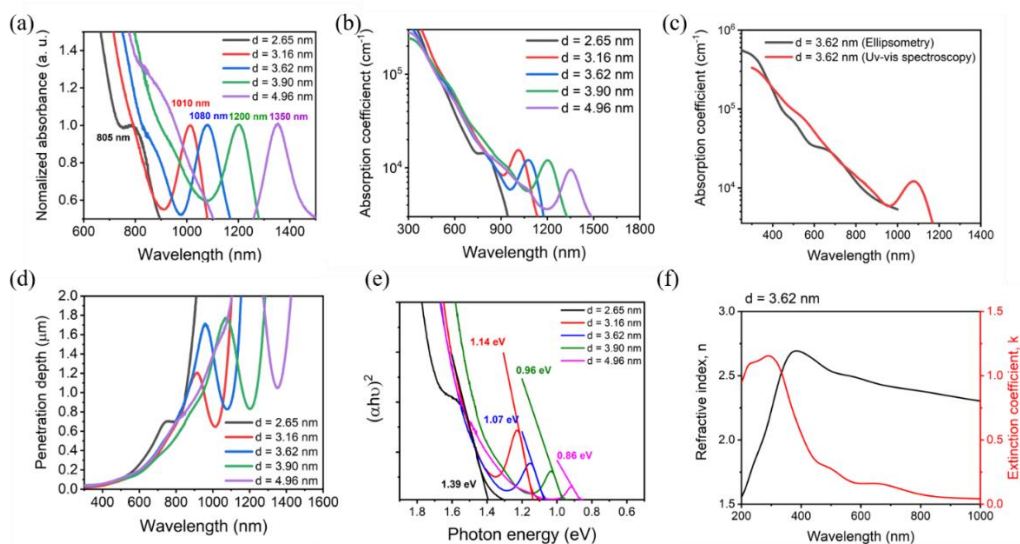


Figure 10. Optical properties of PbS QDs of different sizes. (a) Absorbance of PbS QDs of different sizes. The first absorption peaks are located at  $\lambda = 805, 1010, 1080, 1200,$  and  $1350$  nm depending on the size of PbS QDs ( $d = 2.65, 3.16, 3.62, 3.90,$  and  $4.96$  nm, respectively). (b) The absorption coefficient of different sizes of PbS QDs. (c) Complex refractive index ( $n, k$ ) ( $k$ : extinction coefficient) extracted from ellipsometry for  $d = 3.62$  nm. The rest of ( $n, k$ ) for different QD sizes is shown in Figure 12. (d) Absorption coefficient from ellipsometry and UV-vis absorption show similar behavior for  $d = 2.65$  nm in the visible range. (e) Penetration depth vs wavelength of different PbS QDs. In the vis range, the penetration depth is  $<400$  nm for QDs of different sizes. In the IR range, the penetration depth is dominated by the exciton peak. (f)  $(\alpha\hbar\nu)1/r$  for PbS QDs allows extracting bandgaps of  $E_g = 1.39, 1.14, 1.07, 0.96,$  and  $0.86$  eV for  $d = 2.65, 3.16, 3.62, 3.90,$  and  $4.96$  nm, respectively.

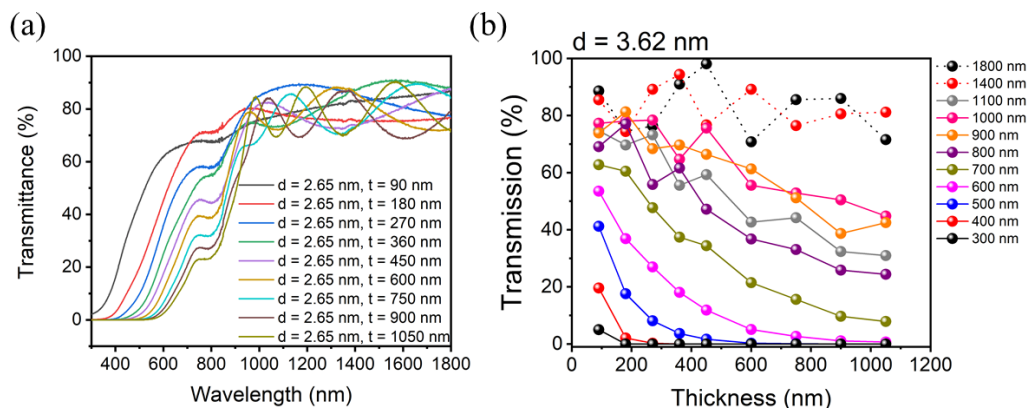


Figure 11. Transmission data. (a) Transmission versus wavelength with different thickness. The transmission becomes decreased as thicker. Below first extinction peak, there is sinuous waves due to the interference. (b) Transmission versus thickness. The transmission decreases exponentially for wavelength below the band gap. For long wavelengths, transmission remains high as photons cannot be absorbed.

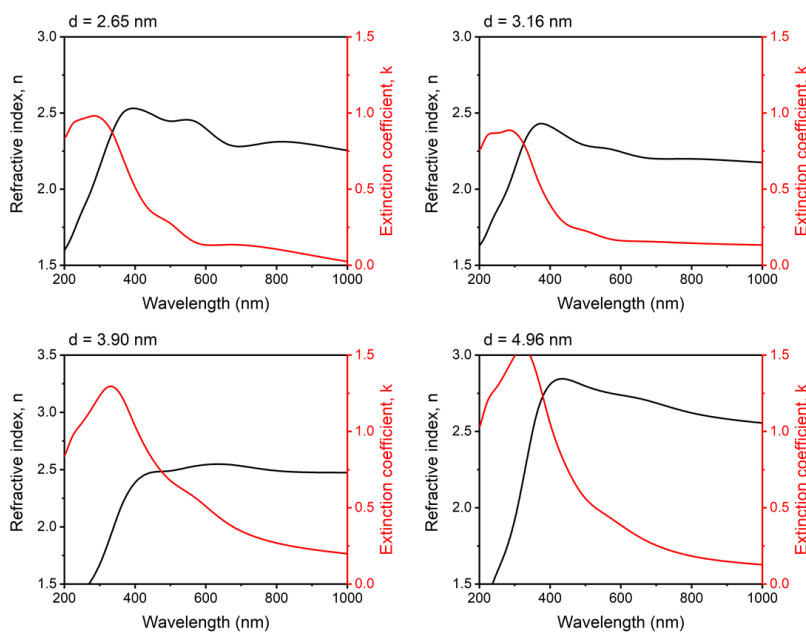


Figure 12. Refractive index (n,k) of QD films with QD sizes of  $d=2.65, 3.16, 3.90$  and  $4.96$  nm as function of wavelength obtained by ellipsometry.

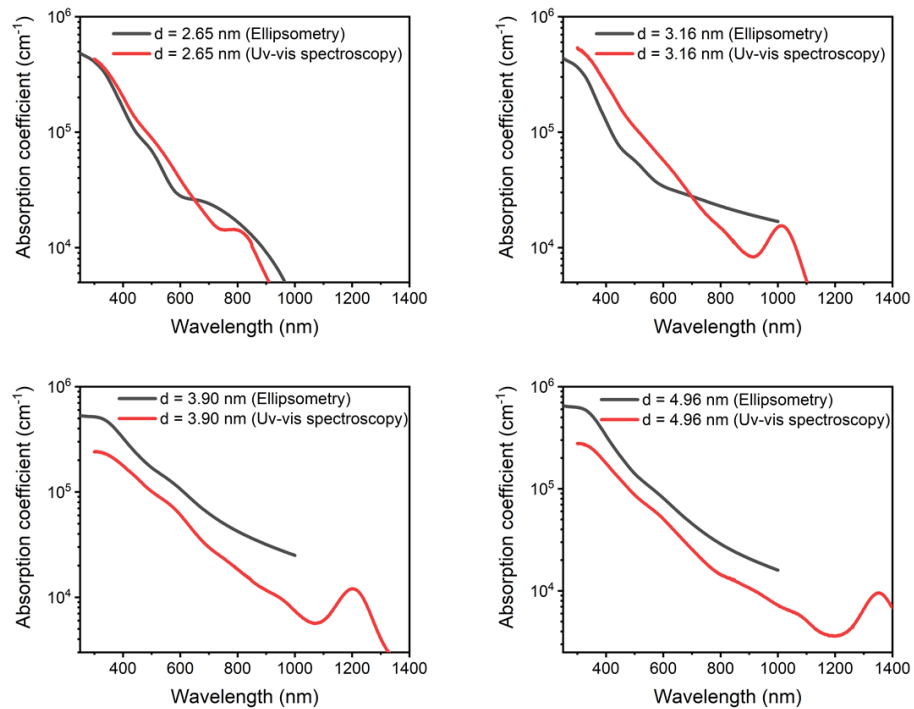


Figure 13. Absorption coefficients. Comparison of absorption coefficients obtained by UV/Vis spectroscopy and by Ellipsometry showing show similar behaviors.

### 2.5 Photoresponse of hybrid graphene – PbS photodetectors

Hybrid photodetectors were fabricated by spin coating PbS QDs on single layer Gr to investigate the hybrid Gr/QD photoresponse performance. PbS QDs of different sizes were coated on a graphene monolayer to reach a thickness of 150 nm. The photocurrent normalized for different sizes of QDs as a function of light wavelength is shown in Figure 14 (a) using a Xe lamp with a monochromator. The photocurrent is normalized to the highest photoresponse for each QD. The photocurrent shifts toward the IR and has a peak closely matching the absorption exciton peak. This behavior resembles the absorption spectrum behavior, proving the role of QDs absorbing light and

generating photocarriers. After the photoresponse exciton peak, the photocurrent drops since longer wavelengths are not able to excite photocarriers. Figure 14 (b) shows the photoresponsivity of 150 nm thick films with different sizes as a function of QD size under a  $\lambda = 635$  nm laser excitation. The photoresponse clearly decreases as the size of the QDs increases. This can be related to a higher filling factor, i.e., more packed QDs, with smaller QDs. This higher filling factor will result in more QDs absorbing light with the same thickness. In addition, better packed QDs can result in easier transport of photoexcited holes through the QDs in their path to the bottom graphene. A lower response for larger QDs has also been observed in previous reports.<sup>[13]</sup> The time response of Gr/QD photodetectors was also investigated, as shown in Figure 14 (c). The devices with different QD sizes show similar time responses in the time scale of the experiments, in all cases showing subsecond modulation, with rising times of  $\sim 10$  to 50 ms and slower recovery times of 50–100 ms. Time fittings are shown in Figure 15. The recovery process also has a slower component  $>1$  s, which has also been reported in previous hybrid Gr/QD reports associated with traps in the QDs.<sup>[13, 34]</sup> However, Figure 14 (c) shows that subsecond modulation is possible with different quantum sizes and, therefore, with a broad spectral range. The time responses in Figure 14 (c) also confirm the higher photoresponse for smaller QDs. We also measured the effect of light intensity on photoresponse, showing a decrease in photoresponsivity as the light intensity decreases as shown in Figure 14 (d). The plot also confirms higher responsivity for smaller QDs. The decrease in responsivity with the light intensity is due to saturation in traps in QDs, higher recombination rate, and lower transfer of photocarriers from QDs to Gr.<sup>[15, 34]</sup> Small QDs  $d = 2.65$  nm can reach a photoresponsivity  $>10^7$  A/W. Overall, photoresponsivity is affected by QD size, bias voltage, power, and wavelength, with clear

trends showing higher photoresponsivity for smaller QDs and under low incident power.

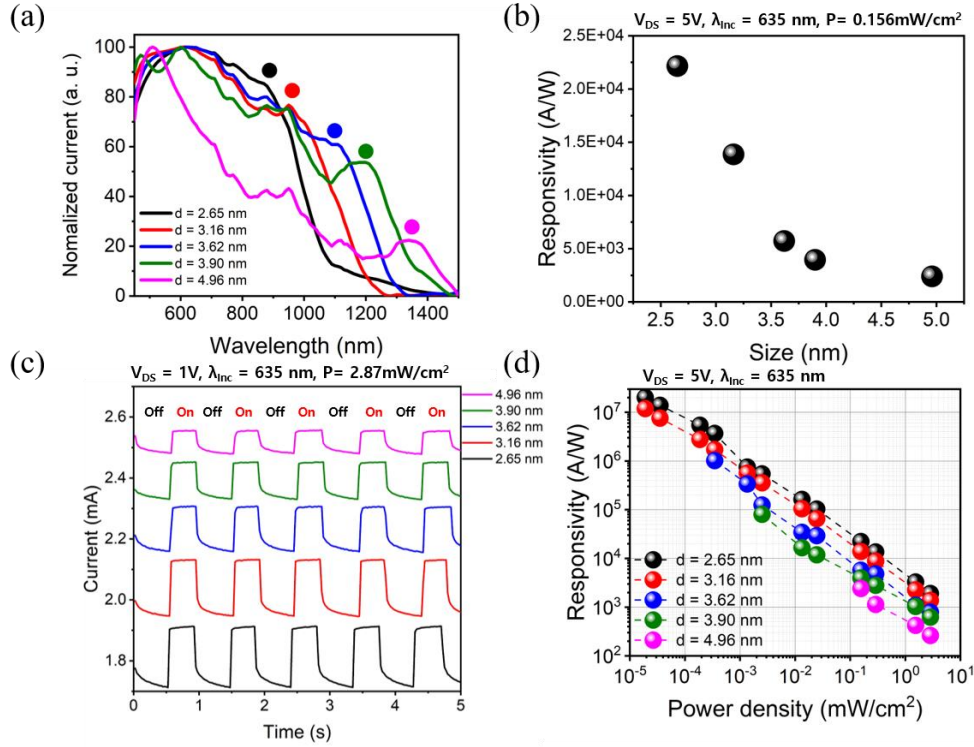


Figure 14. Photoresponse of hybrid Gr/QD photodetectors. (a) Normalized current vs wavelength (Xe lamp with monochromator) for different sizes of PbS QDs but with the same film thickness of  $t = 150$  nm. (b) Responsivity as a function of QD size under  $\lambda = 635$  nm for different QD sizes ( $t = 150$  nm), showing a decrease in responsivity as the QD size decreases. (c) Time response showing subsecond modulation capability for QDs of different sizes and confirming a larger photoresponse of smaller QD size. Rising times are  $\sim 10$  to  $50$  ms, and recovery times are  $\sim 50$  to  $100$  ms. The recovery process also has a slower component  $> 1$  s. (d) Responsivity decreases as the light intensity increases for different sizes of QDs. Smaller QDs also show the highest responsivity for different light intensities. Smallest PbS QDs ( $d = 2.65$  nm) have highest responsivity reaching  $> 10^7$  A/W. The I/V curves for different light intensities and QD sizes are shown in Figure 16.

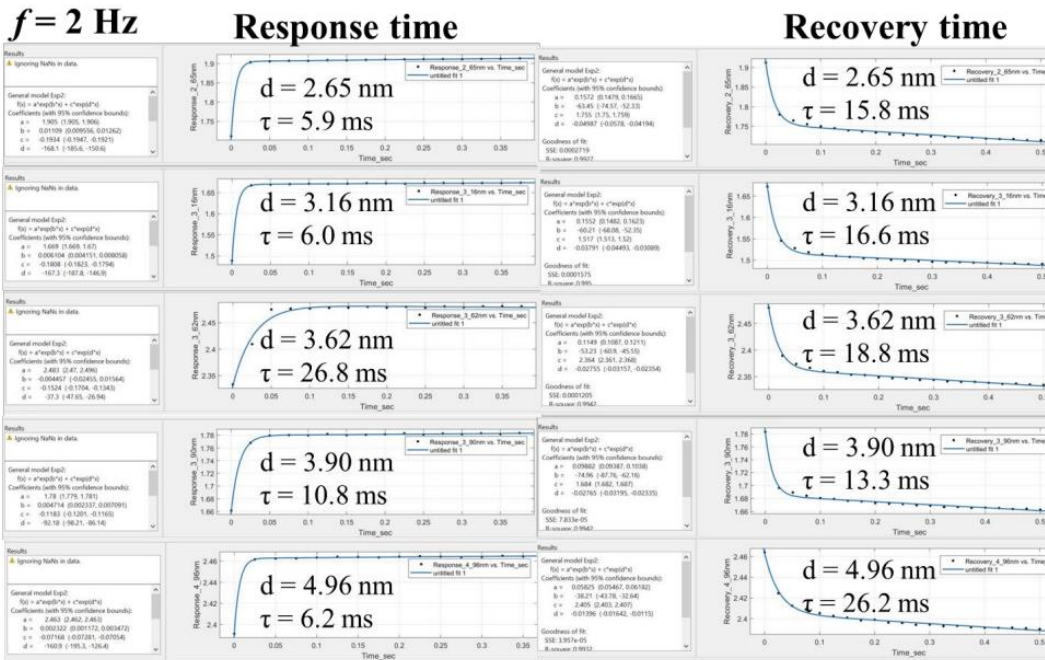


Figure 15 Time response fittings. Exponential fitting for response and recovery time for various QD size.

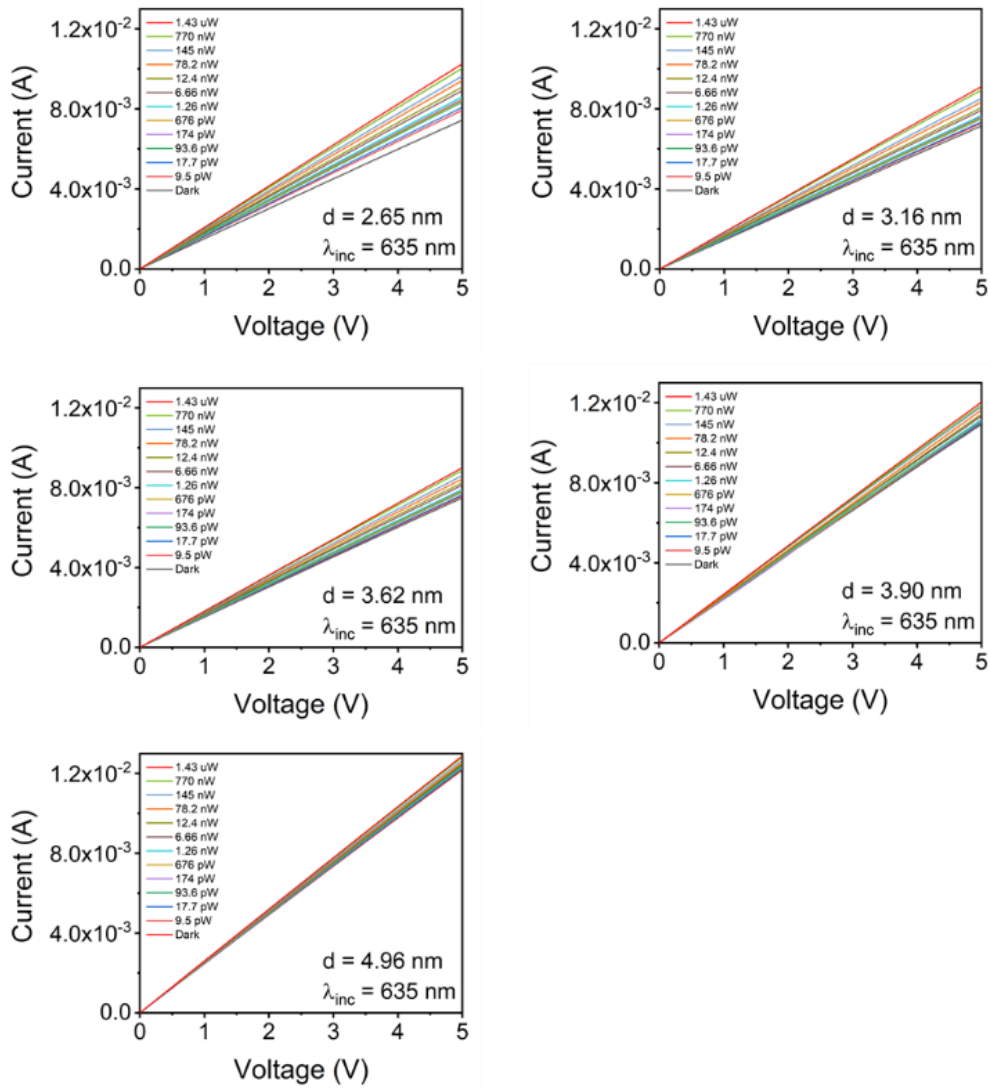


Figure 16 I/V curves. I/V curves under  $\lambda=635$  illumination for various powers and QD size.

An important design parameter for QD photodetectors is the thickness. For correct operation, there is a lower limit to the film thickness set by the penetration depth, which is wavelength dependent. Films thinner than the penetration depth would rapidly collect less than 63%



of light at the wavelength of interest, drastically reducing its photoresponse. Thickness also has an upper limit set by the diffusion length, which sets the maximum length that photocarriers can travel before they recombine. Due to the poor mobility of QD films, the diffusion length is typically below 200 nm.<sup>[18]</sup> This compromise in thickness is illustrated in Figure 17(a). We study the photoresponse of hybrid Gr/QD devices as a function of thickness using the smallest PbS QDs ( $d = 2.65$  nm). Figure 17 (b) shows the photocurrent vs wavelength with various thicknesses of 2.65 nm PbS QDs. Thin layers show higher responsivity in the vis range ( $\sim 400$  to  $600$  nm). As the thickness increases, their photoresponse improves toward the infrared. Figure 17 (c) shows that for visible light ( $\lambda = 500$  nm), the maximum photoresponse is at  $t = 360$  nm, but for thicker films, the responsivity rapidly decreases. For near IR light ( $\lambda = 800$  nm), the maximum photoresponsivity is at  $t = 1250$  nm, followed by a decrease as  $t$  increases. Thin films absorb visible light efficiently due to its short penetration depth while also collecting photocarriers efficiently since they are thinner than their diffusion length. However, thin films collect IR light poorly, resulting in a low photoresponse. For thick films, such as  $t = 1200$  nm, visible light is effectively absorbed in the top 500 nm layers, but the charges recombine before reaching the bottom graphene charge collector. For IR light, as the wavelength increases, it gets absorbed deeper into the QD film and closer to the graphene collector, increasing the photoresponse as the wavelength increases until reaching the bandgap edge. Figure 17 (d) shows the wavelength detection window vs thickness. The long wavelength limit (low energy) is determined by the size (bandgap) of the PbS QDs, and the bottom limit (high energy) of the window is set by the thickness of PbS QDs. The window was set as the full-width at half maximum of the spectral response from Figure 17 (b). Above  $t = 700$  nm, high energy photons absorbed at the top

cannot reach the graphene layer and only longer wavelengths penetrate deep enough to produce photocarriers near the graphene layer. As  $t$  increases, the response window narrows down toward the infrared. In cases in which the graphene collector would be on top, these trends would reverse. Recently, it was shown that intercalated layers inside the QD film can overcome the limitations of the short diffusion length on the thickness of hybrid Gr/QD photodetectors.<sup>[18]</sup> Figure 17 (e) shows the time response for different thicknesses under  $\lambda = 635$  nm. The photoresponse is higher for thin films and decreases as the films get thicker. In all cases, we observe fast modulation below the subsecond scale. These results show that in addition to the QD size, the thickness can also be used to tune the spectral response of hybrid Gr/QD photodetectors keeping subsecond time modulation capabilities.

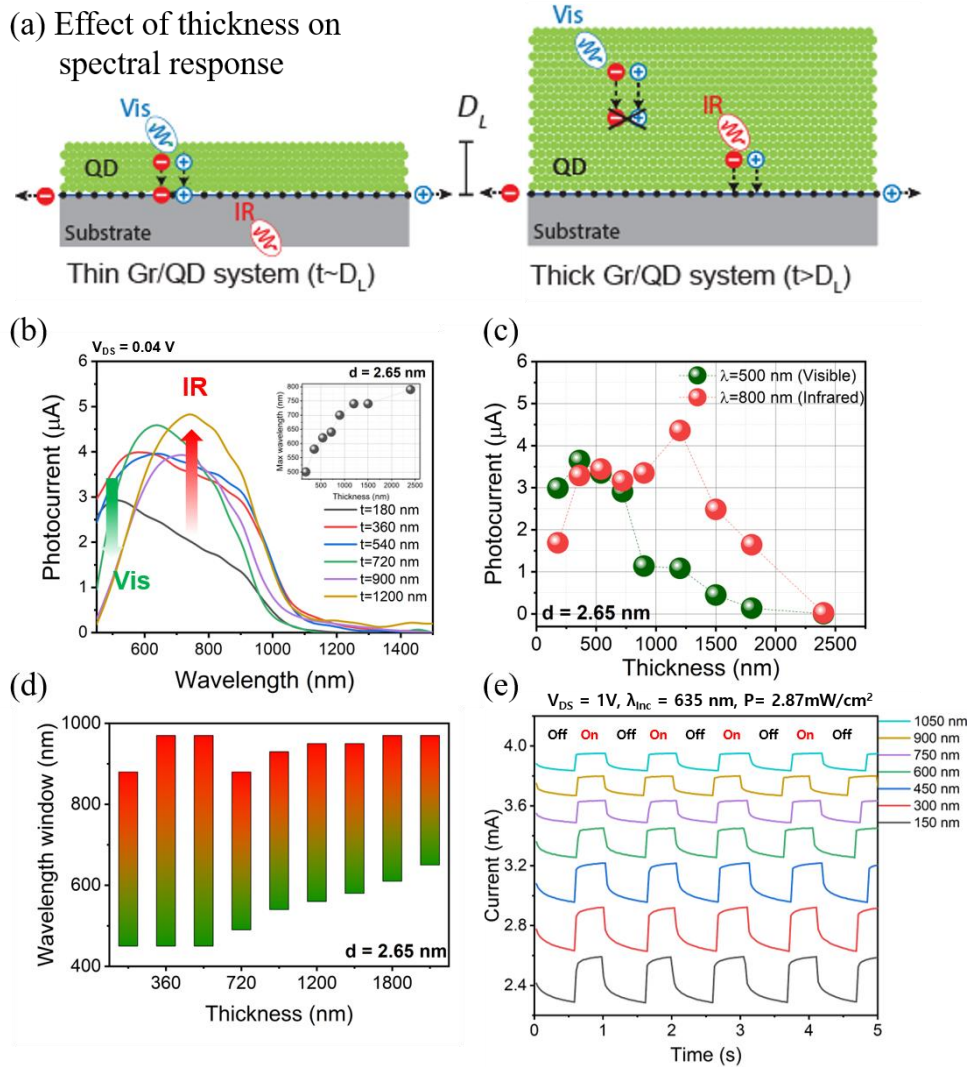


Figure 17 Effect of thickness. (a) Diagram showing light absorption and charge collection in thin and thick QD layers with respect to the diffusion length  $D_L$ . (b) Normalized photocurrent vs wavelength with different thicknesses of PbS QDs showing a shift in response toward larger  $\lambda$  as  $t$  increases. (c) Photocurrent vs thickness for  $\lambda = 500$  and  $800\text{ nm}$ . (d) Window response shifts toward longer wavelengths as the thickness of the QD film increases. The windows correspond to the FWHM of the photocurrent vs wavelength in (b). (e) Time modulation of photocurrent for different thicknesses of PbS QDs on graphene.

In summary, we report on the optical properties of PbS QDs and the effect of QD size and film thickness on the photoresponse of novel hybrid PbS QD on graphene photodetectors. The size of PbS QDs is controlled by the ratio of PbO and oleic acid. The size allows controlling the absorption spectrum, shifting the absorption peak due to the first exciton peak to longer wavelengths as the QD size increases. The absorption coefficient of PbS QDs reaches values of  $10^5$  to  $10^4$   $\text{cm}^{-1}$  in the visible region with little variations with the QD size. In IR, the absorption coefficients are size dependent as the first exciton peak shifts. The photoresponse of hybrid Gr/QD photodetectors has a high responsivity ( $>10^7$  A/W), with a response time of  $\sim 50$  ms and a recovery time of  $\sim 100$  ms for varying QD sizes and film thicknesses. As expected, as the QD size increases, the spectral photoresponsivity is shifted toward the IR. For a fixed thickness, the responsivity decreases as the QD size increases, which can be due to a lower packing factor as the QD size increases; however, further analysis is required. The thickness also allows us to tune the spectral response of the QDs, with thin ( $t < 400$  nm) films having stronger photoresponse in the visible and thicker films enhancing the response toward the IR. The results herein provide valuable information to design the QD size and film thickness for a high response and tunable spectrum hybrid QD/Gr photodetector.

Chapter 2, in full, is a reprint of the material as it appears in “Optoelectronic response of hybrid PbS-QD/graphene photodetectors”. Seungbae Ahn, Hyeseung Chung, Wenjun Chen, Miguel A Moreno-Gonzalez, Oscar Vazquez-Mena, *The Journal of Chemical Physics*, 151, 23, 234705 (2019). The dissertation author was the primary investigator and author of this paper.

### **Measuring the carrier diffusion length in quantum dot films using graphene as photocarrier density probe**

The diffusion length of quantum dot (QD) films is a critical parameter to improve the performance of QD-based optoelectronic devices. The dot-to-dot hopping transport mechanism results in shorter diffusion lengths compared to bulk solids. Herein, we present an experimental method to measure the diffusion length in PbS QD films using single layer graphene as a charge collector to monitor the density of photogenerated carriers. By producing devices with different thickness, we can construct light absorption and photocarrier density profiles, allowing to extract light penetration depths and carrier diffusion lengths for electrons and holes. We realized devices with small (size:  $\sim 2.5$  nm) and large (size:  $\sim 4.8$  nm) QDs and use  $\lambda=532$  and  $\lambda=635$  nm illuminations. For small QDs, we obtain diffusion lengths of 180 nm for holes and 500 nm for electrons. For large QDs, we obtain diffusion lengths of 120 nm for holes and 150 nm for electrons. Our results show that films made of small QD films have longer diffusion lengths for holes and for electrons. We also observe that wavelength illumination may have a small effect, with electrons showing a diffusion length of 500 nm and 420 nm under  $\lambda=532$  nm and  $\lambda=635$  nm illumination, respectively, which may due to increased interactions between photocarriers for longer wavelengths with deeper penetration depths. Our results demonstrate an effective technique to calculate diffusion lengths, and indicate that QD size and wavelength illumination can play important roles in the diffusion and electrical transport of QD films.

### 3.1 Introduction

Colloidal quantum dots (QDs) have important advantages for optoelectronics such as strong light absorption coefficient, a size tunable direct band gap, and low-cost wet chemical synthesis, making them very attractive for different optoelectronic applications such as solar cells light-emitting diodes, and photodetectors.<sup>[6, 20-24, 26, 27, 30, 31, 36, 37, 48, 49-51]</sup> However, due to their inherent nanoparticle structure, colloidal QD films have poor conductivity because their electronic transport relies on dot-to-dot hopping mechanisms and on surface ligands to facilitate electron coupling between QDs, resulting in low charge mobilities ( $\mu < 1 \text{ cm}^2/\text{Vs}$ ) and short diffusion lengths ( $L_D \sim 100 \text{ nm}$ ) compared with conventional bulk crystalline semiconductors.<sup>[28, 33, 38, 39, 52-55]</sup> Photoconductive detectors that combine PbS QDs, as light absorbers and photocarrier generators, with single layer graphene (SLG), as a charge collector and photocurrent channel, have shown very high responsivity ( $10^7 \text{ AW}^{-1}$ ) with very thin active films with thicknesses ( $t$ ) in the order of  $\sim 100 \text{ nm}$ .<sup>[10, 13, 18, 34, 35, 56-60]</sup> The high mobility of graphene compensates for the poor conductivity of QDs, which combined with the long lifetime traps in QDs results in high photogain and high photoresponsivity.<sup>[13]</sup> Herein, we demonstrate that the photocurrent in graphene can be used to measure the diffusion length of photogenerated holes and electrons in QD films. Diffusion length is a critical parameter for the performance of photovoltaic and photodetector devices.<sup>[33, 39, 55, 61]</sup> Therefore, reliable measurements of diffusion lengths are important to understand the electronic transport in QDs and to improve the design of photodetectors and photovoltaic devices based on QDs.

### 3.2 Results and Discussion

Our concept is similar to a previous report in which light incident on the front surface of

colloidal QD films generate photocarriers that diffuse through the film to reach a QD acceptor layer on the back surface, where charges recombine radiatively to generate a photoluminescent signal.<sup>[38]</sup> In our approach, we have a colloidal QD film, but with a SLG on the back surface instead of the QD acceptor layer. The incident light penetrates into the QD film following the Beer-Lambert law ( $\sim \exp(-x/D_\lambda)$ ), characterized by the light penetration depth ( $D_\lambda$ ), producing photocarriers upon absorption. Then, the photocarriers diffuse in the QD film with a characteristic diffusion length ( $L_D$ ). The photocarriers that reach and transfer to SLG produce a photocurrent as shown in Figure 18 (a). As it has been reported previously, in the case of a PbS QD film directly in contact with SLG, the SLG photocurrent is due to the transfer of photogenerated holes to SLG. Therefore, by probing the SLG photocurrent due to photogenerated holes in QD films with different thickness ( $t$ ), we can estimate the diffusion length of holes ( $L_{D,h}$ ) in the QDs.<sup>[13]</sup> This concept also allows probing the diffusion length of electrons  $L_{D,e}$  in QDs. As previously reported as well, by adding an intermediate ZnO layer between the PbS QD film and SLG, electrons get transferred to SLG instead of holes, allowing to measure the electron  $L_{D,e}$  as shown in Figure 18 (b). By measuring the light absorption and the photocurrent for devices with different thickness, it is possible to extract the light penetration depth and the diffusion length. Since the photocurrent in graphene is proportional to the transfer of photocarriers from the QDs to SLG, then the SLG photocurrent  $I_{ph-SLG}$  is also proportional to the photocarrier distribution  $n_{e,h}^{ph}(x)$  at the SLG-QD interface ( $x=t$ ).

$$I_{ph-SLG} \sim n_{e,h}^{ph}(x = t) \text{ (Eq. 1)}$$

A typical photocarrier distribution with light incident on the front surface is shown in Figure 18 (c). This profile depends on the wavelength-dependent penetration depth ( $D_\lambda$ ) and on the diffusion length

( $L_D$ ). For these experiments, we have produced QD films with thicknesses reaching  $\sim 1 \mu\text{m}$ , which are significantly larger than the depletion layer between SLG and PbS QDs. In addition, we do not apply any voltage bias between the QD film and SLG, avoiding drift currents like in FET mobility measurements.<sup>[53, 54, 62, 63]</sup> Therefore, our estimated values correspond to bulk diffusion lengths in PbS QD films in the absence of electric fields to tune Fermi level or driving charge motion. In order to explore the effect of the QD size, we studied  $L_{D,e}$  and  $L_{D,h}$  for QDs of two different sizes:  $\sim 2.5 \text{ nm}$  and  $\sim 4.8 \text{ nm}$  as shown in Figure 19.



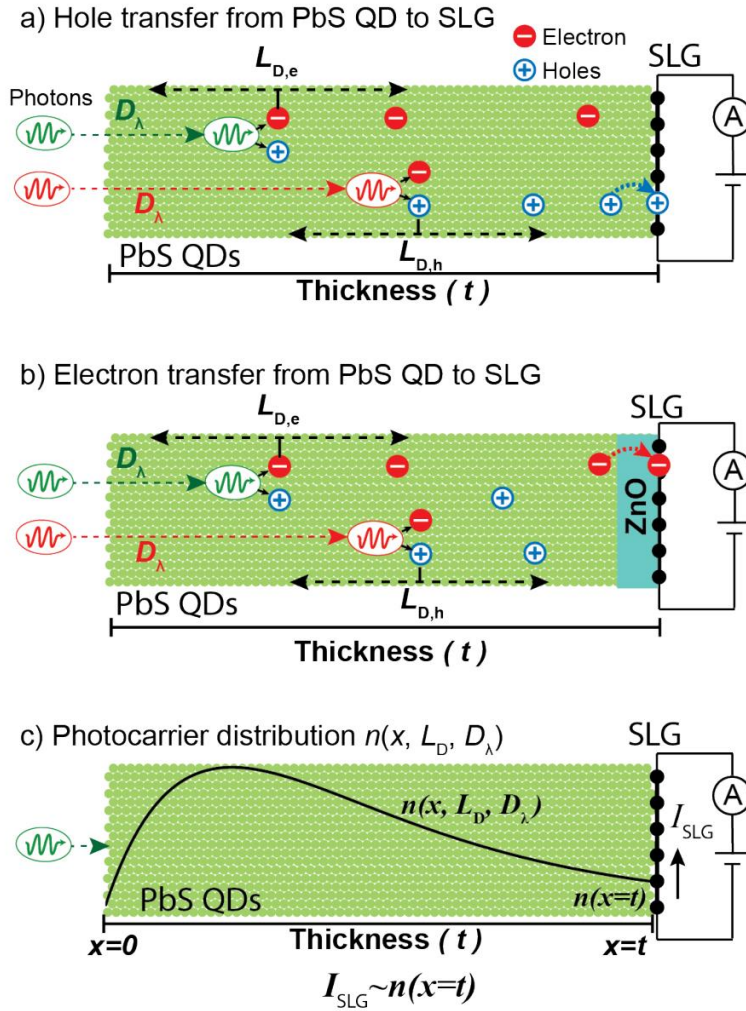


Figure 18 Light penetration and carrier diffusion. a) Incident photons onto a QD film with a wavelength dependent penetration depth ( $D_\lambda$ ) are absorbed generating photocarriers that then diffuse through the film ( $L_D$ ). The photocarriers that reach graphene (SLG) produce a photocurrent. By measuring the light transmission and photocurrent as function of thickness, it is possible to estimate penetration depths and diffusion lengths. For direct QD/SLG junction, holes are transferred to SLG, allowing to estimate the hole diffusion length ( $L_{D,h}$ ). b) In the case of devices with an intermediate ZnO layer, electrons are transferred from the QDs to SLG, allowing to estimate the diffusion length of electrons ( $L_{D,e}$ ). c) Typical behavior of photocurrent concentration under illumination assuming Beer-Lambert model for light penetration and diffusive behavior of photocarriers based on generation and recombination events.

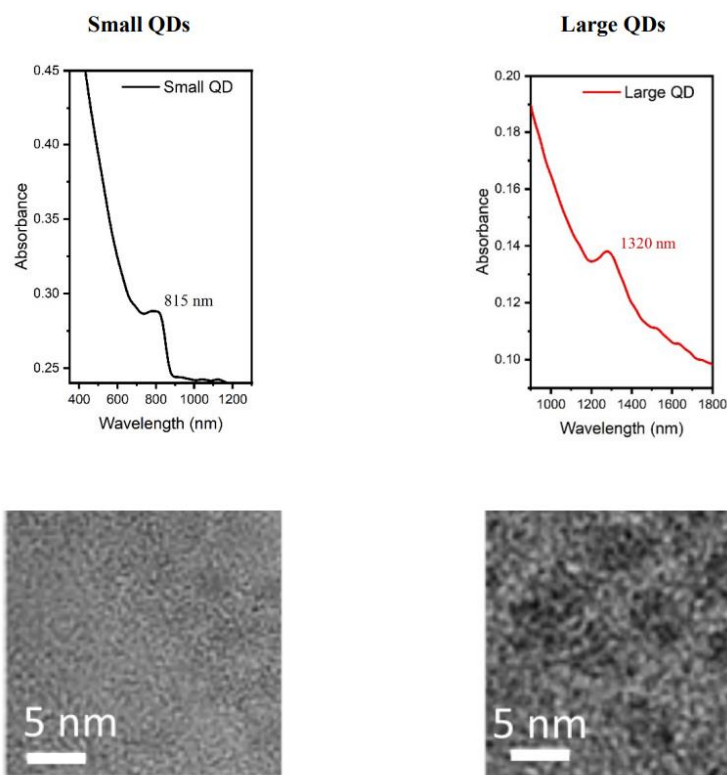


Figure 19 Absorption spectrum and TEM of PbS QDs.

The geometry for the device to measure the hole diffusion length is shown in Figure 20 (a). It is based on a SLG on a glass substrate layer covering a large area of the chip with two predefined Au contacts to apply a bias voltage ( $V_B$ ) and measure the current through graphene. On top of the graphene there is QD layer that absorbs light and generate photocarriers that are collected by SLG, generating a photocurrent. The device also contains a light penetration testing area without electrical contacts that serve to test the transmission of light and extract the light penetration depth for different light wavelengths. By fabricating a series of devices with different thicknesses, we were able to extract light absorption and photocurrent curves as a function of thickness. We also prepared devices

to measure the electron diffusion by adding a ZnO layer in between the QDs and SLG as shown in Figure 20 (b). Optical images of the fabricated devices for measuring the hole (QD/SLG) and electron (QD/ZnO/SLG) diffusion lengths are shown in Figure 20 (c and d), respectively. The active areas have a channel length of 100  $\mu\text{m}$  and width of 500  $\mu\text{m}$ , defined by the contact geometry. We tested two different PbS QD sizes: Small QDs with first exciton absorption peak at 815 nm (1.52 eV) and Large QDs with first exciton peak at 1320 nm (0.94 eV) as shown in Figure 19. Therefore, we fabricated four types of devices: 1) Small PbS QDs on SLG, 2) Small PbS QDs on ZnO/SLG, 3) Large QDs on SLG, and 4) Large PbS QDs on ZnO/SLG. For each type of device, we prepared 5, 10, 15, 20, 30, 40 and 50 layers of QDs. The fabrication process of the photodetectors for QD/SLG and QD/ZnO/SLG are described in the chapter 3.4 Fabrication process. Briefly, a CVD-SLG (Graphenea, Spain) is transferred onto a substrate with prepatterned Au contacts using wet transfer with PMMA as supporting layer. Then, PbS QDs functionalized with oleic acid in toluene solution are spin coated on the substrate followed by ligand exchange with tetrabutylammonium iodide (TBAI). This coating process is repeated for different number of layers. The thickness is estimated from a calibration device based on spin coating of 50 QD layers, as show in SEM cross section images in Figure 21. For our Small QDs, we obtain a  $1027\pm 50$  nm thick film for 50 layers, corresponding to  $20.54\pm 1$  nm per layer. For the Large QDs we obtain a  $653\pm 30$  nm thick film for 50 layers, corresponding to  $13\pm 0.6$  nm per layer. For the ZnO layer devices, we spin coated and anneal a 100 nm thick layer of ZnO nanoparticles after the SLG transfer and then adding the PbS QDs

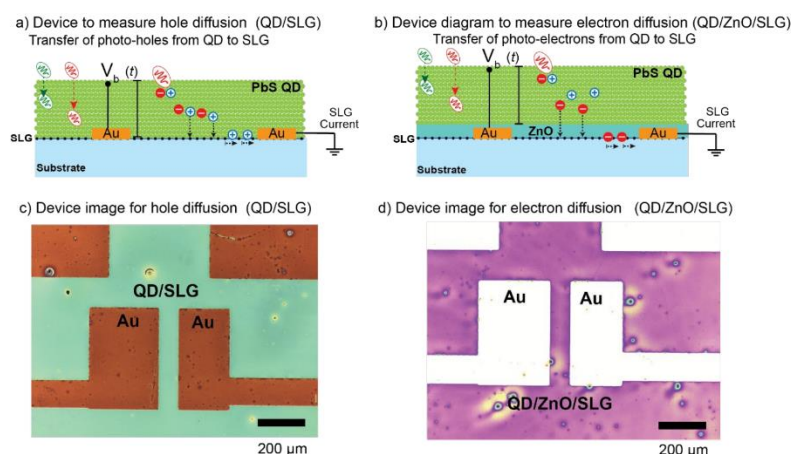


Figure 20 Device structure. a) Device diagram to measure hole diffusion length with a glass substrate, predefined Au contacts, a bottom SLG, and a PbS QD film. b) Device diagram to measure electron diffusion length with a glass substrate, predefined Au contacts, a bottom SLG, a PbS QD film, and an intermediate ZnO layer that transfers photogenerated electrons from the QDs to SLG. c,d) Optical images of the devices shown in a,b), showing the Au electrodes defining the active photodetection areas with channel length of 100  $\mu\text{m}$  and width of 500  $\mu\text{m}$

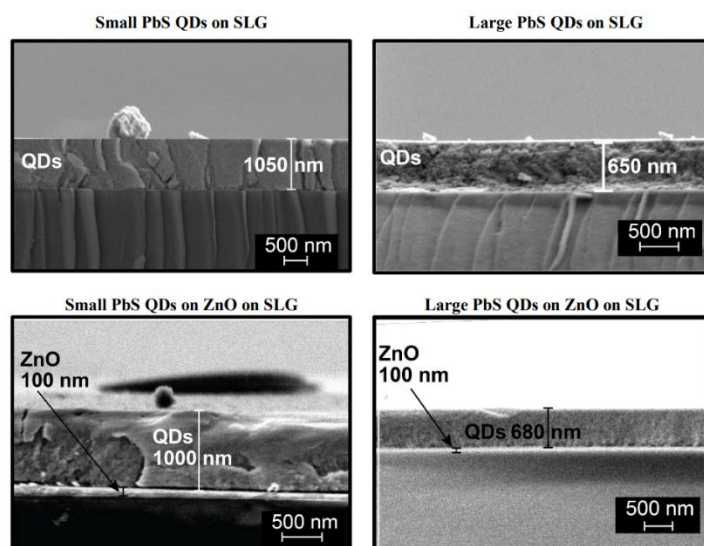


Figure 21 SEM Cross sections

The photoresponse and charge transfer for QD/SLG and QD/ZnO/SLG devices under  $\lambda=635$  nm illumination are shown in Figure 22. As it is observed in Figure 22 (a), in the QD/SLG devices the photocurrent is positive as the current through SLG increases when the light is ON. This is expected as SLG on glass typically has a ‘p’-type behavior. When photogenerated holes are transferred to SLG, this increases the number of majority hole carriers, resulting in an increase in the current. In contrast, in the case of QD/ZnO/SLG, the current decreases when light is ON. The transfer of photogenerated electrons to p-type SLG results in a decrease in the number of holes, and therefore in a reduced current and a negative photocurrent. This is also shown in the transconductance measurements performed on Si/SiO<sub>2</sub> substrates using a 300 nm thick SiO<sub>2</sub> as gate dielectric and doped-Si as back gate (Figure 23). Figure 22 (c) shows the SLG drain current as function of gate voltage ( $I_{DS}$  vs  $V_g$ ) for QD/SLG devices. The  $I_{DS}$  minimum, corresponding to the Fermi level hitting the Dirac point of SLG, is at  $V_g = 8$  V, meaning a p-type conductance as electrons have to be added to reach the Dirac point. Under illumination, the  $I_{DS}$  minimum shifts towards larger  $V_g$ , indicating that SLG becomes even more p-doped and therefore that photogenerated holes are transferred from the QDs to SLG. Figure 22 (d) shows the opposite behavior for QD/ZnO/SLG. In this case, the SLG with ZnO and PbS QDs on top still shows a p-type behavior as the  $I_{DS}$  minimum is also at  $V_g > 0$ . However, under illumination the  $I_{DS}$  minimum shifts towards lower  $V_g$  values, indicating that the Fermi level has increased, and therefore that photogenerated electrons are transferred from the QDs to SLG. These results indicate that in the case of QD/SLG devices, the SLG photocurrent is proportional to the photogenerated holes that reach the QD/SLG junctions, whereas for QD/ZnO/SLG the photocurrent is proportional to the photogenerated electrons reaching

SLG.

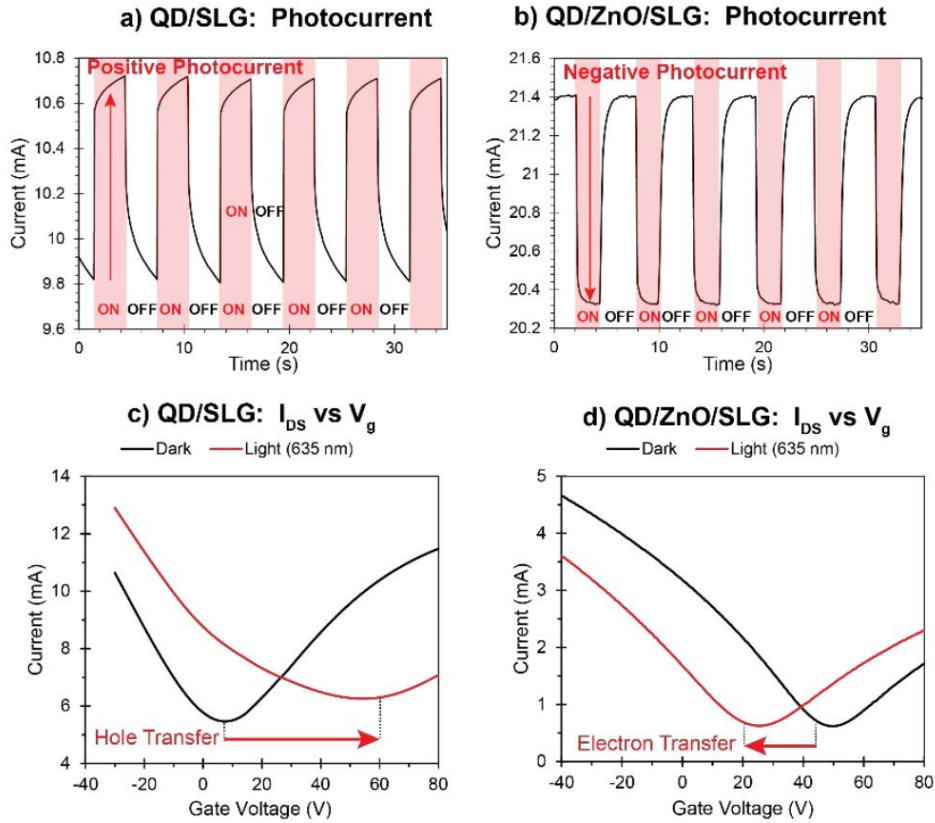


Figure 22 Photoresponse and charge transfer. a,b) Time response of QD/SLG and QD/ZnO/SLG devices, showing their respective increase and decrease in current under  $\lambda=635$  nm illumination, indicating positive and negative photocurrents, respectively. c,d) Transconductance of QD/SLG and QD/ZnO/SLG devices on Si/SiO<sub>2</sub> substrates (Figure 23), showing the opposite shifts in Fermi level under illumination. For QD/SLG, photogenerated holes are transferred to SLG, and for QD/SLG/ZnO photogenerated electrons are transferred to SLG

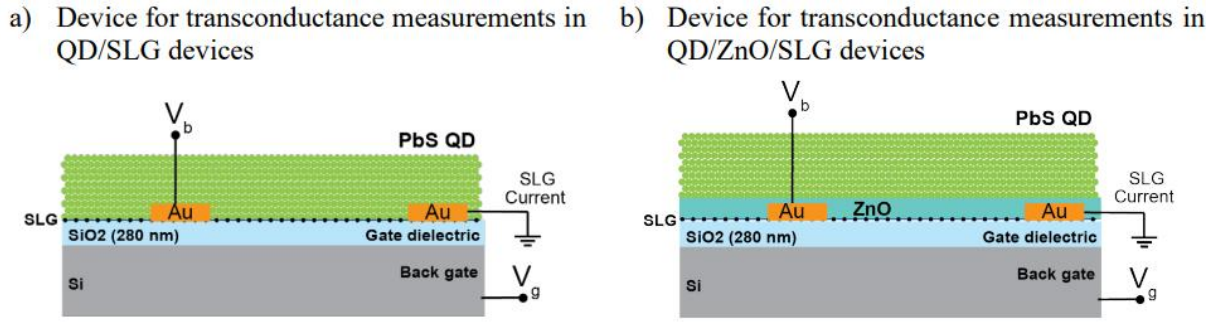


Figure 23 Transconductance devices

In order to extract the diffusion length from the photocurrent measurements as function of thickness, it is important to estimate the light penetration depth (inverse of the absorption coefficient). The penetration depth for PbS QDs has been reported in previous works,<sup>[64]</sup> however, the QD size and morphology has a strong impact in the band gap and thus on absorption coefficients. Therefore, we measured the light absorption for incident wavelengths of  $\lambda=532$  and  $635$  nm for each sample. The results for light transmission as function of thickness are shown in Figure 24 with their exponential fitting to the BeerLambert law ( $\sim \exp[-t/D_\lambda]$ ) for the four types of devices using two different wavelengths:  $\lambda=532$  nm and  $\lambda=635$  nm. As expected, the penetration depths were deeper for the longer  $635$  nm wavelength. In principle, the ZnO layer should not affect the penetration depth, however, the penetration depth for QD/SLG and QD/ZnO/SLG showed slight variations of  $20\text{--}30$  nm for the small QDs and  $20\text{--}25$  nm for the large QDs. We ascribe these variations to thickness errors which reach  $\sim \pm 50$  nm for thicker devices. However, for different QD size we observe notable differences, with shorter penetration depths for the Large QDs. For  $\lambda=532$  nm in QD/SLG devices, the penetration depth was  $D_\lambda=130$  nm for Small QDs and  $D_\lambda=85$  nm for Large QDs. For  $\lambda=635$  nm,



also in QD/SLG devices, the penetration depth was  $D_\lambda=385$  nm for small QDs and  $D_\lambda=200$  nm for large QDs. This indicates stronger absorption in the visible range for larger QDs, which has also been reported in PbS QDs as well as in other types of QDs.<sup>[22, 64, 65]</sup> Table 3 summarizes the penetration depths extracted from the light absorption measurements with the R2 fitting parameters.

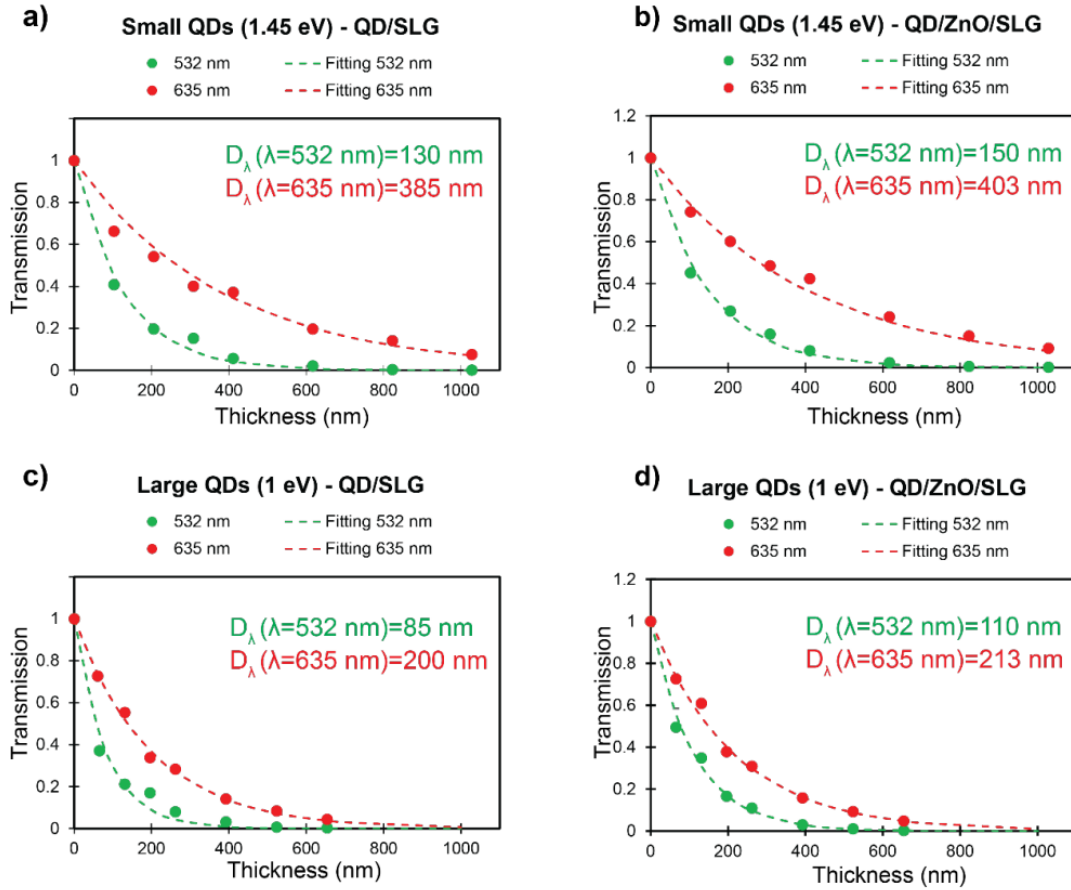


Figure 24 Light penetration depths. a), b), c), d): Transmission as a function of thickness for  $\lambda=532$  nm and  $\lambda=635$  nm through Small QD/SLG, Small QD/ZnO/SLG, Large QD/SLG, and Large QD/ZnO/SLG devices, respectively. The dot points correspond to experimental values and the dashed lines correspond to fittings to Beer-Lambert model ( $e^{-x/D}$ ). The extracted penetration depths ( $D_\lambda$ ) are indicated in each panel. The results are summarized in Table 3.



Table 3 Summary of penetration depth results

	Small QDs, Exciton Peak @ 850 nm				Large QDs, Exciton Peak @ 1320 nm			
	QD/SLG devices		QD/ZnO/SLG devices		QD/SLG devices		QD/ZnO/SLG devices	
<b>Illumination Wavelength</b>	532 nm	635 nm	532 nm	635 nm	532 nm	635 nm	532 nm	635 nm
<b>Penetration Depth <math>D_\lambda</math></b>	130 nm	385 nm	150 nm	403 nm	85 nm	200 nm	110 nm	213 nm
<b>R<sup>2</sup> fitting parameter</b>	0.9936	0.985	0.9955	0.9947	0.9844	0.996	0.9938	0.9925

After measuring the penetration depth, we performed graphene photocurrent measurements in the same samples. A fundamental assumption is that the graphene photocurrent  $I_{ph-SLG}$  is proportional to the density of photocarriers, electrons or holes, at the SLG/QD interface ( $\sim n_{e,h}^{ph}(x = t)$ ) opposite from the incident light surface. The carrier density was modeled in steady state illumination assuming the diffusion model with recombination time ( $\tau$ ) and generation rate ( $G_{ph}$ ) of photocarriers<sup>[38]</sup>:

$$D \frac{d^2 n_{e,h}^{ph}(x)}{dx^2} = \frac{dn_{e,h}^{ph}}{dt} = G_{ph} - \frac{n_{e,h}^{ph}(x)}{\tau} \quad (\text{Eq 2})$$

which in steady state has a solution:

$$n_{e,h}^{ph} \sim A \left( e^{-\frac{x}{L_D}} - e^{-\frac{x}{D_\lambda}} \right) \quad (\text{Eq 3})$$

where  $D_\lambda$  is the wavelength light penetration depth,  $L_D$  is the diffusion length and  $A$  is just a constant that as first approximation does not affect the profile as we work with normalized photocurrent and absorptions. Having obtained the penetration depths  $D_\lambda$  for  $\lambda=532$  and  $635$  nm, we

measured the photocurrent with the same illumination wavelengths and fit our experimental data to Eq 3 to obtaining the values of  $L_{D,h}$  for holes using the direct QD/SLG junction devices (Figure 18 (a) and Figure 20 (a)) and  $L_{D,e}$  for electrons using devices with the ZnO intermediate layer (Figure 18 (b) and Figure 20 (b)). The experiments were carried with Small and Large QDs to explore possible effects of the QD size on diffusion length. In principle, hole and electron diffusion lengths should not depend on light illumination, but as we will see, some variations in  $L_D$  were observed. The experimental results with their corresponding  $L_D$  values based on fittings to Eq. 3 are shown in Figure 25 and the results are summarized in Table 4. For  $\lambda=532$  nm illumination and Small QDs,  $L_{D,h}$  of holes is relatively 180 nm, which is expected for minority carriers in PbS QD, limited typically to  $< 200$  nm. However, for electrons, we observed much longer  $L_{D,e}$ , reaching 500 nm which can be due to their majority carrier nature, reducing recombination events. Remarkably, we observe that  $L_D$  does show a small dependence on wavelength illumination in the case of Small QDs. For small QDs under  $\lambda=635$  nm illumination, we observe that both  $L_D$  of holes and electrons are reduced with respect to  $\lambda=532$  nm illumination:  $L_{D,h}$  is reduced from 180 nm to 140 nm, and  $L_{D,e}$  from 500 nm to 420 nm. These variations cannot be due to variations or measurement errors in thickness as the measurements under both wavelengths are done in the same devices. In the case of Large QDs, the variations in  $L_D$  for holes and electrons between the two different illuminations, are much smaller, with variations of 10 and 5 nm respectively. Another important remark is the impact of the QD size on the diffusion length. For electrons and holes, and for both illuminations,  $L_D$  decreases significantly from Small to Large QDs. For  $\lambda=532$  nm,  $L_D$  for holes decreases from 180 nm in Small QDs to 120 nm in Large QDs, and  $L_D$  for electrons decreases from 500 nm to 150 nm.

Similarly, for  $\lambda=635$  nm,  $L_D$  for holes decreases from 170 nm in Small QDs to 130 nm in Large QDs, and  $L_D$  for electrons decreases from 420 nm to 145 nm.

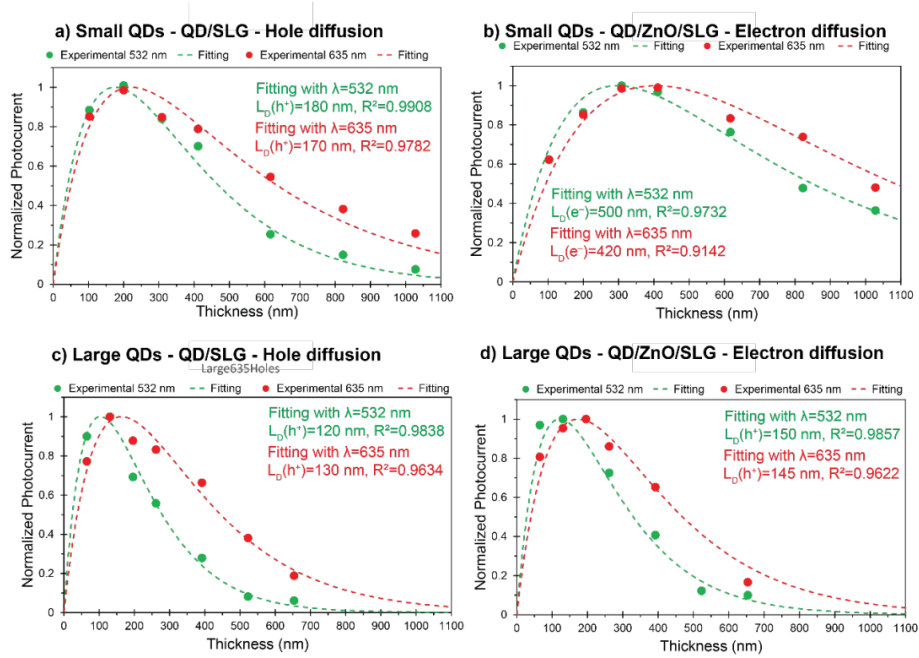


Figure 25 Holes and electron diffusion length. a), b), c), d) Normalized SLG photocurrent as function of thickness under  $\lambda=532$  nm and  $\lambda=635$  nm illumination for Small QD/SLG, Small QD/ZnO/SLG, Large QD/SLG, and Large QD/ZnO/SLG devices, respectively. The dot points correspond to experimental values and the dashed lines correspond to fittings to Eq. 3. The extracted diffusion lengths ( $L_D$ ) with R2 fitting parameters are indicated in each panel. The results are summarized in Table 4.

Table 4 Summary of diffusion length results

	Small QDs, Exciton Peak @ 850 nm				Large QDs, Exciton Peak @ 1320 nm			
	QD/SLG devices		QD/ZnO/SLG devices		QD/SLG devices		QD/ZnO/SLG devices	
	Holes		Electrons		Holes		Electrons	
<b>Illumination Wavelength</b>	532 nm	635 nm	532 nm	635 nm	532 nm	635 nm	532 nm	635 nm
<b>Diffusion Length <math>L_D</math></b>	180 nm	140 nm	500 nm	420 nm	120 nm	130 nm	150 nm	145 nm
<b>R<sup>2</sup> fitting parameter</b>	0.9908	0.9782	0.9732	0.9142	0.9893	0.9634	0.9857	0.9622

The main findings of our measurements are the dependence of the diffusion length on the QD size and, in the case of the Small QDs, the slight reduction in diffusion length for  $\lambda=635$  nm in comparison to  $\lambda=532$  illumination. In the case of the reduction of  $L_D$  for larger QDs, there are two effects to consider. As QDs get larger, there are “less jumps” from dot-to-dot required to achieve the same distance, but on the other hand, the film becomes more porous and less compact with “smaller contact area” between QDs. It is possible that in our case, the second phenomenon may dominate reducing the dot-to-dot conduction. In a previous report, Liu et al reported an opposite behavior in PbSe QDs, with increasing mobility as QD size increased, however, they use field-effect measurements in dark with a bias voltage and very thin films ( $t \sim 30$  nm) that probably involved transport in a depleted regime. Their conditions therefore are significantly different from our case, in which our samples are thicker ( $t > 100$  nm), without a bias, without depletion layers and under illumination with photocarrier population. Therefore, further analysis and experiments are required to understand this behavior and the different trend between Liu et al and our experiments. However, these results clearly indicate that even though the use of the QD size for tuning its bandgap is an advantage, altering the size can also have important effects in charge transport and therefore on

optoelectronic device performance. Therefore, in addition to tuning optical properties using the size, it is important to take into account size effects on transport in QD films.

In regard to the effect of the wavelength on diffusion length, this is observed mainly on Small QDs, and more limited on the Large QDs. The limited effect in Large QDs could be due to the already short  $L_D$ . However, for electrons in Small QD,  $L_{D,e}$  is reduced from 500 nm for  $\lambda=532$  nm to 420 nm for  $\lambda=635$  nm. In principle, the mobility of the photocarriers should be independent of the wavelength of the photon that created them. However, the light penetrations depths are significantly different:  $D_{\lambda=532}=130$  nm and  $D_{\lambda=635}=385$  nm. The shorter  $L_D$  for  $\lambda=635$  nm than for  $\lambda=532$  nm could be due to a second order effect related to interactions with other photogenerated carriers that have a distribution that does depend on the wavelength. For  $\lambda=532$ ,  $D_{\lambda}=130$  nm, so most of the light (80%) is absorbed in the first 200 nm of the QD film (Figure 24 (a)), which means that after 200 nm, the photocarriers will diffuse just limited by traps or recombination but with almost no photons creating more photogenerated charges. However, for  $\lambda=635$  nm,  $D_{\lambda}=385$  nm and 80% of the light is absorbed up to 600 nm in depth, which means that in the first 600 nm of the material, photocarriers will interact with a significant amount of other photocarriers as photons can still generate carriers at such depths. These interactions will result in addition recombination events with other photogenerated carriers, which can result in a reduction of diffusion length. In short, it is possible that illuminations with longer wavelengths, and deeper penetration depths, results in an increase in recombination events between photogenerated carriers, decreasing the diffusion length. The mechanisms herein proposed are just suggested mechanisms, but further measurements and analysis are required for more solid understanding. However, the presented results highlight the

effect that size and illumination wavelengths have on diffusion lengths.

### 3.3 Conclusions

In conclusion, we have presented an effective technique to measure the diffusion length of both electrons and holes in the bulk of thick QD films without the effect of drift currents, field effects, or Fermi level tuning. These values are important for understanding and improving the performance of optoelectronic devices based on QDs. By measuring the light absorption and photocurrent on hybrid QD/SLG devices, it is possible to extract the penetration depth and diffusion lengths by preparing devices with different thicknesses. Our measurements show that QDs with larger size have shorter penetration depths (larger absorption coefficients), as well as shorter diffusion lengths. We suggest that the shorter diffusion length could be due to smaller contact area between QDs, limiting hopping transport, but it is imperative to do more analysis with other variables to determine the causes of this behavior. We also observe that the illumination wavelength also influences the diffusion length, with longer wavelengths showing shorter diffusion lengths. We suggest this is a second order mechanism related to increased interactions between photocarriers for wavelengths with longer penetration depths. Further analysis and measurements are required to understand this behavior, but our results indicates that photocarrier transport in QD films is also affected by the size of the QDs and wavelength illumination.

### 3.4 Fabrication process.

The devices were fabricated on glass substrates with predefined Au/Cr electrodes with 100/10 nm thickness. The electrode geometry gave an active area of 100  $\mu\text{m}$  long channels by 500  $\mu\text{m}$  in

width. In the case of QD/ZnO/SLG devices, a solution with ZnO nanoparticles was added before adding the PbS QDs. The ZnO layer was prepared by spin coating 100  $\mu\text{L}$  of a ZnO nanoparticle in chloroform solution at 2500 rpm for 10 seconds and dried at 200 $^{\circ}\text{C}$  for 10 min, repeating this process 3 times to obtain a  $\sim 110$  nm thick layer. Then the PbS QD layer was prepared by spin coating different number of layers (5, 10, 15, 20, 30, 40, 50). The concentrations of the PbS QDs in toluene were 40 mg/ml for the Small QDs and 30 mg/ml for the large QDs. For spin coating, 0.1 mL were dropped on the substrate for spin coating at 2500 rpm for 10 seconds. Then a 0.03 M tetrabutylammonium iodide (TBAI) in methanol was added and left for incubation for 30 seconds. This process was repeated according to the desired thickness. Their respective thickness for a single coating layer was  $21 \pm 0.6$  nm and  $13 \pm 0.7$  nm for the Small and Large QD respectively. This was estimated from the thickness of  $1050 \pm 30$  nm for 50 layers for Small QDs and  $650 \pm 34$  nm per 50 layers of Large QDs.

Chapter 3, in full, is a reprint of the material as it appears in “Measuring the carrier diffusion length in quantum dot films using graphene as photocarrier density probe”. Seungbae Ahn and Oscar Vazquez-Mena. Submitted. The dissertation author was the primary investigator and author of this paper.

### **$\pi$ - $\pi$ Interactions Mediated Pyrene based Ligand Enhanced Photoresponse in Hybrid Graphene/PbS Quantum Dots Photodetectors**

Hybrid graphene and quantum dots (QDs) photodetectors merge the excellent conductivity and ambipolar electric field sensitivity of graphene, with the unique properties of QDs. A critical aspect for the photoresponsivity of these devices is charge transfer at the graphene/QDs interface. Here we use 1-pyrene butyric acid (PBA)-coated PbS QDs with single layer graphene (SLG) to investigate the effect of pyrene as a  $\pi$ - $\pi$  mediator to enhance charge transfer at the SLG/QDs junction under illumination. The surface chemistry at the QD-QD and SLG/QD interface is studied before and after treatment with the conventional tetrabutylammonium iodide (TBAI) QD linker. The hybrid SLG/QD photodetectors prepared using PBA as a SLG-QD linker demonstrate a photoresponse up to 30% higher than that recorded for devices where only TBAI is used, due to the strong electron coupling between SLG and QDs. Transconductance measurements show that PBA provokes electron depletion in SLG ascribed to the tendency to delocalize the QDs holes, favouring their transfer to SLG. This surface ligand is found to improve the interaction between the QDs light absorbers and the SLG charge collector, leading to an increased photodetection response. Ligand engineering demonstrates able to enhance charge dynamics and thus boost the performance of the hybrid device.

#### 4.1 Introduction

Graphene and semiconducting quantum dots (QDs) offer attractive properties for optoelectronic and sensing applications. Graphene has the highest carrier mobility and its charge



density can be tuned by electrostatic gating, as well as by charge transfer from adjacent materials.<sup>[66, 67]</sup> Semiconducting QDs are excellent light harvesters, present a size-tunable bandgap and can be obtained by low-cost chemical synthesis, resulting highly processable due to their solution dispersibility, and their tunable surface chemistry.<sup>[36, 50, 68]</sup> Recently, hybrid photoconductive detectors, combining QDs as light absorbers and photocarrier generators with graphene or other 2D materials as charge collectors, have attracted great interest due to their ultrahigh gain and high responsivity ( $10^7 \text{ AW}^{-1}$ ), enabling high-sensitivity and gate-tunable photodetection.<sup>[10, 13, 15, 18, 34, 35, 57, 69-72, 73]</sup> Recent advances in hybrid photodetectors combining two-dimensional (2D) materials and PbS or other QDs are summarized in Table 5. In graphene/PbS QD based photodetectors, the band offset at the graphene/QD junction induces a built-in potential that keeps the photogenerated electrons in the QDs and transfers photo-holes to graphene producing a photogating effect, leading to a change of carrier density and a photocurrent under the bias voltage  $V_{SD}$  across graphene, as shown in Figure 26 (a).<sup>[13, 73]</sup> A critical aspect for the performance of these devices is the graphene/QD interface. As shown in Figure 26 (b), QD surface ligands play a major role in the effective transfer of photo-holes from the QDs to graphene. A weak graphene/QD coupling limits the photogenerated carriers from being collected at SLG, leading to more recombination with the opposite carriers or with “trap” states, thus ultimately limiting charge transfer and device photoresponsivity. Currently, the transfer of photo-holes from the QDs to graphene has been made effective by using surface ligands such as tetrabutylammonium iodide (TBAI) or 1,2-ethanedithiol (EDT) that, exchanging the pristine long chain molecule at the QD surface, allow for the charge transfer between QDs, as shown in Figure 1c. Band offset engineering has also been used to improve

charge injection from QDs to graphene. A ZnO layer between graphene and PbS QDs has been used to enhance the built-in potential, driving extraction and collection of charge from the QDs/ZnO p-n junction to the graphene channel, leading to a reverse and an improvement of charge collection.<sup>[73]</sup> Specifically, in such a device, electrons photogenerated in the QDs are transferred to graphene and a responsivity of  $3 \times 10^8 \text{ AW}^{-1}$ , improved of ca. one order of magnitude with respect to the device without ZnO, has been reached.<sup>27</sup> Similarly, an intermediate TiO<sub>2</sub> layer has been used in PbS QDs/MoS<sub>2</sub> hybrid junctions, passivating defect sites and inducing an offset at the MoS<sub>2</sub>/TiO<sub>2</sub>/PbS interface that generates a built-in potential at the TiO<sub>2</sub>/PbS p-n junction, thus facilitating electron transfer to the MoS<sub>2</sub> channel.<sup>[74]</sup> The latter avoids the formation of a high density of localized states in the sub-band-gap region that pin the Fermi level in graphene, and hampers significantly current modulation at the interface, resulting in phototransistors showing a high detectivity of  $5 \times 10^{12}$  Jones in the Vis. Modification of the QD surface chemistry through ligand exchange also allows the modification of energy levels in QD film, thus allowing the engineering of the band offset at the graphene/QD interface.<sup>[75]</sup> In graphene/PbS QD photodetectors the ligand coordinating the QD surface plays a major role in the device performance. In fact, insulating oleic acid (OLEA), that is the pristine QDs ligand, enables inter-QDs charge transfers only via a tunneling mechanism, while shorter ligands improve carrier mobility, that is reported to increase exponentially with the decrease of the ligand chain length.<sup>[54]</sup> The effect of the length of ligand molecules on the charge transfer from QDs to graphene has been studied, showing that short ligands (1~0.5 nm) result in improved responsivity compared to longer ligands (1~5 nm).<sup>[56]</sup> In addition, suitable selected ligands can passivate trap sites at the surface of the QDs increasing lifetime of carriers, and affect valence and

conduction band energy levels, thus modifying the band offset with the Fermi level of graphene.<sup>[51]</sup>

<sup>76]</sup> The described approaches have been applied for improving QD-QD electron transfer and for optimizing the offset of the levels involved in the graphene/QD charge transfer, whereas the improvement of the electron coupling at the graphene/QD interphase for enhancing charge collection at the channel has not been extensively investigated, thus remaining a demanding challenge. Recently, a 3% decrease of the sheet resistance and an effective light energy conversion have been demonstrated by using 1-pyrenebutyric acid (PBA) as a surface ligand for PbS QDs immobilized by  $\pi$ - $\pi$  interactions onto the basal plane of chemical vapour deposition (CVD) grown single layer graphene (SLG), demonstrating that PBA is an effective coupling agent in channeling charge transfer between the hybrid components.<sup>[58]</sup>

Table 5. Summary of recent reports on established advances on hybrid photodetectors combining 2D materials and QDs.

<b>Year</b>	<b>Development in QDs/2D material based photodetectors</b>	<b>Reference work</b>
2012	Demonstration of effective charge transfer between QDs and Graphene	Zhang, D. et al. <i>Understanding Charge Transfer at PbS-Decorated Graphene Surfaces toward a Tunable Photosensor.</i> <sup>[11]</sup>
2012	Demonstration of Ultra High-Gain in Hybrid Gr/QD Photodetectors	Konstantatos, G. et al. <i>Hybrid Graphene–Quantum Dot Phototransistors with Ultrahigh Gain.</i> <sup>[13]</sup>
2012	Infrared Gr/QD Photodetectors with CVD graphene	Sun, Z. et al. <i>Infrared Photodetectors Based on CVD-Grown Graphene and PbS Quantum Dots with Ultrahigh Responsivity.</i> <sup>[34]</sup>
2015	Hybrid PbSe/Gr composite phototransistor	Zhang, Y. et al. <i>Multiheterojunction Phototransistors Based on Graphene-PbSe Quantum Dot Hybrids.</i> <sup>[10]</sup>
2015	Studying the effect of ligand chain on QD/Gr phototransistor	Turyanska, L. et al. <i>Ligand-Induced Control of Photoconductive Gain and Doping in a Hybrid Graphene–Quantum Dot Transistor.</i> <sup>[56]</sup>

Table 5. Summary of recent reports on established advances on hybrid photodetectors combining 2D materials and QDs. Continued.

Year	Development in QDs/2D material based photodetectors	Reference work
2015	Photoactive material based on PbS QDs decorating CVD Graphene monolayer	Ingrosso, C. et al. <i>Photoactive Hybrid Material Based on Pyrene Functionalized PbS Nanocrystals Decorating CVD Monolayer Graphene.</i> <sup>[58]</sup>
2015	Hybrid 2D MoS <sub>2</sub> / PbS QD Photodetector	Kufer, D. et al. <i>Hybrid 2D-0D MoS<sub>2</sub>-PbS Quantum Dot Photodetectors.</i> <sup>[77]</sup>
2016	Integrating a Photodiode and Phototransistor Gr/QD photodetector	Nikitskiy, I. et al. <i>Integrating an Electrically Active Colloidal Quantum Dot Photodiode with a Graphene Phototransistor.</i> <sup>[35]</sup>
2016	Engineering interface between 2D MoS <sub>2</sub> and PbS QD hybrid photodetector	Kufer, D. et al. <i>Interface Engineering in Hybrid Quantum Dot-2D Phototransistors.</i> <sup>[74]</sup>
2016	Hybrid Gr/QD solar cell	Kim, B.-S. et al. <i>High Performance PbS Quantum Dot/Graphene Hybrid Solar Cell with Efficient Charge Extraction.</i> <sup>[49]</sup>
2017	Field-effect phototransistor based on a graphene and lead sulfide quantum dot (PbS QD) hybrid matrix	Song, X. et al. <i>Graphene and PbS Quantum Dot Hybrid Vertical Phototransistor.</i> <sup>[9]</sup>
2017	Graphene/PbS-Quantum Dots/Graphene Sandwich Structures Enabled by Laser Shock Imprinting	Nian, Q. et al. <i>Graphene/PbS-Quantum Dots/Graphene Sandwich Structures Enabled by Laser Shock Imprinting for High Performance Photodetectors.</i> <sup>[78]</sup>
2017	Hybrid 2D MoS <sub>2</sub> HgTe QD hybrid photodetectors	Huo, N. et al. <i>MoS<sub>2</sub> -HgTe Quantum Dot Hybrid Photodetectors beyond 2 <math>\mu</math>m.</i> <sup>[79]</sup>
2017	Image sensor based on Gr/QD photodetector on CMOS readout system	Goossens, S. et al, <i>Broadband Image Sensor Array Based on Graphene-CMOS Integration.</i> <sup>[80]</sup>
2019	Intercalated Multijunction Gr/QD photodetectors	Chen, W. et al. <i>Improved Charge Extraction Beyond Diffusion Length by Layer-by-Layer Multistacking Intercalation of Graphene Layers inside Quantum Dots Films.</i> <sup>[81]</sup>
2019	Metallic VIAs for intercalated Gr/QD Photodetectors	Chen, W. et al. <i>Implementation of Metallic Vertical Interconnect Access in Hybrid Intercalated Graphene/Quantum Dot Photodetector for Improved Charge Collection.</i> <sup>[70]</sup>

Table 5. Summary of recent reports on established advances on hybrid photodetectors combining 2D materials and QDs. Continued.

<b>Year</b>	<b>Development in QDs/2D material based photodetectors</b>	<b>Reference work</b>
2019	Characterization of hybrid Gr/QD photodetector as function of QD size, film thickness and wavelength	Ahn, S. et al. Optoelectronic Response of Hybrid PbS-QD/Graphene Photodetectors. <sup>[12]</sup>
2020	Near unity Quantum Efficiency in NIR with intercalated Gr/QD photodetectors	Chen, W. et al. Near Full Light Absorption and Full Charge Collection in 1-Micron Thick Quantum Dot Photodetector Using Intercalated Graphene Monolayer Electrodes. <sup>[71]</sup>
2020	ZnO intermediate layer for enhanced charge collection in Gr/QD photodetectors	Ahn, S. et al. Enhanced Charge Transfer and Responsivity in Hybrid Quantum Dot/Graphene Photodetectors Using ZnO as Intermediate Electron-Collecting Layer. <sup>[73]</sup>
2021	Tunable Response Time and Responsivity in Graphene-PbS QD Based Hybrid Photodetectors	Sahoo, A. et al. Optical Modulation Frequency Mediated Tunable Response Time and Responsivity in Graphene-PbS QD Based Hybrid Photodetectors. <sup>[59]</sup>
2021	Studying carrier diffusion length in Gr/QD photodetectors	Dutta, R. et al. Enhancing Carrier Diffusion Length and Quantum Efficiency through Photoinduced Charge Transfer in Layered Graphene-Semiconducting Quantum Dot Devices. <sup>[60]</sup>
2021	Patterning of Gr/QD photodetectors using a Gr-PMMA protective layer	Ahn, S. et al High Resolution Patterning of PbS Quantum Dots/Graphene Photodetectors with High Responsivity via Photolithography with Top Graphene Layer to Protect Surface Ligands. <sup>[82]</sup>

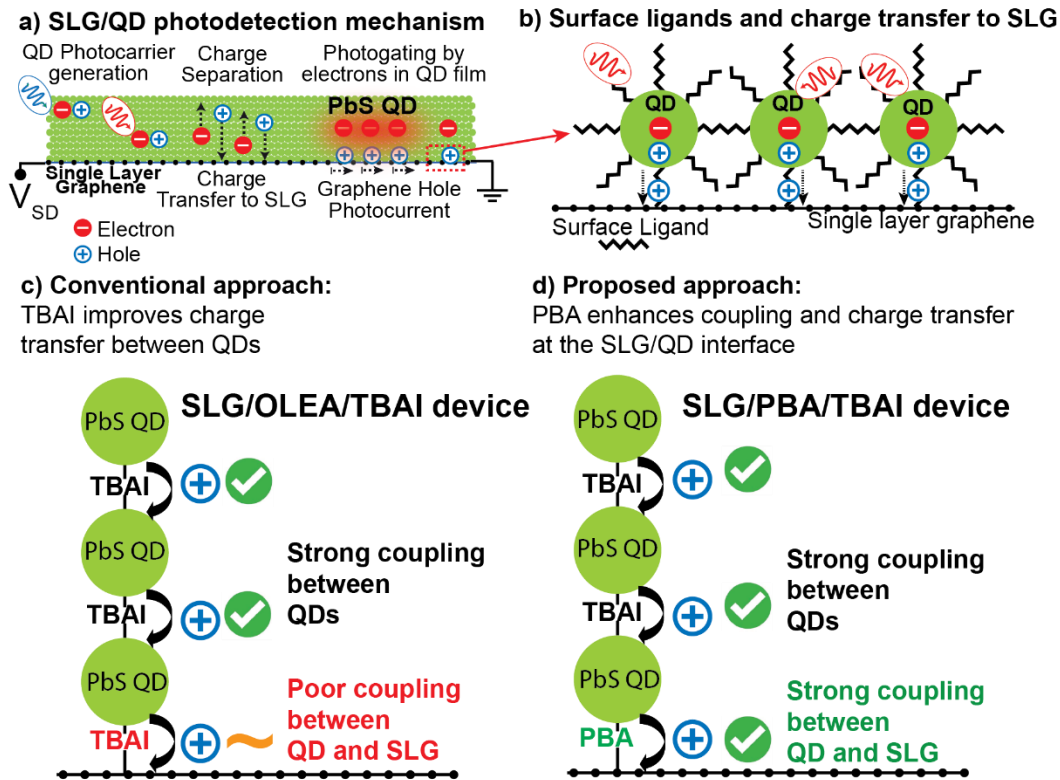


Figure 26 a) Principle of operation in hybrid SLG/QD photoconductive detectors based on carrier photogeneration in QDs and charge transfer to SLG to produce a photocurrent under the bias voltage V<sub>DS</sub> across SLG. b) Surface ligands play an important role in transfer of charges from QDs to SLG. c) Conventional hybrid SLG/QD photodetectors use TBAI to facilitate charge transfer between QDs, but without specific coupling between QDs and SLG. d) Our proposed approach uses PBA as a ligand at the SLG/QD interface to improve electron coupling and enhance charge transfer.

In this work, we report on hybrid photodetectors that use PBA as a ligand between CVD SLG and QDs, while keeping TBAI as a QD–QD ligand, as shown in Figure 26 (d). Maintaining TBAI as a ligand between QDs ensures an efficient transport of photocarriers along the QD layers, while PBA forms a  $\pi$ - $\pi$  bond with SLG enhancing the coupling and improving charge collection from QDs to SLG. The characterization of the prepared PBA-coated PbS QDs shows the effect of PBA on the light absorption and emission of the QDs. The molecular interface between SLG and

PBA-QDs has been investigated by means of FTIR and Raman spectroscopy to elucidate the chemical interactions between QDs and PBA and between the latter and SLG. Then, we have performed transconductance measurements in SLG to study the behavior of the Fermi level in SLG/QDs devices for PBA and non-PBA devices. Finally, the recorded electrical conductivity and photoresponsivity of the photodetectors has shown a 30% enhancement in photocurrent in the PBA/TBAI-QD based architecture (Figure 26 (d)) with respect to the OLEA/TBAI-QD based device (Figure 26 (c)), thus highlighting the effectiveness of the coupling between pyrene and SLG via  $\pi$ - $\pi$  interactions.

#### 4.2 Results and Discussion

Oleic acid (OLEA)-coated PbS QDs have been synthesized by the colloidal chemistry route and then functionalized by a capping exchange procedure with pyrene-1-butyric acid (PBA).<sup>[58, 83]</sup> This aromatic molecule is typically used as a multifunctional anchoring system for carbon based allotropic forms.<sup>[84]</sup> Similarly, here, PBA is expected to link the QDs, which coordinates by its end carboxyl functionality, to the SLG platform by means of  $\pi$ - $\pi$  interactions. In fact, although a direct synthesis of semiconducting PbS QDs in PBA could be, in principle, an interesting strategy to achieve QDs already surface coordinated by PBA, the synthesis of the QDs by using a long alkyl chain surfactant as OLEA has been preferred. The OLEA based route offers reliable control of the nucleation and growth processes in the QDs synthesis essential to achieve a controlled and narrow size dispersion, and to obtain stability in non-polar organic solutions.<sup>[83]</sup> Conversely, for a PBA direct synthesis of PbS QDs, the PBA capability to form highly soluble species for rapid nucleation and then controlled growth to achieve a precise size distribution has yet to be demonstrated. In addition,

the presence of bulky pyrene pendant moiety of the ligands on the surface of PbS QDs would likely hamper their colloidal stability. Therefore, here the post-synthetic ligand exchange of OLEA-capped PbS QDs with PBA has been carried out. To assess the QD surface chemistry modification and the retention of the intrinsic geometry and optical properties, electron microscopy and spectroscopy measurements have been performed before and after treatment with the PBA ligand. The TEM images in Figure 27 (a) display spherical nano-objects having a mean size of ca.  $2.1 \pm 0.5$  nm, that stays unchanged after treatment with PBA (Figure 27 (b)). The UV-Vis-NIR absorption spectrum of the OLEA-QDs (Figure 27 (c)) shows a peak at ca. 788 nm, ascribed to the first allowed exciton transition of QDs having size consistent with that estimated by TEM investigation (Figure 27 (a)).<sup>[6]</sup> The photoluminescence spectrum of the OLEA-QDs (Figure 27 (c)) presents an intense emission peak due to band-edge recombination, Stokes shifted at 939 nm and having a relatively narrow fullwidth at half maximum (FWHM: 91 meV) that accounts for the narrow size distribution of the QDs.<sup>[6]</sup> After exchange with PBA, the absorption spectrum of the QDs significantly broadens, featuring a shoulder that monotonically increases towards the high energy side, whereas the intensity of the emission peak slightly quenches with respect to that of the pristine OLEA-QDs, with a maximum that red-shifts up to 971 nm, and a FWHM that increases up to 130 meV (Figure 27 (c)). These changes in the spectral features can be reasonably explained by the redistribution of the mid-gap surface defect states, induced by desorption of OLEA upon PBA treatment, that reduce QD passivation, turning in a quenching of the emission peak (Figure 27 (c)).<sup>[85]</sup> This is also consistent with the hole acceptor behavior of PBA, which stabilizes them by the  $\pi$  ring system, thus limiting radiative exciton recombination.<sup>[86]</sup> The interactions between SLG and QDs were studied by FTIR



and Raman spectroscopy. Figure 27 (d) reports the infrared spectra of both OLEA- and PBA-QDs, spin-coated onto SLG before and after treatment with TBAI. The typical signals of both PBA and OLEA ligands characterize the high wavenumber region of the spectrum of the PBA-QDs with the aromatic -C-H stretching of pyrene ring at  $3041\text{ cm}^{-1}$ , the weak shoulder of the asymmetric -CH<sub>3</sub> stretching, and the strong asymmetric and symmetric stretching of -CH<sub>2</sub>- of OLEA at around  $2954\text{ cm}^{-1}$ ,  $2923\text{ cm}^{-1}$  and  $2852\text{ cm}^{-1}$ , respectively. All these signals are present also in the pristine OLEA-QDs.

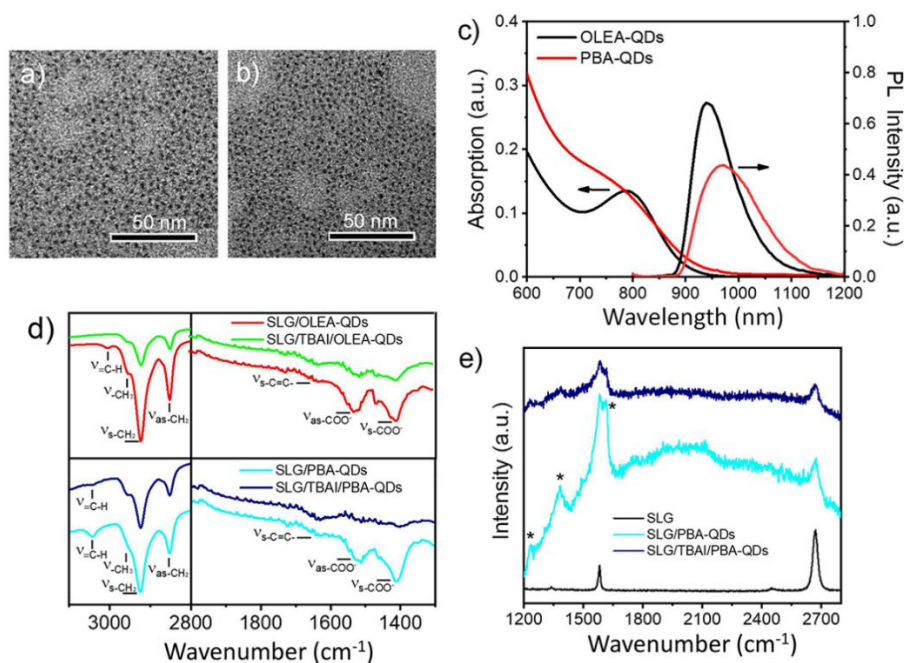


Figure 27 TEM micrographs of (a) OLEA- and (b) PBA-QDs. Steady state UV-Vis-NIR absorption and photoluminescence (PL) spectra of QDs before and after capping exchange with PBA (c). FT-IR absorption spectra of OLEA- and PBA-QDs deposited onto SLG transferred onto glass, before and after treatment by spin-coating with TBAI (d). Raman spectra of bare SLG, and of OLEA- and PBA-QDs on SLG, before and after treatment by spin-coating with TBAI, highlighting with \* the signals ascribed to PBA (e).

Such features indicate that coordination of PBA at the surface of the QDs takes place concomitantly with a partial retention of OLEA.<sup>[58]</sup> In the low wavenumber region, the PBAQDs spectrum presents vibrations at 1511  $\text{cm}^{-1}$  and 1413  $\text{cm}^{-1}$ , observed also in the OLEA-QDs, and accounted for by the antisymmetric and symmetric -COO- stretching modes, respectively, of residual OLEA and PBA both coordinating the QD surface via a bidentate link.<sup>[58]</sup> Interestingly, the lack of a free C=O stretching band of the PBA molecule, expected at 1691  $\text{cm}^{-1}$ , excludes the presence of uncoordinated PBA in the PBA-QDs solution.<sup>[58]</sup> After treatment with TBAI, the intensity of these OLEA related peaks significantly decreases, both in the TBAI treated PBA-QDs and OLEA-QDs, whereas the aromatic -C-H stretching of PBA is still evident as a weak shoulder in the high wavenumber region. These results confirm effective exchange of most of OLEA molecules with TBAI at the QDs surface, and the preservation of part of PBA coordinating molecules therein.<sup>[49]</sup>

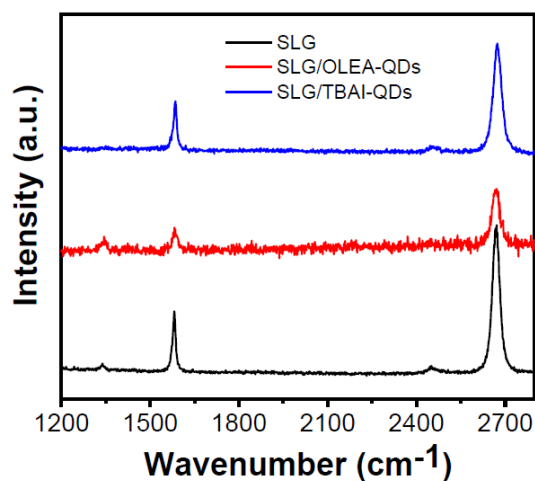


Figure 28 Raman spectra of SLG and OLEA-QDs onto SLG before and after treatment with TBAI.

Raman spectra of the SLG, bare and after deposition of the OLEA- and PBA-QDs, before

and after treatment with TBAI, have been recorded (Figure 27 (e)). SLG shows the G and 2D peaks at  $1581\text{ cm}^{-1}$  and  $2671\text{ cm}^{-1}$  (Figure 27 (e)), respectively, ascribed to the bond stretching between two  $\text{C-sp}^2$  atoms and the second-order breathing modes of  $\text{C-sp}^2$  atoms in hexagonal rings, respectively. Such peaks, that after OLEA-QDs deposition are at  $1582\text{ cm}^{-1}$  and  $2671\text{ cm}^{-1}$ , after TBAI treatment move to  $1585\text{ cm}^{-1}$  and  $2673\text{ cm}^{-1}$ , respectively (Figure 28) likely due to p-doping effect induced by transfer from QDs to SLG of the hole photogenerated upon the intrusive effect of the laser excitation source used for the Raman measurement<sup>[58],[87]</sup> The spectrum of the PBA-QDs deposited onto SLG, before and after treatment with TBAI, shows a broad photoluminescence background signal and new peaks at ca.  $1233\text{ cm}^{-1}$ ,  $1382\text{ cm}^{-1}$  and  $1614\text{ cm}^{-1}$ , marked with \* in the plot (Figure 27 (e)), which are assigned to the  $\text{C sp}^2$  vibration modes of PBA.<sup>[88]</sup> Such spectral features, though weak, are still evident after TBAI treatment, thus further confirming the preservation of PBA molecules coordinating the QD surface. The functionalization of SLG with PBA-QDs does not turn in any defect induced peak (D) in the Raman spectra, thanks to the non-covalent nature of the  $\pi$ - $\pi$  interactions.<sup>[58, 89]</sup> Finally, in the spectrum of the sample after TBAI treatment of the PBA-QDs functionalized SLG, the G and the 2D peaks up-shift up to the same wavenumber observed for the TBAI treated OLEA-QDs,  $1585\text{ cm}^{-1}$  and  $2673\text{ cm}^{-1}$ , as a consequence of the same p-doping effect of QDs upon laser irradiation during the Raman investigation.<sup>[58]</sup> The ensemble of results from FTIR and Raman spectra points out that PBA molecules are preserved after treatment with TBAI of the QDs film onto SLG.

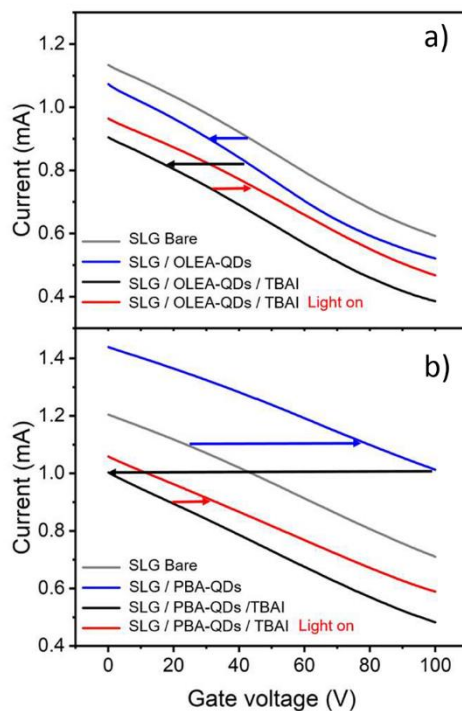


Figure 29 measurements (I vs  $V_G$  @  $V_{DS}=1$  V) for a) bare SLG (grey curve), after deposition of OLEA-QDs (blue curve), after TBAI ligand exchange (black curve), and under illumination ( $\lambda=635$  nm) (red curve), and b) SLG (grey curve), after deposition of PBAQDs (blue curve), after TBAI ligand exchange (black curve), and under illumination ( $\lambda=635$  nm).

Transconductance measurements have been performed to investigate the direction of charge transfers after deposition of QDs onto SLG, and after the different surface treatments, thus providing information about the effectiveness of the charge transfer between materials in the system. The experiments have been performed by measuring the current through SLG, as a function of the gate voltage (I vs  $V_G$ ) under a bias voltage between drain and source ( $V_{DS}$ ) of 1 V. The extent of the shift of  $V_G$  may give indication on the intensity of the charge coupling between the two materials, being higher the shift, more efficient the charge transfer. Figure 3a shows the transconductance

measurements of the SLG samples, as bare, after coating with OLEA-QDs (SLG/OLEA), then after TBAI ligand exchange (SLG/OLEA/TBAI), and finally under illumination of a diode laser at  $\lambda=635$  nm (SLG/OLEA/TBAI Light On). Figure 30 (a and b) show the position of the Fermi level ( $E_F$ ) in SLG inferred from the transconductance measurements. For the bare SLG sample, the negative slope at  $V_G=0$  indicates a p-type doping, as expected for SLG samples transferred onto  $\text{SiO}_2$  substrates. The p-doping state is due to oxygen terminations at the basal plane defects and grain boundaries, to interface effects with the substrate, and to physisorbed contaminants from air, such as  $\text{O}_2$ ,  $\text{H}_2\text{O}$ , and  $\text{CO}_2$ .<sup>[49]</sup> The Dirac point, that stems on the neutrality charge point of the density of state distribution (DOS) of SLG, that is observed as a minimum of the current in the  $I$  vs  $V_G$  plot, is not observed in Figure 29 (a), as the  $V_G$  value, required to reach it, is beyond the range of voltages considered ( $100 \text{ V} < V_G$ ) in the investigated experimental conditions, to prevent breaking the gate dielectric (280 nm thick  $\text{SiO}_2$ ). After spin-coating OLEA-QDs onto SLG, the transconductance trace is shifted to lower  $V_G$  (SLG/OLEA trace is left-shifted in Figure 29 (a), indicating an increase of  $E_F$  (Figure 30 (a)), which can be ascribed to electron transfers from the QDs to SLG, induced by the built-in potential generated at the junction because of a favourable SLG/QDs level off-set (Figure 30 (a)), being the lowest unoccupied molecular orbital (LUMO) state at -3.5 eV as reported for similar OLEA-PbS QDs, just slightly larger, that is an energy higher than the Dirac point of SLG, that is ca. -4.6 eV.<sup>[69, 90, 91]</sup>

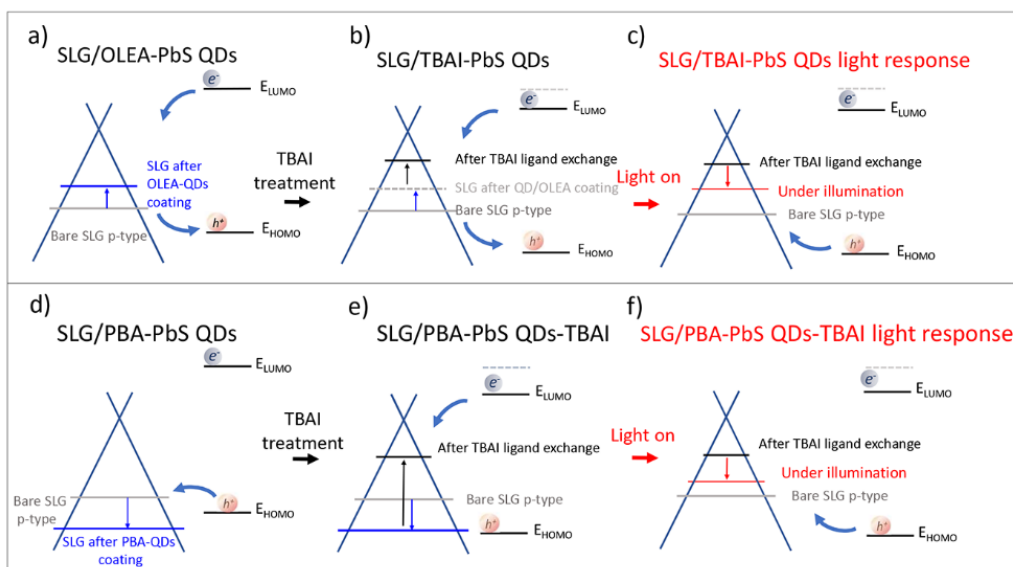


Figure 30 Models of the energy levels behavior trends depicted for SLG a) after deposition of OLEA-QDs, b) after TBAI ligand exchange, and c) upon illumination, on the basis of the transconductance measurements reported in Figure 29 (a) and relative QDs energy levels position from the references<sup>[13, 90-92]</sup> and for SLG d) after deposition of PBA-QDs, e) after TBAI ligand exchange, and f) upon illumination, on the basis of the transconductance measurements reported in Figure 29 (b) and relative QDs energy levels positions from the references.<sup>[91-93]</sup>

After TBAI ligand exchange, the curve is further shifted to lower  $V_G$  (Figure 29 (a)), indicating that  $E_F$  moves further upwards towards the Dirac point (Figure 30 (b)), that still leaving it above. This evidence can be accounted for by coordination of halide ions ( $I^-$ ) that displace OLEA, and behave as an electron-donating QD ligand, lowering the energy of the LUMO level ( $E_{LUMO}$ ) of the QD, and favoring electron transfers to SLG.<sup>[90, 92, 94]</sup> Then, under illumination, the curve has a reverse shift towards larger  $V_G$  (Figure 3a), indicating that the built-in electric field at the SLG/QD interface provides exciton separation at the QDs, with transfer of photoholes from the highest occupied molecular orbital (HOMO) level of the QDs to SLG, shifting  $E_F$  downwards away from

the Dirac point (Figure 30 (c)), whereas photoelectrons stay in the QDs.

The transconductance behavior of SLG after coating with PBA-QDs (Figure 29 (b)) shows a striking difference from that of OLEA-QDs (Figure 29 (a)). The bare SLG still presents the p-type behaviour with the Dirac point beyond  $V_G$  of 100 V. However, after deposition of PBA-QDs, the curve (SLG/PBA) has a significant shift towards higher  $V_G$  (Figure 29 (b)), indicating a large electron depletion that shift  $E_F$  downwards away from the Dirac point (Figure 30 (d)). This finding can be ascribed to the tendency of the aromatic ligand to delocalize the QD photoholes increasing the  $E_{HOMO}$  level of QDs, thus favoring holes transfer to SLG.<sup>[93]</sup> After treatment with TBAI (SLG/PBA/TBAI), the curve shift is largely reversed towards lower  $V_G$  (Figure 30 (e)) with again a rise in  $E_F$  due to the lowering of  $E_{HOMO}$  of the TBAI treated PBA-QDs, the latter induced by the electron-donating I, recovering the same behavior observed for SLG/OLEA/TBAI. Finally, under illumination, the transconductance is shifted to higher  $V_G$ , again for the transfer of photoholes from the QDs to SLG and shifting  $E_F$  downwards (Figure 30 (f)). The large shift of  $E_F$  in the opposite direction upon deposition of PBA-QDs on SLG with respect to OLEA-QDs, suggests a strong interaction between the QDs and SLG, that can be ascribed to PBA-mediated  $\pi$ - $\pi$  interactions between the SLG basal plane and the QDs. After the TBAI exchange, charge flow through the QDs is improved, and thus electronic equilibrium between SLG and QD films can be reached, resulting in a comparable built-in potential between QD and SLG, and, thus, in a photoresponse similar for both OLEA/TBAI and PBA/TBAI devices.

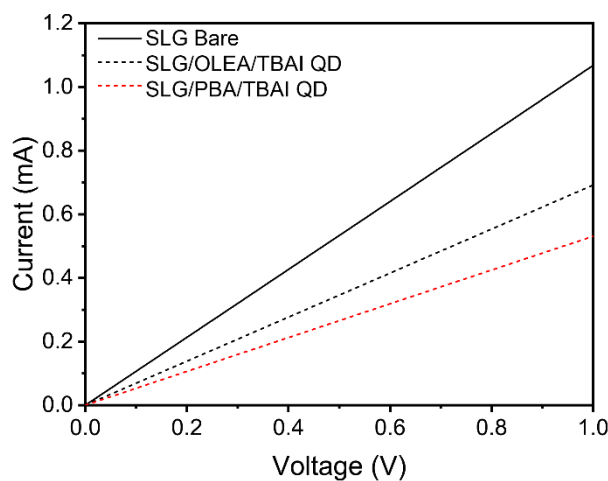


Figure 31 I/V measurements for bare SLG, SLG/OLEA/TBAI, and SLG/PBA/TBAI samples, showing reduction in conductance after QD deposition.

The current vs. bias voltage (I/V) characteristics of bare SLG, SLG/PBA/TBAI and of SLG/OLEA/TBAI devices also offer evidence of the PBA-mediated interactions between SLG and QDs. I/V curves are shown in Figure 31, showing that after deposition of either PBA-QDs and OLEA-QDs on SLG, and their subsequent treatment with TBAI, the conductivity of the samples is reduced with respect to bare SLG samples. This is consistent with the electron transfers taking place from the QDs to SLG, which reduce holes majority carrier density. Taking averages over 5 measurements, we obtain a resistance of  $968.00 \pm 2.05 \Omega$  for bare SLG,  $1446.00 \pm 5.02 \Omega$  for SLG/OLA/TBAI, and  $1884.00 \pm 1.72 \Omega$  for SLG/PBA/TBAI. The stronger reduction in conductivity for SLG/PBA/TBAI than for SLG/OLEA/TBAI with respect to bare SLG is probably due to the stronger electron coupling between QDs and SLG, due to the delocalization of charge in PBA.<sup>[93]</sup>



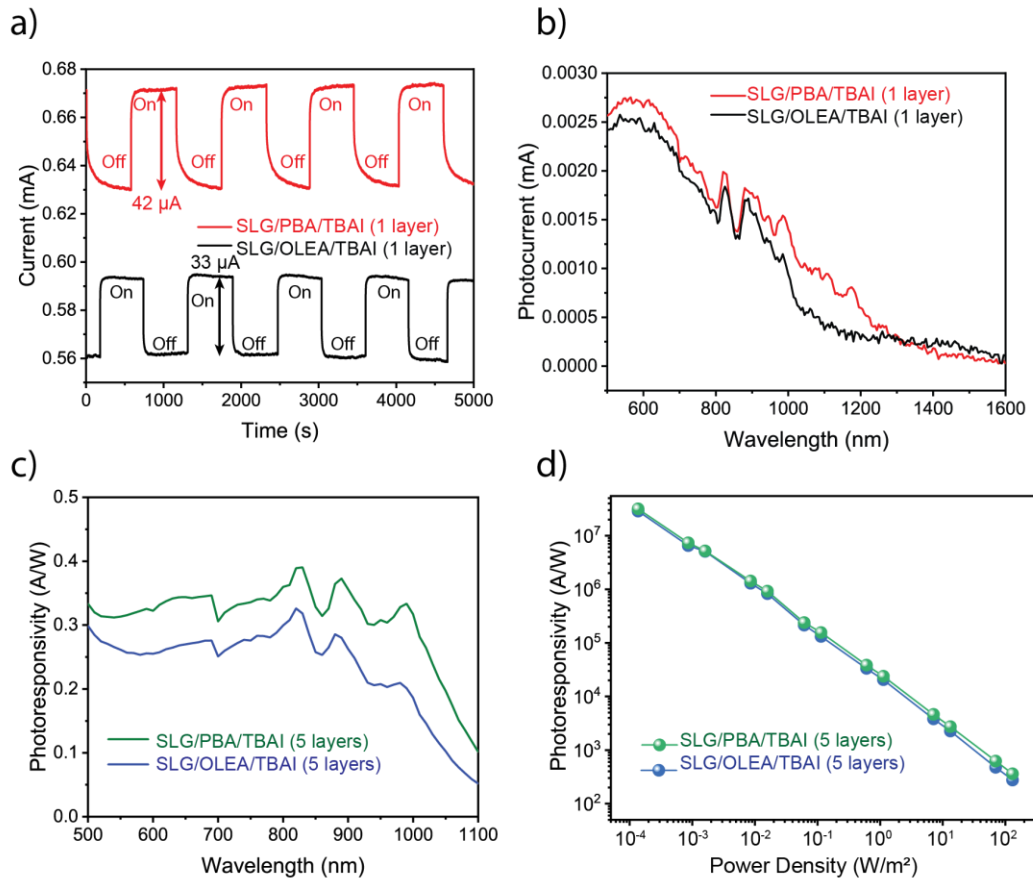


Figure 32 a) Photoresponse of the SLG/OLEA/TBAI and SLG/PBA/TBAI devices collected under ON/OFF light stimulation ( $\lambda = 635$  nm,  $14.33$   $\text{mW}/\text{cm}^2$ ,  $V_{\text{bias}} = 1$  V). b) Photocurrent as a function of light wavelength, showing higher photocurrent for SLG/PBA/TBAI devices through the  $\lambda \sim 600-1200$  nm range. c) Photoresponsivity as a function of wavelength for thicker devices made of 5 spin-coated layers of QDs, showing the improved responsivity of SLG/PBA/TBAI devices over SLG/OLEA/TBAI devices. d) Photoresponsivity as a function of light intensity for 5 spin-coated QD layers, showing higher responsivity at lower intensity for both SLG/OLEA/TBAI and SLG/PBA/TBAI devices.

The photoresponse of hybrid SLG/QD photodetectors has been assessed by comparing the performance of the SLG/OLEA/TBAI devices in which TBAI acts as both QD-QD and SLG/QD ligand (SLG/OLEA/TBAI device in Figure 26 (c)), versus SLG/PBA/TBAI devices in which PBA

induces a strong coupling between SLG and QD (SLG/PBA/TBAI device in Figure 26 (d)). The fabrication is discussed in more detail in the Methods section. The thicknesses of the QD films were  $28.21 \pm 4.58$  nm for 1 layer of SLG/OLEA/TBAI and  $28.37 \pm 3.64$  nm for 1 layer of SLG/PBA/TBAI. The photoresponse of the devices has been collected under ON/OFF light stimulation ( $\lambda = 635$  nm,  $100 \text{ mWcm}^{-2}$ ,  $V_{\text{bias}} = 1$  V) as shown in Figure 32 (a). The SLG/PBA/TBAI device generates a photocurrent of  $42 \mu\text{A}$  while the SLG/OLEA/TBAI device produces  $33 \mu\text{A}$ , which means a  $\sim 30\%$  improvement in photoresponse. The higher photocurrent observed in the SLG/PBA/TBAI device with respect to the SLG/OLEA/TBAI photodetector can be explained considering the presence of PBA molecules that act as a transfer channel of the holes photogenerated in the QDs to SLG via delocalization in the aromatic  $\pi$  electron system. The rising (OFF $\rightarrow$ ON) and recovery (ON $\rightarrow$ OFF) times of the SLG/OLEA/TBAI and SLG/PBA/TBAI devices were extracted by exponential fitting of the transient photocurrent time response (see Figure 33-32). SLG/OLEA/TBAI devices have a rising time of 69.98 ms and recovery time of 853.24 ms and SLG/PBA/TBAI devices have slower transients, with rising time of 101.64 ms and a recovery time of 2.11 s (Table ). As can be noticed from Table , the response time presents two components; a fast one, in the order of ms, that can be ascribed to the direct transfer of photocarriers from the QDs to SLG and a slow one, in the order of s, that can be, instead, related to surface trap states that slow down the release of carriers.<sup>[95]</sup> The longer times of the SLG/PBA/TBAI device can be attributed to the delocalization of charge in the PBA ring which mediates the charge transfer between SLG and the QDs. In addition, both SLG/OLEA/TBAI and SLG/PBA/TBAI devices show slower time components ( $> 1$  s) due to the interface traps as reported previously.<sup>[13, 94]</sup>

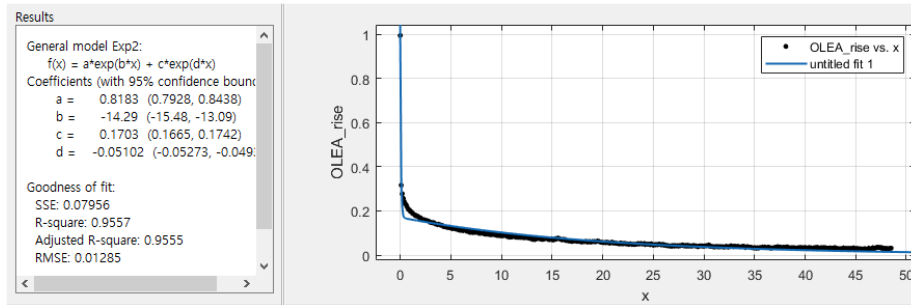


Figure 33 SLG/OLEA/TBAI rising time (Light OFF → ON) achieved by fitting the transient photocurrent time response of Figure 32.

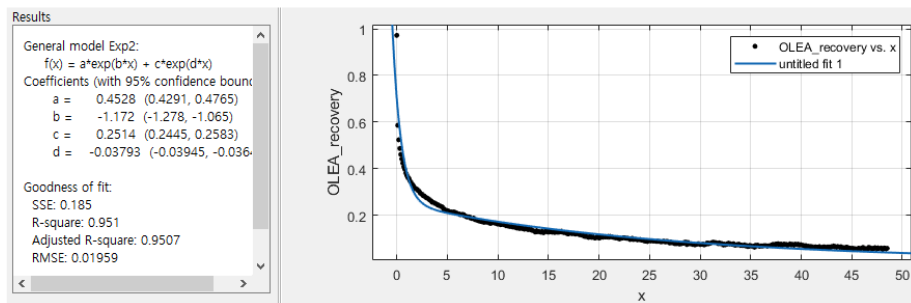


Figure 34 SLG/OLEA/TBAI recovery time (Light ON → OFF) achieved by fitting the transient photocurrent time response of Figure 32.

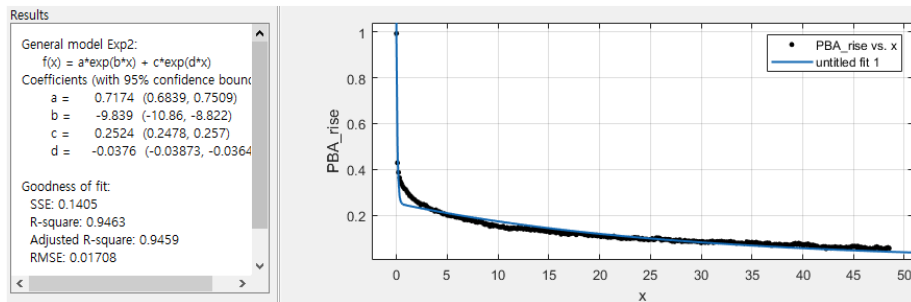


Figure 35 SLG/PBA/TBAI rising time (Light OFF → ON) achieved by fitting the transient photocurrent time response of Figure 32.

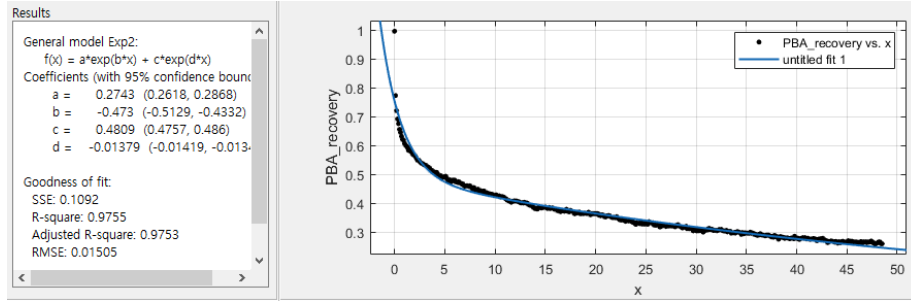


Figure 36 PBA/TBAI recovery time (Light ON → OFF) achieved by fitting the transient photocurrent time response of Figure 32.

Table 6 Rise and Recovery times of SLG/OLEA/TBAI and SLG/PBA/TBAI devices.

	Rise time (OFF to ON) (s)		Recovery time (ON to OFF) (s)	
	Fast component	Slow component	Fast component	Slow component
<b>SLG/OLEA/TBAI</b>	0.06998	19.6	0.85300	26.0
<b>SLG/PBA/TBAI</b>	0.10164	26.6	0.00211	72.0

Figure 32 (b) highlights how SLG/PBA/TBAI device exhibits a photoresponse higher than that shown by SLG/OLEA/TBAI device through the entire spectrum, from  $\lambda \sim 600$  nm to 1200 nm. The photocurrent spectral response of the SLG/OLEA/TBAI and SLG/PBA/TBAI devices, recorded for one layer of QDs (Figure 32 (b)), shows a high photoresponsivity matching the absorption spectra of the QDs in solution (Figure 27 (b)), whereas no photocurrent is observed for photon energies below the bandgap of the QDs, because photocarriers generation from SLG is not expected to yield photoconductance due to their ultrafast recombination.<sup>[96]</sup> The current traces under different wavelengths with the dark current reference is shown in Figure 37. These evidences assess the spectral selectivity of the manufactured SLG/QD photodetector, and hence, the possibility to tune

spectral responsivity by changing the QD band gap.

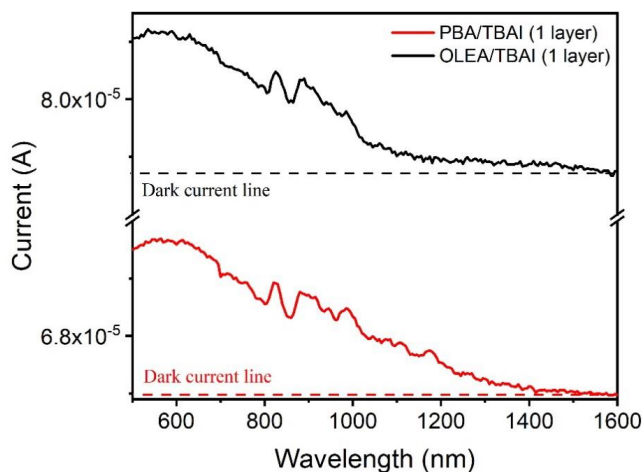


Figure 37 Raw data from the spectral response measurement. The current under 40 mV bias is measured for each wavelength step with an integration time of 10 s.

Since light absorption and responsivity of the hybrid SLG/QD photodetector are limited by the low thickness (ca. 30 nm) of the film obtained upon a single deposition of QDs, devices with a higher number of layers are required to increase light absorption, especially in the Vis-NIR range, where radiation has a penetration depth higher than 200 nm. In Figure 32 (c) the spectral photoresponsivity of thicker devices, obtained, by i. depositing 5 layers of OLEA-QDs, being each of them ligand exchanged by using a TBAI solution, and ii. by depositing 4 layers of OLEA QDs, undergoing each a ligand exchange with TBAI, onto a first layer of PBA-QDs. In this way, PBA is expected to anchor by  $\pi$ - $\pi$  interactions onto SLG, while QD-QD coupling is ensured by TBAI (Figure 26 (d)).<sup>[58, 89, 97]</sup> The photoresponsivity as a function of wavelength shows the higher responsivity for the SLG/PBA/TBAI device through the ~600-1200 nm range, proving its higher performance also for thicker films. Figure 6d shows the dependence of responsivity on light density

extracted from I/V curves taken at different light intensities shown in Figure 38. The responsivity of the SLG/PBA/TBAI devices drops with light intensity, following the same trend as SLG/OLEA/TBAI devices and as reported in previous reports of hybrid SLG/QD photodetectors.<sup>[13, 18, 34]</sup> This behavior is due to larger recombination rates at high light influx, reducing the number of the photogenerated holes that can reach the SLG/QDs interface. At low intensities of  $\sim 10^{-12}$  Watts ( $\lambda=635$  nm), the responsivity is  $3 \times 10^7$  AW<sup>-1</sup>, which is in line with the magnitude found for such hybrid SLG/QD devices.<sup>[12, 13, 34, 35, 73]</sup> These results show that the use of PBA QDs as a priming layer enhances the responsivity performance of SLG/QD devices through a stronger interaction between the two nanomaterials, but also induces a slower response.

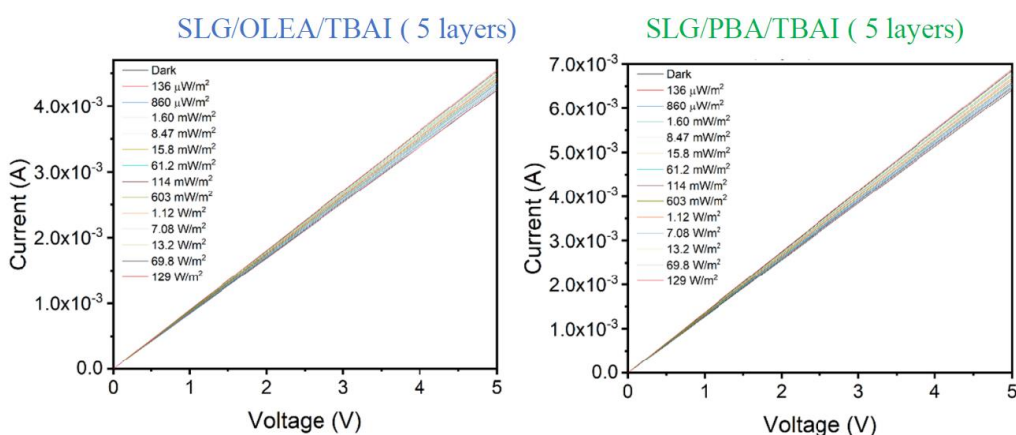


Figure 38 I/V curves of SLG/QD devices at different light intensities ( $\lambda=635$  nm)

### 4.3 Conclusion

In conclusion, we have presented a novel strategy tailoring the surface ligands according to their roles: TBAI has been used to achieve a strong QD–QD coupling, while PBA, a pyrene based

ligand, present as a capping ligand coordinating the surface of the first layer of QDs, has been used to enhance SLG-QD coupling via  $\pi$ - $\pi$  interactions. We have demonstrated that PBA ligand has a negligible effect on the light absorption edge of the NCs, which is the main factor affecting the photodetector performance. FTIR and Raman analysis demonstrate that PBA serves as an effective linker between QDs and SLG, that, via the carboxyl group of pyrene, creates a stable  $\pi$ - $\pi$  bond that retains its coupling role even after TBA exchange. Transconductance measurements also suggest that PBA-SLG interactions result in electrons participating in  $\pi$ - $\pi$  bonds between PBA and SLG. The photoresponse measurements show that the improved responsivity is uniform across different wavelengths in the  $\lambda$ -600-1200 nm range, reasonably due to the more effective electron coupling at the SLG/QD junction provided by the PBA linker, which acts as a channel in transferring the charge to the delocalized  $\pi$  electrons system of SLG. Slower response times for PBA/TBAI are also observed due to the same  $\pi$ - $\pi$  interactions that would need to be addressed for applications requiring high speeds. However, the higher responsivity achieved in this work demonstrates that ligand engineering can enhance the performance of hybrid devices based on nanomaterials, where interface engineering plays a major role in charge exchange dynamics.

#### 4.4 Experimental section

Materials: 1-pyrene butyric acid (PBA), lead(II) oxide (PbO, powder 99.99%), hexamethyldisilathiane (HMDS, synthesis grade), trioctylphosphine (TOP, 90% technical grade), methanol (CH<sub>3</sub>OH  $\geq$  99.8%) and chloroform (CHCl<sub>3</sub>,  $\geq$  99.8%) were purchased by Sigma-Aldrich and used as received. Tetrabutylammonium iodide (TBAI), 1-Octadecene (ODE, 90% technical grade) and oleic acid (OLEA, technical grade 90%), also purchased by SigmaAldrich, were distilled

before use. Single layer graphene (SLG) was purchased from Graphenea.

Synthesis of OLEA-capped PbS QDs: The preparation of PbS QDs was carried out as previously reported.<sup>35</sup> In a typical synthesis, 4 mmol of PbO, 3 mL of trioctylphosphine (TOP) and 2.35 g of oleic acid (OLEA) were added to 36 mL of 1-octadecene (ODE) and stirred under vacuum at 120°C. Then, a 2 mM solution of sulfur precursor, hexamethyldisilathiane (HMDS) in ODE, was rapidly injected, followed by fast cooling at room temperature. The obtained QDs were purified by centrifugation adding to the reaction product a large amount of ethanol and the precipitate was then dispersed in CHCl<sub>3</sub>

Capping exchange of OLEA-capped PbS QDs with 1-pyrene butyric acid (PBA): The ligand exchange was carried out under inert atmosphere as reported in the reference.<sup>[58]</sup> First, as synthesized 10<sup>-2</sup> M QDs were repeatedly washed with cycles of precipitation by centrifugation and redispersion in CH<sub>3</sub>OH to remove the excess of OLEA ligand coordinating the QDs surface. A 0.5 M PBA solution in CHCl<sub>3</sub> was added to the washed QDs and the mixture was left to stir overnight at room temperature. The QDs were then washed with repeated cycles of precipitation by centrifugation and redispersion with CH<sub>3</sub>OH to remove the aromatic ligand in excess and then re-dispersed in CHCl<sub>3</sub> for further studies. A concentrated transparent solution of 10<sup>-2</sup> M PBAQDs in CHCl<sub>3</sub> was obtained.

Material characterization: Steady state UV–Vis absorption spectra were recorded with a Cary 5000 (Varian) UV/Vis/NIR spectrophotometer. Steady state photoluminescence spectra were collected by using a Fluorolog 3 spectrofluorimeter (HORIBA Jobin–Yvon), equipped with double grating excitation and emission monochromators. All optical measurements were performed at room



temperature. TEM analyses were performed using a Jeol Jem-1011 microscope, operating at 100 kV and images were acquired by a Quemesa Olympus CCD 11 Mp Camera. The samples were prepared dipping a 300 mesh amorphous carbon-coated Cu grid in  $\text{CHCl}_3$  solution of QDs and leaving the solvent to dry. Size statistical analysis (NPs average size and size distribution) of the samples were performed by freeware ImageJ analysis program. At least 150 QDs were counted for each sample.

Graphene transfer: SLG was transferred onto the substrate by PMMA wet-transfer.<sup>[98, 99]</sup> The PMMA/graphene layer on copper was left floating on a 0.1 M sodium persulfate solution until the copper was dissolved. Then the PMMA/graphene layer was transferred to two subsequent DI water baths and finally to the target device and left drying. Finally, PMMA is removed by acetone and isopropanol.

Deposition of QDs onto SLG: SLG/OLEA/TBAI type devices were fabricated by spin coating (2500 rpm for 10 s) 0.1 ml of  $10^{-2}$  M OLEA-QDs in  $\text{CHCl}_3$  onto CVD SLG. Then, ligand exchange was performed, after each layer deposition, by incubation in a 0.03 M TBAI  $\text{CH}_3\text{OH}$  solution for 30 s, and then rinsing with  $\text{CH}_3\text{OH}$ . SLG/PBA/TBAI devices were prepared, the first was obtained by spin coating 1 layer of 0.1 ml of  $10^{-2}$  M PBA-QDs in  $\text{CHCl}_3$  followed by ligand exchange with TBAI and rinsing with  $\text{CH}_3\text{OH}$ . The thickness of the QD films was measured by ellipsometry (Rudolph Auto EL Ellipsometer).

Spectral photoresponse characterization: The spectral response was performed over wavelengths from 500 to 1200 nm with a 5 nm step size with a monochromator. The calibration to obtain the power intensity at each wavelength was performed before data collection using a silicon photodiode (S-120VC, Thorlabs). Light was generated by a Xe arc lamp with a Newport CS260 UV-

Vis monochromator to select desired wavelengths. The experiment was done by measuring the current through graphene at a fixed voltage (40 mV) with a time integration of 10 s at each wavelength. The photocurrent was extracted by measuring the current under different wavelengths and subtracting the dark current.

Light intensity photoresponse: Photoresponsivity versus power intensity experiment was performed by combining neutral density filters with optical densities (transmission) of 0.3 (50%) , 1.0 (10%), 2.0 (1%) and 3.0 (0.1%) from Thorlabs (NE503A, NE510A, NE520A, and NE530A). A CPS635R laser diode (red,  $\lambda \sim 635$  nm) with a circular beam with diameter of 2.9 mm was used. The calibration for a laser power was performed prior to data collection using a silicon photodiode (S-120VC, Thorlabs). The graphene channel had a width of 100  $\mu\text{m}$  and length of 100  $\mu\text{m}$ , resulting in an active area of 0.0001  $\text{cm}^2$ . The photocurrent was measured from the photocurrent at a bias voltage of 5 V.

Time response analysis: Rising and recovery times were estimated by fitting the time response with a two-components exponential decay functions. The rising (ON $\rightarrow$ OFF) times were obtained by normalizing and inverting the response to obtain the decay behavior and fitting to an exponential behavior. The recovery (OFF $\rightarrow$ ON) times were obtained by normalizing the response and fitting to an exponential decaying behavior. In both cases MATLAB was used and the results give a two-component exponential behavior, with a fast and a slow component.

Chapter 4, in full, is a reprint of the material as it appears in “ $\pi$ - $\pi$  Interactions Mediated Pyrene based Ligand Enhanced Photoresponse in Hybrid Graphene/PbS Quantum Dots Photodetectors”. Seungbae Ahn, Chiara Ingrosso, Annamaria Panniello, Marinella Striccoli,

Giuseppe Valerio Bianco, Angela Agostiano, Giovanni Brunoc, Maria Lucia Curri, and Oscar Vazquez Mena, *Advanced Electronic Materials*, Accepted. The dissertation author was the primary investigator and author of this paper.

### **Enhanced Charge Transfer and Responsivity in Hybrid Quantum Dot/Graphene Photodetectors Using ZnO as Intermediate Electron-Collecting Layer**

Hybrid graphene (Gr)-quantum dot (QD) photodetectors have shown ultrahigh photoresponsivity combining the strong light absorption of QDs with the high mobility of Gr. QDs absorb light and generate photocarriers that are efficiently transported by Gr. Typically, hybrid PbS-QD/graphene photodetectors operate by transferring photogenerated holes from the QDs to Gr while photoelectrons stay in the QDs inducing a photogating mechanism that achieves a responsivity of  $6 \times 10^7 \text{ A W}^{-1}$ . However, despite such high gain, these systems have poor charge collection with quantum efficiency below 25%. Herein, a ZnO intermediate layer (PbS-QD/ZnO/Gr) is introduced to improve charge collection by forming an effective p-n PbS-ZnO junction driving the electrons to the ZnO layer and then to Gr. This improves the photoresponsivity of the devices by nearly an order of magnitude with respect to devices without ZnO. Charge transfer to Gr is demonstrated by monitoring the change in Fermi level under illumination for conventional PbS-QD/Gr and for ZnO intermediate PbS-QD/ZnO/Gr devices. These results improve the capabilities of hybrid QD/Gr configurations for optoelectronic devices.

#### 5.1 Introduction

Light to electricity conversion is a fundamental process required in a broad range of optoelectronic applications such as imaging, photovoltaics, and telecommunications.<sup>[30, 99, 100]</sup> While

current technologies are mainly based on inorganic materials (Si, GaAs, GaN) and low-cost organic molecules, nanomaterials with extraordinary electronic and optical properties are emerging for next generation optoelectronic devices.<sup>[2, 101]</sup> Quantum dots (QDs) offer size-tunable band gaps, strong light absorption, easy solution-based processing, and further capabilities with core-shell compositions.<sup>[28, 102]</sup> Similarly, 2D materials have shown extraordinary high mobilities like in graphene (Gr), as well as high light adsorption/emission with transition metal dichalcogenides monolayers.<sup>[8, 103]</sup> However, the implementation of nanomaterials into high performing optoelectronic devices still faces several challenges. QD films have very poor mobility, resulting in poor photocarrier collection.<sup>[62]</sup> One-atom thin Gr has extraordinary mobility and stability, but it lacks a bandgap and is ultrathin, resulting in poor light absorption.<sup>[67]</sup> 2D semiconductors also offer high responsivity but do not offer the band gap size tunability of QDs. A novel strategy to overcome such limitations was demonstrated by combining Gr and PbS-QDs into hybrid Gr/QD photodetectors.<sup>[9-13, 34, 35, 70, 80, 81]</sup> These devices exploit the synergy between these two materials, combining the strong light absorption and bandgap tunability of QDs for carrier photogeneration, with the high mobility of single-layer Gr for efficient charge transport resulting in ultrahigh gain ( $\approx 10^8$  electrons/photon) and responsivity ( $\approx 10^7$  A W<sup>-1</sup>).<sup>[13, 15, 104]</sup> In addition to single QD/Gr devices, multistacked QD/Gr devices with intercalated Gr layers have also been reported, showing improved photoresponsivity.<sup>[70, 81]</sup> All previously reported PbS-QD/Gr hybrid devices operate by transferring photogenerated holes from QDs to Gr.<sup>[11, 56]</sup> The long lifetime of electrons staying in the QDs acting as a photogate, combined with the short transit time of holes through the Gr channels result in high gains. However, the charge transfer from QDs to Gr is poor. The highest quantum efficiency (QE)

reported in single PbS-QD/ Gr junction is 25%, probably due to a low built-in potential that limits the force driving photogenerated holes from PbS-QDs to Gr. In this work, we add an intermediate ZnO layer in between the PbS-QDs and the Gr layer (PbS/ZnO/Gr), forming a PbS-ZnO p-n junction that reverses and improves the device operation by transferring photogenerated electrons, instead of holes, from the PbS QDs to Gr. This strategy has been demonstrated using a P3HT layer to enhance charge transfer from perovskites to Gr.<sup>[105]</sup> Surface ligands have also been optimized resulting in high responsivities using short-length ligands, but also resulting in hole-transfer from QDs to Gr.<sup>[56]</sup> In this work, the ZnO intermediate layer operates as an efficient electron collecting layer driving electrons from QDs to Gr.

The hybrid photodetectors herein presented are constructed by a high mobility single-layer Gr, a ZnO intermediate layer, and a light absorbing PbS-QDs layer. From here on, these devices will be referred to as intermediate PbS/ZnO/Gr devices, and the control devices without ZnO will be referred to as control PbS/Gr devices. Gate-sweep measurements are performed to monitor the Fermi level and carrier concentration in Gr. We observe that in the case of control PbS/Gr devices, the Fermi level of Gr decreases under illumination, pointing to transfer of holes from the QDs to Gr, whereas for PbS/ZnO/Gr devices, the Fermi level increases under illumination, indicating electron transfer. We show that PbS/ZnO/Gr devices have more efficient charge transfer with higher photoresponsivity than PbS/Gr devices.

## 5.2 Results and Discussion

### 5.2.1 Device Fabrication and Material Characterization

In brief, the devices are fabricated by transferring CVD Gr monolayers on a 500  $\mu\text{m}$  thick silicon chip with a thermal  $\text{SiO}_2$  layer 285 nm thick used as gate dielectric. The chip has predefined electrodes with a channel length/width of 500  $\mu\text{m}$ /500  $\mu\text{m}$  on top of the  $\text{SiO}_2$ . Field-effect measurements indicate that bare Gr is p-doped, with the gate voltage ( $V_G$ ) required to reach the Dirac point ( $V_{\text{DP}}$ ) located at  $V_{\text{DP}} \approx 80\text{--}120$  V for various devices. An I versus  $V_G$  plot is shown in Figure 39 (a). Using a value of  $V_{\text{DP}} \approx 100$  V for bare Gr, we estimate that the Fermi level ( $E_F$ ) is  $\approx 0.28$  eV below the Dirac point in the valence band. This is consistent with previous works on hybrid Gr/QD photodetectors reporting bare Gr monolayers on  $\text{SiO}_2$  as p-type channels.<sup>[13]</sup> The resistances of various Gr samples are shown in Figure 39 (b). Figure 39 (c) shows the Raman spectrum of a Gr monolayer. After Gr transfer, ZnO nanoparticles are spin-coated on the Gr layer followed by an annealing process at 200  $^\circ\text{C}$  to form continuous films. The thickness of the ZnO is controlled by the number of spin-coated layers, with each ZnO layer being about 35 nm in thickness. PbS QDs films are deposited by spin coating followed by a ligand exchange using tetrabutylammonium iodide (TBAI). The thickness of one spin-coated layer is  $\approx 30$  nm for PbS QDs. SEM cross sections of ZnO/Gr and PbS-QD/Gr devices are shown in Figure 40 (a and b), showing full coverage on Gr layers. UV-vis absorption spectra of ZnO, PbS-QDs, and PbS-QD/ZnO films are shown in Figure 40 (c–e). XRD patterns of a ZnO films are shown in Figure 40 (f), confirming its crystallographic structure. After adding either PbS QDs or ZnO nanoparticles,  $E_F$  of Gr shifts upward toward the Dirac point, shifting  $V_{\text{DP}}$  from  $\approx 100$  to  $\approx 50\text{--}60$  V, staying p-type in agreement with previous works

on hybrid PbS-QD/Gr devices (see Figure 39 (d)).<sup>[13, 81]</sup>

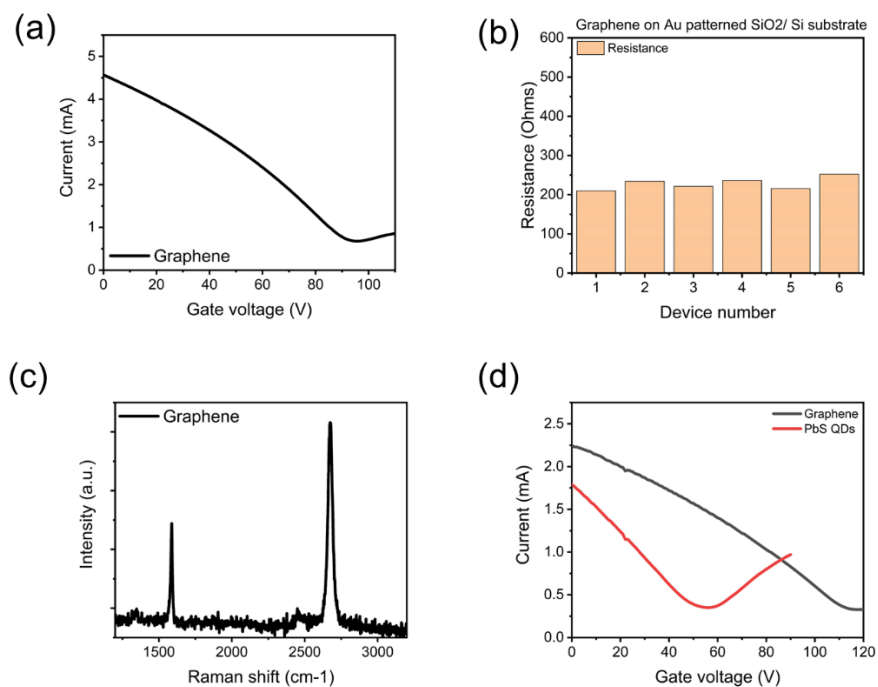


Figure 39 a) I vs VG for a bare graphene sample, showing the Dirac peak at  $V_{DP} \sim 90$  V and that graphene is p-type. b) Resistance histogram of different graphene samples with channel length and width of  $500 \mu\text{m}$ . c) Raman spectrum of single layer graphene. d) Shift in  $V_{DP}$  for graphene from  $\sim 115$  V to  $\sim 55$  V after PbS quantum dots coating. This indicates that the Fermi level is up-shifted towards the Dirac point, but that graphene remains p-doped.



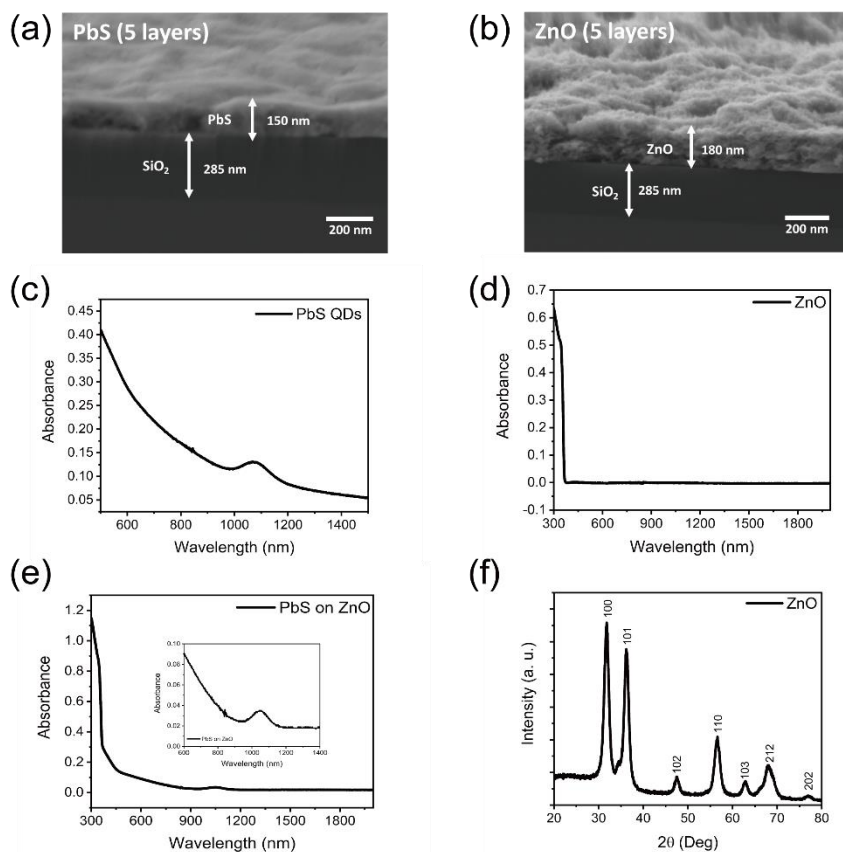


Figure 40 a) Five layers of PbS QDs coated on 285 nm of SiO<sub>2</sub>. The thickness of PbS quantum dots is 150 nm, indicating a thickness of 30 nm per layer. b) Five layers of ZnO coated on 285 nm of SiO<sub>2</sub>. The thickness is 180 nm, indicating a thickness of  $\approx 36$  nm per layer. c) UV-vis absorption spectra of PbS QDs, showing a resonance peak at  $\lambda = 1090$  nm. d) UV-vis absorption spectra of a ZnO layer, showing a strong response at  $\lambda = 300$  nm, but negligible response for higher wavelengths. e) UV-vis spectrum of PbS quantum dots on ZnO, showing an overlap of the spectra in (c) and (d). The resonance peak from ZnO can be observed at  $\lambda = 300$  nm as well as the weaker absorption peak from PbS QDs at  $\lambda = 1090$  nm. f) X-ray diffraction patterns of ZnO layer.

### 5.2.2 Charge Transfer to Gr

The primary effect of the intermediate ZnO layer in the transfer of photogenerated charges from PbS to Gr is shown in Figure 41, illustrating PbS/Gr and PbS/ZnO/Gr device diagrams with

their respective light and dark electrical current as function of gate voltage ( $I$  vs  $V_G$ ). In the case of the direct PbS/Gr junction (Figure 41 (a)), the gate voltage to reach the Dirac point ( $V_{DP}$ ) shifts from  $V_{DP} = 57$  V in dark to  $V_{DP} = 80$  V under light ( $\lambda = 635$  nm) as shown in Figure 41 (b). The positive shift of  $V_{DP}$  under illumination indicates a downshift of Fermi level and therefore a transfer of photogenerated holes from the PbS-QDs to Gr. In contrast, for the PbS/ZnO/Gr device (Figure 41 (c)),  $V_{DP}$  shifts negatively under illumination, from  $V_{DP} = 40$  V in dark to  $-12$  V under light (Figure 41 (d)), indicating an upshift in Fermi level and therefore a transfer of photogenerated electrons to Gr. We infer that ZnO forms an effective p-n junction with the PbS-QDs (PbS/ZnO), transferring photogenerated electrons from PbS to ZnO that are then collected and transported by Gr.

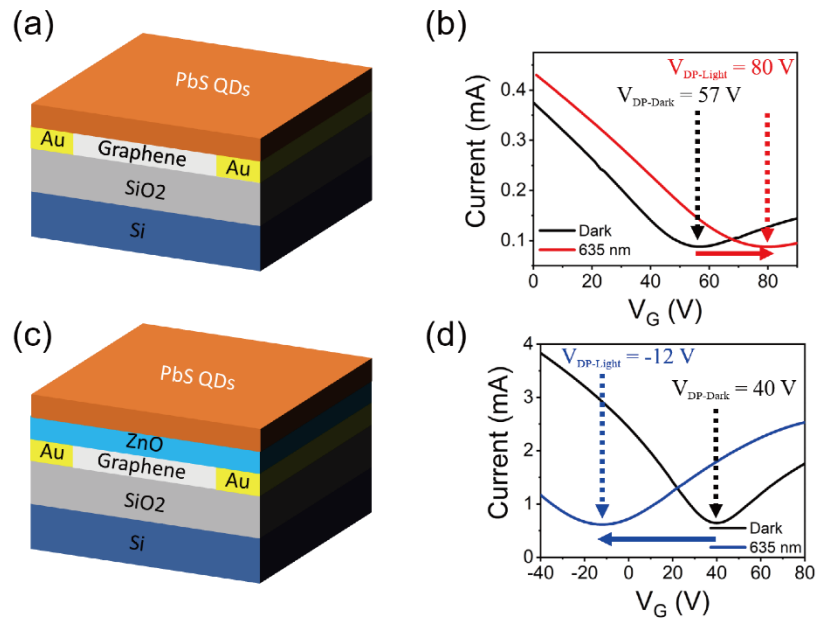


Figure 41 a) PbS/Gr device schematics. b) I versus  $V_G$  for a PbS/Gr device in dark (black) and under  $\lambda = 635$  nm light (red), showing the positive shift of the Dirac point from  $V_{DP} = 57$  to  $80$  V in light, indicating a downshift in Fermi level and transfer of photogenerated holes to Gr under light. c) PbS/ZnO/Gr device schematics. d) I versus  $V_G$  for PbS/ZnO/Gr in dark (black) and under  $\lambda = 635$  nm light (blue), showing the negative shift from  $V_{DP} = 40$  V in dark to  $-12$  V in light, indicating an upshift in Fermi level and the transfer of photogenerated electrons to Gr under light. ( $V_{DS} = 1$  V).

In order to gain understanding on the charge transfer to Gr, the resistance and Fermi level of Gr were measured in PbS/Gr and ZnO/Gr junction devices. Figure 42 (a) shows the electrical resistance of Gr as function of PbS film and ZnO film thickness. For PbS/Gr, the resistance jumps from  $\approx 250 \Omega$  without PbS (thickness  $t = 0$ ), to  $\approx 550 \Omega$  after the first layer of PbS ( $t = 30$  nm) is added. This initial drastic shift in EF indicates a transfer of electrons from PbS to Gr, reducing the number of hole majority carriers. As more PbS QD layers are added, the resistance of Gr keeps increasing up to  $900 \Omega$  for  $t = 120$  nm. Figure 42 (b) shows how  $V_{DP}$  decreases as PbS layers are added, indicating an upward shift in  $E_F$  toward the Dirac point. Even though from  $t = 30$  to  $60$  nm,

there is a slight increase in  $V_{DP}$ , from  $t = 60$  to  $120$  nm,  $V_{DP}$  decreases from  $\approx 60$  to  $\approx 35$  V. The behavior of resistance and  $V_{DP}$  as function of thickness indicates that adding more PbS layers adds more electrons to Gr. Since adding more PbS-QD layers keeps shifting the Fermi level, we infer that the depletion layer at the PbS/Gr junction extends at least to  $\approx 120$  nm in the QDs. From the Fermi level shift in Gr, we infer a PbS/Gr interface with accumulated negative charges in Gr and positive charges in PbS generating a built-in potential. Under illumination, this built-in potential drives photogenerated holes to Gr and keeps photoelectrons in PbS. In the case of the ZnO/Gr device, the trends are different. Figure 3a shows that after adding the first ZnO layer, there is an initial increase in resistance from  $\approx 220$  to  $\approx 450$   $\Omega$ . However, as more layers of ZnO are added, the resistance of Gr does not change significantly, remaining near  $\approx 450$   $\Omega$  up to  $t = 140$  nm. Similarly,  $V_{DP}$  does not show major changes, remaining at  $\approx 55$  V from  $t = 35$  to  $140$  nm (Figure 42 (b)). From this behavior, we infer a narrow depletion layer ( $\approx 30$  nm) and possibly lower built-in potential at the ZnO/Gr interface compared to the PbS/Gr interface. It is important to mention that in the case of the PbS/Gr junction, surface ligands have a strong effect on band alignment and charge transfer that also affect the interface between PbS and Gr.<sup>[75, 106]</sup> In the case of ZnO/Gr junctions, the ZnO nanoparticles are deposited without intermediate molecules on Gr.<sup>[107]</sup> Figure 43 shows the complete set of  $I$  versus  $V_G$  plots from which  $V_{DP}$  are extracted for Figure 42 (b).

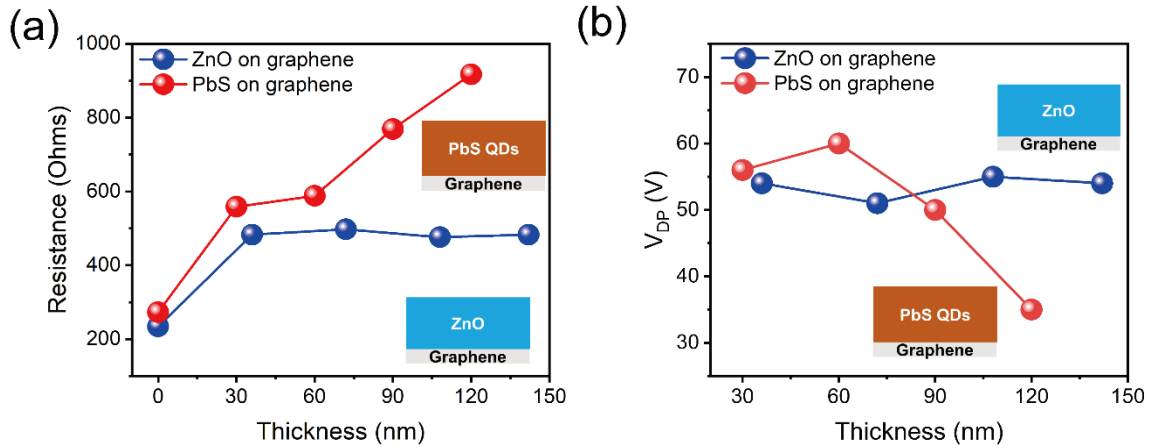


Figure 42 a) Resistance as a function of thickness for PbS/Gr and ZnO/Gr. For PbS/Gr the resistance increases from  $R \approx 250$  to  $900 \Omega$  as the thickness increases from  $t = 0$  to  $120$  nm. For ZnO/Gr the resistance increases from  $R \approx 220 \Omega$  to  $500 \Omega$  as the thickness increases from  $t = 0$  to  $35$  nm but remains constant from  $t = 35$  to  $140$  nm. b) Dirac point gate voltage ( $V_{DP}$ ) as a function of thickness. For PbS/Gr,  $V_{DP}$  increases slightly from  $t = 30$  to  $60$  nm, but then decreases from  $t = 60$  to  $120$  nm as PbS QDs are added. For ZnO/Gr,  $V_{DP}$  remains stable as ZnO is added from  $t = 35$  to  $140$  nm. The complete set I versus VG plots for different thicknesses of PbS and ZnO on Gr from which  $V_{DP}$  are extracted are shown in Figure 43 (a and b).

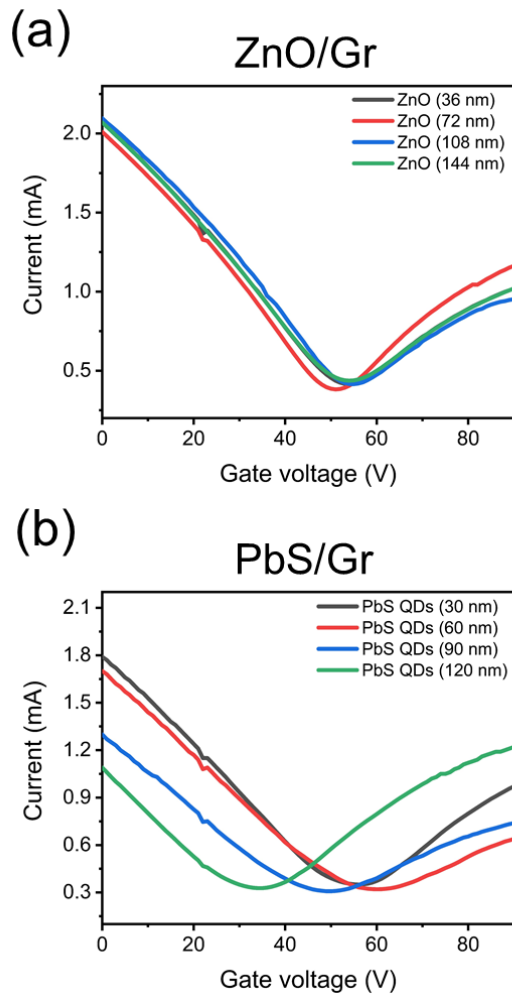


Figure 43. Full I vs VG curves for ZnO/Gr and PbS/Gr as function of ZnO and PbS thickness respectively from which  $V_{DP}$  is extracted for Figure 42 (b) in the main text. a) For ZnO, the shifts in  $V_{DP}$  are minor as more ZnO layers are added. b) For PbS, there is slight initial right shift in  $V_{DP}$  from  $t=30$  nm to  $t=60$  nm, but as  $t$  is increased to  $t=90$  and  $t=120$  nm there is a clear negative shift in  $V_{DP}$ . The shifts in  $V_{DP}$  for PbS are clearly more significant than for ZnO.

### 5.2.3 Photoresponse of PbS/Gr and PbS/ZnO/Gr Devices

The inverted photoresponse under  $\lambda = 635$  nm illumination for the control PbS/Gr and the

intermediate PbS/ZnO/Gr devices is shown in Figure 45. In both cases, the thickness of the PbS layer is  $\approx 30$  nm, and for the intermediate device the ZnO layer is  $\approx 110$  nm thick. A ZnO/Gr control device shows negligible response at  $\lambda = 635$  nm as shown in Figure 44; therefore, it is assumed that the photoresponse in PbS/ZnO/Gr devices is due to light absorption by the PbS layer. Figure 45 (a and b) shows the photocurrent  $I_{\text{ph}} = I_{\text{light}} - I_{\text{dark}}$  as function of  $V_G$ . For PbS/Gr (Figure 45 (a)), at  $V_G = 0$  the photocurrent  $I_{\text{ph}}$  is positive as photogenerated holes are transferred from PbS to Gr, increasing the carrier density and therefore the conductivity of the p-type Gr channel. For values of  $V_G < 40$  V,  $I_{\text{ph}}$  is positive, and it increases as  $V_G$  increases because the  $E_F$  upshifts toward the Dirac point and the impact of photoholes transferred to Gr has a larger effect on its hole carrier density as  $E_F$  gets closer to the Dirac point.  $I_{\text{ph}}$  reaches its maximum at  $V_G \approx 40$  V, which corresponds to the Dirac point in dark ( $V_{\text{DP-Dark}}$ ). As  $V_G$  increases above 40 V,  $I_{\text{ph}}$  decreases as now Gr is n-type in dark but becomes p-type under illumination due to photoholes transferred from PbS, reducing effectively  $I_{\text{ph}}$ . This trend continues, passing by a zero-response ( $I_{\text{ph}} = 0$ ) point near  $V_{\text{G-Zero}} = 68$  V, at which the n-type Gr electron carrier density in dark is equal to the p-type Gr hole carrier density under illumination. Passing the zero-response,  $I_{\text{ph}}$  becomes negative and keeps decreasing, hitting a minimum at  $V_G \approx 80$  V, corresponding to the Dirac point under illumination ( $V_{\text{DP-Light}}$ ). The maximum and minimum points of  $I_{\text{ph}}$  in Figure 45 (a) can also be correlated to the dark and light Dirac points in Figure 41 (b) (not same devices), since  $I_{\text{ph}}$  closely matches to the difference between the dark and light curves, with the zero-response point  $I_{\text{ph}} = 0$  at the crossing between the two curves. Figure 46 (a) has a diagram showing how Fermi level and carrier concentration shifts in Gr under illumination, explaining the photocurrent behavior. In the case of the PbS/ZnO/Gr device, the behavior is similar

but inverted. At  $V_G = 0$ ,  $I_{ph}$  is negative, indicating that photoelectrons are transferred to p-type Gr, decreasing the net carrier hole density. From  $V_G = -50$  to  $-35$  V,  $I_{ph}$  is negative and decreases until reaching a minimum at the Dirac point under illumination at  $V_{DP-Light} = -35$  V. From this point, Gr still behaves as p-type in dark, but now it converts to n-type under illumination due to photoelectrons transferred from PbS. The zero-response ( $I_{ph} = 0$ ) is reached at  $V_{G-Zero} = 22$  V, where the hole carrier concentration in dark is equal to the electron carrier concentration under light.  $I_{ph}$  keeps increasing until reaching a maximum at the Dirac point in dark at  $V_{DP-Dark} \approx 45$  V. From there, Gr now behaves as n-type in dark and photoelectrons transferred to Gr increase its conductivity, keeping  $I_{ph}$  positive. As  $V_G$  increases above  $V_{DP-Dark}$ ,  $I_{ph}$  keeps positive, but its magnitude decreases because the impact of photoelectrons in the carrier density diminishes as EF shifts upward away from the Dirac point. This behavior can also be understood from Figure 41 (d), (not same devices) since  $I_{ph}$  corresponds to the difference between dark and light curves. Shifts in Fermi level in Gr under illuminations are shown in Figure 46 (b) Given that in both intermediate PbS/ ZnO/Gr and control PbS/Gr devices Gr is p-type ( $V_{DP} > 0$  V), the inverted behavior of  $I_{ph}$  in Figure 45 (a and b) provides strong evidence of transferring of photo-electrons from QDs to Gr in PbS/ZnO/Gr devices and photo-holes in PbS/Gr devices.



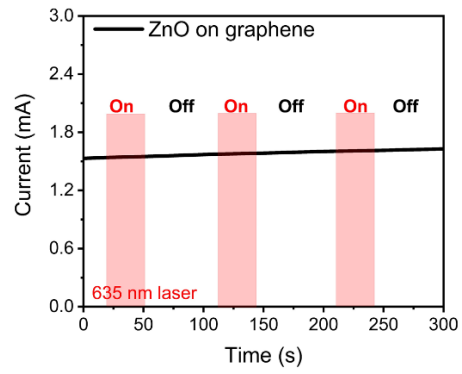


Figure 44 Current response under a  $\lambda=635$  nm laser of a ZnO/Gr structure, showing the zero response of the system since  $\lambda =635$  laser cannot create photocarriers in ZnO due to its high band gap.

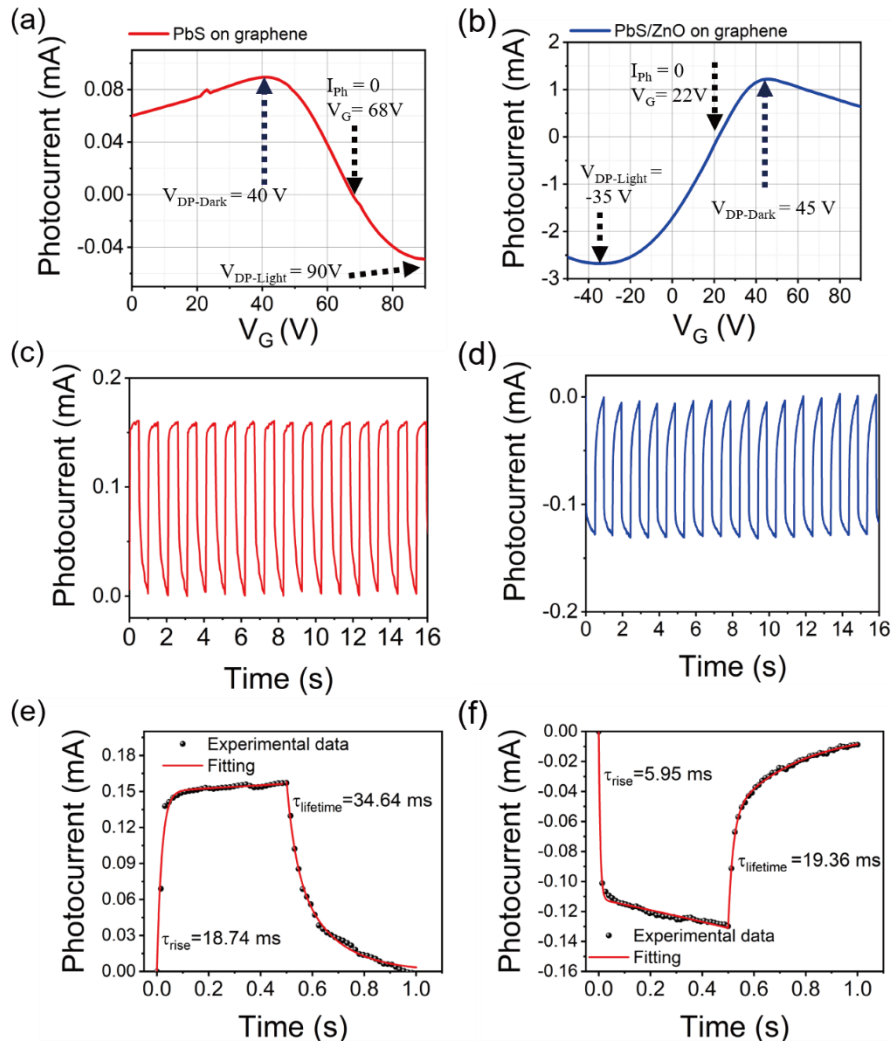


Figure 45 a)  $I_{ph}$  versus  $V_G$  for PbS(30 nm)/Gr. At  $V_G = 0$ , the photoresponse is positive due to photoholes transferred to p-type Gr. The maximum and minimum relate to the Dirac points in dark and light respectively. b)  $I_{ph}$  versus  $V_G$  for PbS(30 nm)/ZnO(110 nm)/Gr. At  $V_G = 0$ , the photoresponse is negative due to photoelectrons transferred to p-type Gr. The minimum and maximum relate to the Dirac points in dark and light respectively. c,d) Time response for ON/OFF light switching for PbS/Gr and PbS/ZnO/Gr. The current increases for light ON for PbS/Gr, while it is reduced for PbS/ZnO/Gr. e,f) Rising and recovery times for PbS/Gr and PbS/ZnO/Gr devices. Illumination:  $\lambda = 635$  nm and laser frequency modulation: 2 Hz.

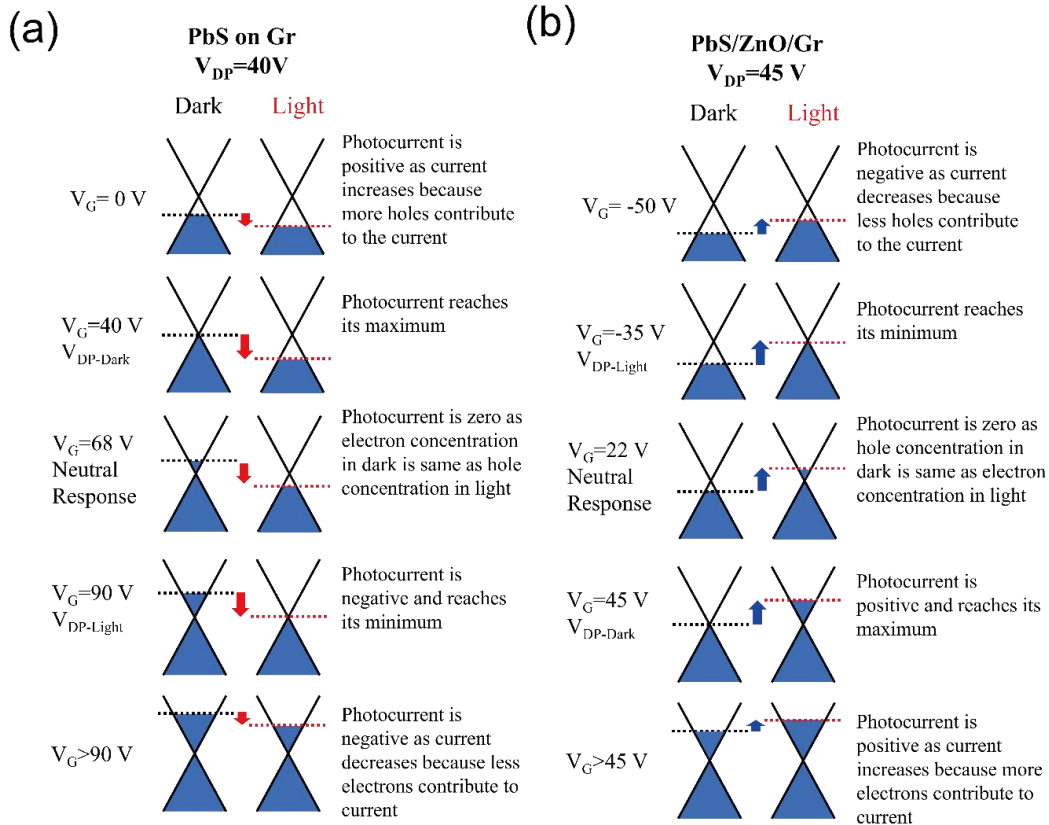


Figure 46 Band diagrams of PbS/Gr and PbS/ZnO/Gr showing the shift in Fermi level under illumination for representative  $V_G$ .

Time-modulated response for both devices are shown in Figure 45 (c and d). Both cases show time modulation below 1 s with good time stability. The detailed response and recovery times are shown in Figure 45 (e and f). For PbS/Gr, the current increases (positive  $I_{ph}$ ) with a response time of 18.74 ms and a slower recovery time of 34.64 ms. In the case of the PbS/ ZnO/Gr device, the light response is a decrease in current with a faster response time of 5.95 ms and a recovery time of 19.36 ms. The response times are similar to previous results using PbS/Gr (10 ms) and PbS/MoS2 (12 ms) junctions, but still below Gr/QD devices with an ITO top-gate encapsulation reaching sub-

millisecond response.<sup>[13, 35, 74]</sup> The recovery time has a second time component of  $\approx 1$  s associated with surface traps as reported previously.<sup>[13, 15, 74, 77]</sup> Measurements for wide switching time interval (10 mHz) were also investigated to understand the stability in ambient air-condition as shown in Figure 47. Both PbS/Gr and PbS/ZnO/Gr devices have good stability under ambient condition with exposure time of about 1 h. Proper encapsulation is also required since QDs are known to be sensitivity to humidity and further work is needed to study performance in extreme conditions such as high humidity and for longer time periods.

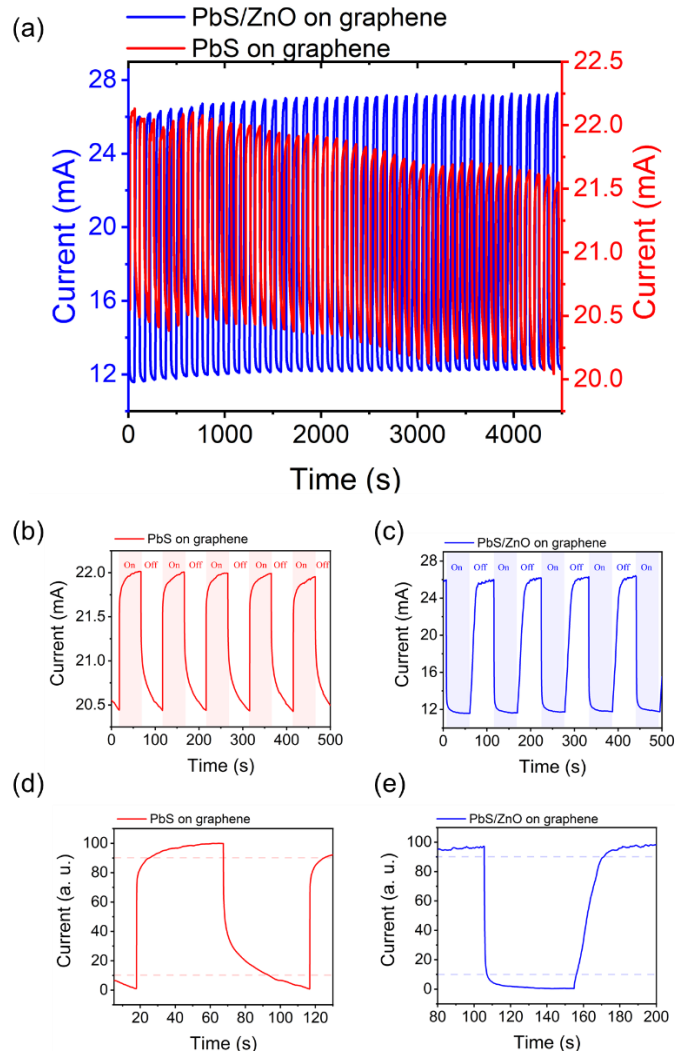


Figure 47 Time response for ON/OFF light switching for PbS/Gr and PbS/ZnO/Gr (a) with long time exposure (>1 hour), (b) and (c) 5 cycles, and (d) and (e) one cycle. Illumination:  $\lambda=635$  nm and light frequency modulation: 10 mHz.

#### 5.2.4 Enhanced Photoresponsivity and Charge Collection

Figure 48 (a) shows the spectral response for PbS/ZnO/Gr and PbS/Gr devices, showing a superior performance of intermediate ZnO devices in the  $\lambda \approx 500\text{--}1100$  nm range. In both cases

there is a strong response in the  $\lambda \approx 500\text{--}800$  nm range, followed by a drop in Responsivity ( $R_{\text{ph}}$ ) at  $\lambda \approx 800$  nm which has also been observed in other PbS/Gr reports.<sup>[12, 13, 81]</sup> Light with  $\lambda > 800$  nm has a large penetration depth ( $>500$  nm) and is poorly absorbed by the 90 nm PbS-QD thick film. However, the Responsivity peak due to the QD first-exciton resonance absorption peak at  $\lambda \approx 1050$  nm shows a strong response matching almost the response in the visible range. Overall, the performance of the device with intermediate ZnO layer shows a  $R_{\text{ph}}$  10-times higher than the direct PbS/Gr devices. Figure 48 (b) shows  $R_{\text{ph}}$  as function of incident power P, giving a similar 10-times improvement for intermediate PbS/ZnO/Gr over PbS/Gr devices from  $10^{-4}$  to  $10^1$  mWcm $^{-2}$ . (I-V and I vs  $V_G$  plots for various incident power illumination are shown in Figure 49 (a and b)). At low powers of  $10^{-4}$  mWcm $^{-2}$ , the intermediate ZnO devices reach a  $R_{\text{ph}} \approx 10^8$  AW $^{-1}$  which is superior to  $10^7$  AW $^{-1}$  reached previously by PbS/Gr devices.<sup>[13]</sup> PbS/ZnO/Gr device also results in improved detectivity ( $D^*$ ), indicating  $D^* = 1.06 \times 10^{12}$  Jones (NEP =  $4.2 \times 10^{-14}$  WHZ $^{-0.5}$ ) and  $D^* = 5.63 \times 10^{10}$  Jones (NEP =  $7.95 \times 10^{-13}$  WHZ $^{-0.5}$ ) for PbS/Gr device. As shown in Figure 50, the noise levels for PbS/ZnO/Gr and PbS/Gr devices are very similar, therefore, the higher responsivity results in higher detectivity.<sup>[14]</sup> In both cases, PbS/Gr and PbS/ZnO/Gr, a reduction in  $R_{\text{ph}}$  is observed toward higher incident power. This behavior has been also reported for QD/Gr devices and is due to reduced  $\tau_{\text{lifetime}}$ , saturation of traps, and less efficient charge transfer at high light intensities as modeled by Sun et al.<sup>[34]</sup> Figure 48 (c) shows how  $V_{\text{DP}}$  shifts from dark to light as function of light intensity with expected opposite shifts for PbS/Gr and PbS/ZnO/Gr devices. The shift in  $\Delta V_{\text{DP}}$  is clearly stronger in the case of the PbS/ZnO/Gr, indicating a stronger shift in Fermi level and therefore a more significant charge transfer to Gr under same illumination. Figure 48 (d) shows the absolute change

in carrier density in Gr extracted from the shifts in  $V_{DP}$ , showing almost a  $2\times$  larger increments in Gr carrier density for PbS/ZnO/Gr (electron transfer) than for PbS/Gr (hole transfer) devices due to more efficient transfer of photocarriers under illumination and therefore improving the photoresponse. This higher transfer of photocarriers (Figure 48 (d)) contributes to the higher responsivity of the intermediate ZnO devices. In addition, difference in Gr carrier mobility and photocarrier lifetime in QDs may increase the photogain in the intermediate devices.

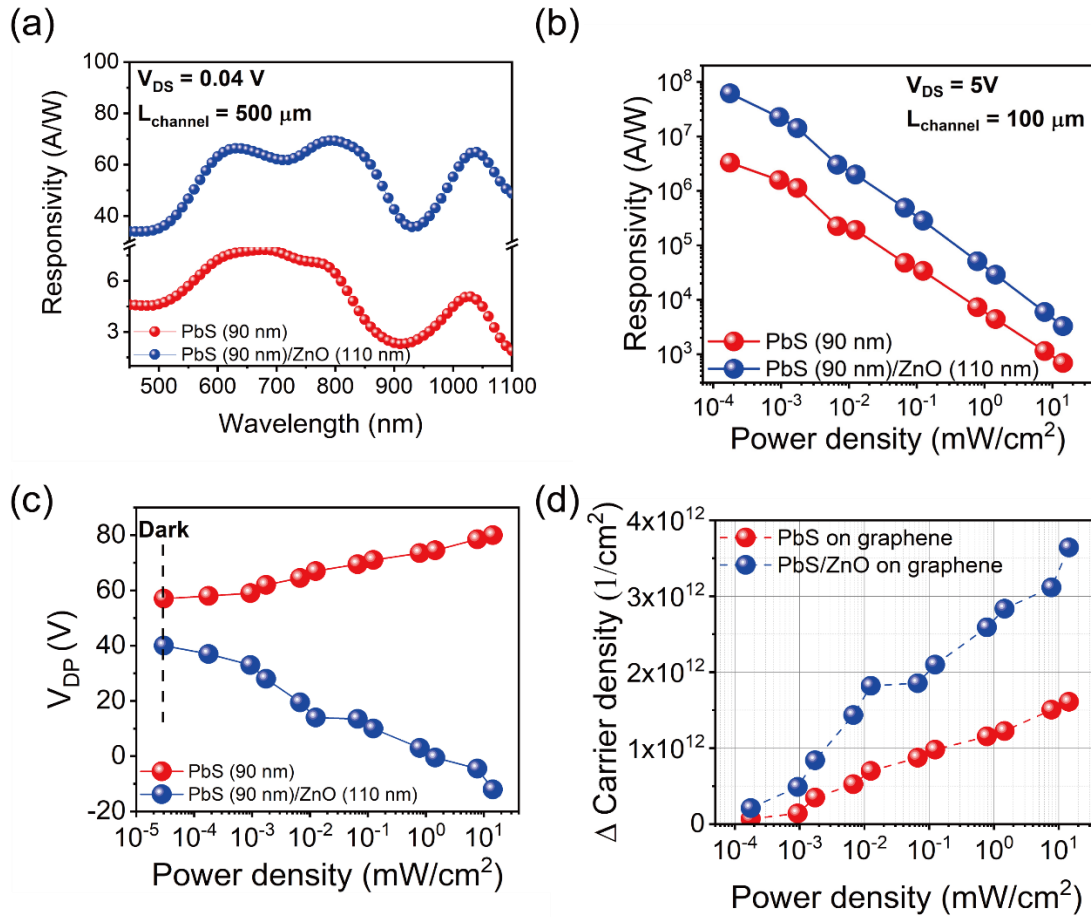


Figure 48 a) Responsivity as function of wavelength, showing a 10 $\times$  higher response for intercalated devices with ZnO. b) Responsivity as a function of power density, showing an increase in responsivity as the power decreases. The responsivity of the PbS/ZnO/Gr devices is  $\approx 10\times$  higher than PbS/Gr over the broad range of power density. c) Dirac-point voltage  $V_{DP}$  as a function of light intensity shows how  $V_{DP}$  increases (Fermi level decreases due to hole transfer) for PbS/Gr devices and how  $V_{DP}$  decreases (Fermi level increases due to electron transfer). The shift in  $V_{DP}$  is stronger for intercalated ZnO devices, indicating a larger shift in Fermi level. d) Absolute change in carrier density for PbS/Gr (hole transfer to Gr) and PbS/ZnO/Gr (electron transfer to Gr), showing the larger charge transfer for intermediate ZnO devices. The full set of I versus  $V_G$  and I–V curves for PbS/Gr and PbS/ZnO/Gr for different light intensities are shown in Figure 49.



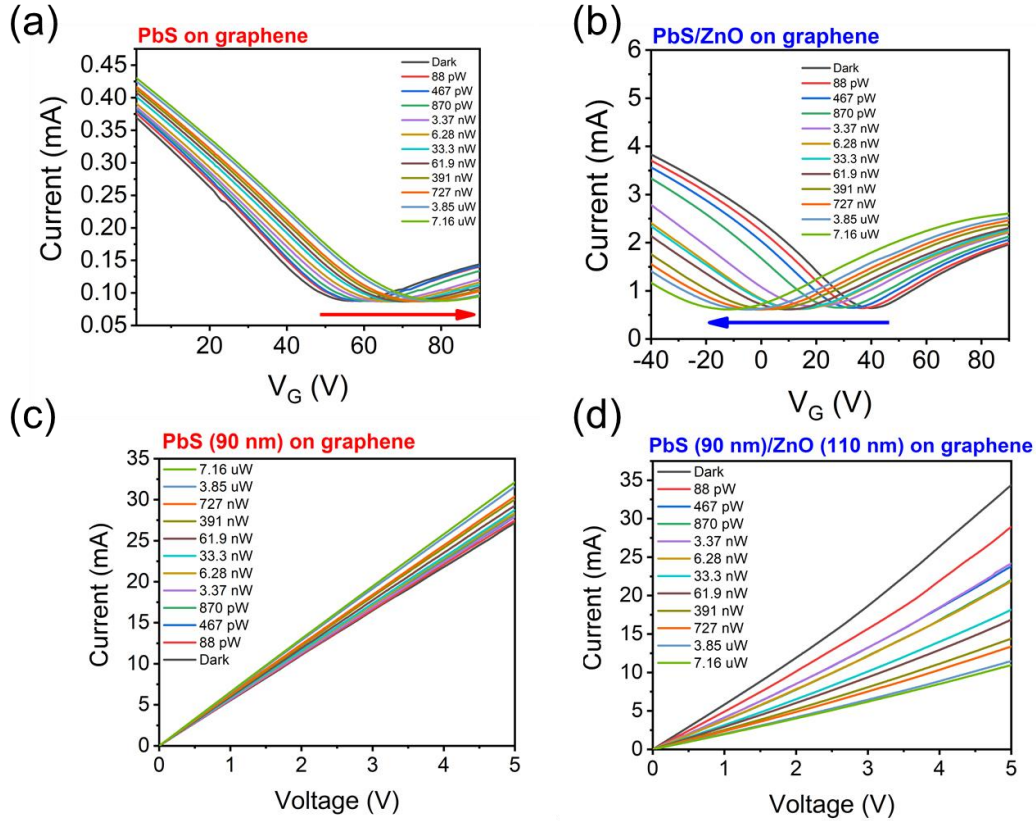


Figure 49. Full set of I vs  $V_G$  and I vs VDS plots for different light intensities for PbS/Gr and PbS/ZnO/Gr. This data is used to generate plots in Figure 48.(b and.c). (a) I vs  $V_G$  for different light intensity for PbS/Gr. The Dirac peak (VDP) increases to further positive values as light intensity increases. This confirms that as light intensity increases more holes are transferred to Gr. (b) I vs  $V_G$  for different light intensity for PbS/ZnO/Gr. The Dirac peak (VDP) is negatively shifted as light intensity increases, indicating more photoelectrons being transferred as more photons are absorbed. (c) I vs VDS for PbS/Gr showing increase in current as light intensity is increased without an  $V_G$  applied. (d) I vs VDS for PbS/ZnO/Gr showing how the current is further decreased as light intensity is increased without an  $V_G$  applied. This shows how more photoelectrons are transferred to Gr as intensity increases, reducing the conductivity of hole-majority carriers in Gr.

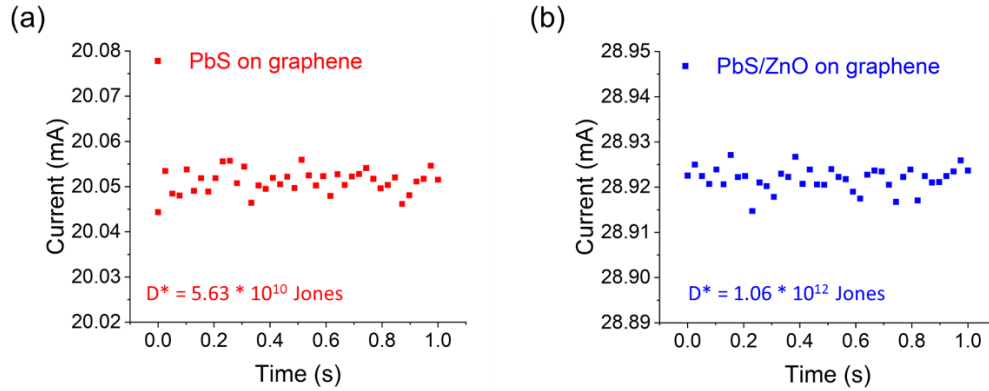


Figure 50. Dark current traces. The detectivity was calculated by  $D^* = \frac{\sqrt{\Delta f \cdot A}}{NEP}$ ,  $NEP = \frac{Noise_{rms}}{R}$ ,  $R =$  Responsivity,  $A = 0.001 \text{ cm}^2$ , and  $\Delta f = 20\text{Hz}$

Based on the stronger photoresponse and larger charge transfer in intermediate ZnO devices, we infer that a stronger driving force from PbS to ZnO than from PbS to Gr is the main factor for their superior performance. Similar to ZnO/PbS-QD solar cells, the ZnO/PbS p-n junction creates a strong charge separation junction, driving electrons toward ZnO. Due to the short  $\approx 30 \text{ nm}$  depletion layer at the ZnO/Gr interface estimated from Figure 3b, we infer that the electrons are then transferred from ZnO to Gr by diffusion. Once in Gr, charges are efficiently transported and collected. Hybrid PbS/MoS<sub>2</sub> devices have been reported in which photoelectrons are also transferred from PbS to MoS<sub>2</sub>, however, the mobility of MoS<sub>2</sub> is inferior to Gr, reaching a lower responsivity of  $10^6 \text{ AW}^{-1}$ , whereas our PbS/ZnO/Gr reaches  $\approx 10^8 \text{ AW}^{-1}$ .<sup>[74, 77]</sup>

shows the comparison of responsivity for PbS QD based photodetectors with different carrier transportation layer. Future work is required to measure the built-up potential, charge separation and charge transfer time scales at PbS/ZnO/Gr interfaces in order to better understand

charge dynamics and improve hybrid Gr/QD photodetectors.

### 5.3 Conclusion

In conclusion, we report a high-responsivity photodetector based on colloidal PbS QDs on a Gr monolayer with a ZnO intermediate layer that selectively allows the transfer of photogenerated electrons from PbS to Gr, as opposed to the transfer of photoholes in PbS/Gr devices. Using gate-sweep measurements it is possible to monitor Fermi level and charge transfer to Gr under illumination, showing larger charge transfer in intermediate ZnO devices. The devices with intermediate ZnO have a stronger photoresponse than the direct PbS/Gr devices, which we presume is due to a stronger driving force from PbS to ZnO. This work also demonstrates how nanomaterials such as nanoparticles, quantum dots and Gr can be integrated into novel architectures, maximizing and complementing their optical and electrical properties for high performing optoelectronic devices. The use of ZnO opens the route for new optoelectronic devices based on hybrid Gr and QD devices that require both hole and electron transfer, such as photovoltaic cells and light emitting diodes.

Table 7 Comparison of responsivity for PbS based photodetectors.

Carrier transport material	Structure	Responsivity [A/W]	Laser power	Ref
Gr	PbS/ZnO/Gr	$6.16 \times 10^7$	0.17 mW/cm <sup>2</sup> (635 nm)	This work
	PbS-pyridine on Gr	$\sim 10^7$	4.5 nW/cm <sup>2</sup> (895 nm)	[34]
	PbS on Gr	$5 \times 10^7$	<10 fW (532 nm)	[13]
	Intercalated Gr/PbS QD system	$5.94 \times 10^7$	$\sim 10^{-5}$ mW/cm <sup>2</sup> (532 nm)	[81]
	1 $\mu$ m thick intercalated Gr/PbS QD system	$\sim 10^7$	$\sim 10^{-5}$ mW/cm <sup>2</sup> (850 nm)	[71]
	Gr/PbS QDs/Gr	$> 10$	430 $\mu$ W/cm <sup>2</sup> (650 nm)	[78]
MoS <sub>2</sub>	PbS(EDT)/PbS(TBAI)/MoS <sub>2</sub>	$5.4 \times 10^4$	20 pW (850 nm)	[108]
	PbS/MoS <sub>2</sub>	$6 \times 10^5$	3 $\mu$ W/cm <sup>2</sup> (635 nm)	[77]
SnS <sub>2</sub>	SnS <sub>2</sub> nanosheet/PbS CQDs	$> 10^6$	0.23 $\mu$ W/cm <sup>2</sup> (970 nm)	[109]
CdS <sub>x</sub> Se <sub>1-x</sub>	CdS <sub>x</sub> Se <sub>1-x</sub> nanosheet/PbS QDs	$1.45 \times 10^3$	$\sim 0.01$ mW/cm <sup>2</sup> (405 nm)	[110]
InGaZnO	PbS QD/IGZO hybrid	$> 10^6$	5.97 pW (1000 nm)	[111]
PbS	PbS(TBAI)/PbS(EDT)	$\sim 0.25$	10.6 $\mu$ W/cm <sup>2</sup> (580 nm)	[112]

## 5.4 Experimental Section

**PbS-QD Synthesis:** Lead sulfide capped with oleic acid with emission at  $\lambda \approx 1100$  nm was purchased from Can GmbH Hamburg (Germany).

**ZnO Nanoparticles Synthesis:** The synthesis of ZnO followed the method described in literature using zinc acetate as precursor with a KOH solution.<sup>[113]</sup> In brief, a solution of KOH was added to a zinc acetate solution in methanol. 3.0 g of zinc acetate dihydrate was dissolved in 125 mL of methanol at 60 °C under stirring at 300 rpm for 1 h. Potassium hydroxide (1.48 g) was dissolved in 65 mL of methanol with 400 rpm stirring for 1 h. The potassium hydroxide solution was slowly added to the zinc acetate solution and the solution was kept stirring at 60 °C for 5 h. ZnO nanoparticles were extracted by centrifugation and washed in by methanol. Finally, they were dispersed in 20 mL of chloroform and filtered with a 0.45  $\mu\text{m}$  filter.

**Gr Transfer:** Single-layer Gr was purchased from Graphenea (Spain). The product consists of poly-methyl methacrylate (PMMA) film on Gr on copper foil. Copper was removed by wet etching using an aqueous solution of ammonium persulfate (APS). Once copper foil was completely etched, PMMA/Gr film was rinsed in DI water for 2 h. Finally, the layer was transferred onto an Au patterned electrode SiO<sub>2</sub>/Si substrate and then dried for 2 h at room temperature, followed by the removal of the PMMA coating using acetone, isopropyl alcohol, and DI water.<sup>[114]</sup>

**Materials Characterization:** The structural information of Gr was carefully analyzed by employing Raman spectroscopy (Renishaw). The optical band gap of ZnO and absorption spectrum of PbS QDs were investigated by the UV-vis spectroscopy (UH4150, Hitachi). Moreover,

crystallographic characterization of ZnO was conducted by using X-ray diffraction (Smartlab, Rigaku).

Device Fabrication: PbS QDs film was prepared by spin coat method. 100  $\mu$ L of the solution was deposited on the substrate by the spin coater at 2500 rpm for 10 s, then a ligand exchange was performed by flooding the surface with 0.03 M tetrabutylammonium iodide (TBAI) in methanol for 30 s before spinning dry at 2500 rpm. The thickness of five spin-coated layers of PbS QDs was 150 nm as shown in Figure 40 (a). ZnO film was prepared by spin coat method. 100  $\mu$ L of the solution was deposited on the substrate by the spin coater at 2500 rpm for 10 s and dried at 200  $^{\circ}$ C for 10 min. This process was repeated according to the number of ZnO layer. The thickness of five spin-coating of ZnO was 180 nm, as shown in Figure 40 (b). Optoelectronic Characterization: The light intensity was measured with a standard silicon photodiode power sensor (S120VC, Thorlabs) at the same position of the samples. A pinhole of  $1 \times 1 \text{ mm}^2$  was used to illuminate only the active area. Current-voltage data were measured using a Keithley 2400 source meter under a 635 nm laser diode (CPS635, Thorlabs). In order to achieve different light intensity, absorptive neutral density filters (NE503A, NE510A, NE520A, NE530A, Thorlabs) were employed.

Chapter 5, in full, is a reprint of the material as it appears in “Selectively Electron-transport from PbS quantum dots to single layer graphene with ZnO intermediate layer with Ultrahigh Responsivity”. Seungbae Ahn, Miguel Angel Moreno Gonzalez, Wenjun Chen, Malcolm Lockett, Jiaying Wang, Oscar Vazquez-Mena, *Advanced Electronic Materials* 2020, 6 (6), 2000014. The dissertation author was the primary investigator and author of this paper.

### **High resolution patterning of PbS quantum dots/graphene photodetectors with high responsivity via photolithography with top graphene layer to protect surface ligands**

Photodetectors based on colloidal quantum dots (CQDs) and single layer graphene (SLG) have shown high responsivity coming from the synergy of strong light absorption from CQDs and high mobility from SLG. However, it is still challenging to achieve high-density and small-foot print devices on a chip to meet the demand for their integration into electronic devices. Even though there are numerous approaches to pattern the chemically fragile CQD films, usually they require non-conventional approaches such as stamping and surface modification that may be noncompatible with the semiconductor processing. In this study, we show that conventional lithography and dry etching can be used to pattern QD active films by employing a graphene monolayer passivation/protective layer that protects the surface ligands of CQDs. This protective layer avoids damage induced by lithography processing solvents that deteriorate the carrier mobility of CQDs and therefore photoresponse. Herein we report patterning of CQDs using conventional UV photolithography, achieving reproducible five-micron length PbS CQDs/SLG photodetector with a responsivity of 108 AW-1. We have also fabricated thirty-six PbS CQDs/SLG photodetectors on a single chip to establish micron size photodetector. This process offers an approach to pattern QDs with conventional UV lithography and dry etching semiconductor technology to facilitate its integration into current semiconductor commercial technology.

## 6.1 Introduction

Colloidal quantum dots (CQDs) are promising nanomaterials for light emission and detection applications because of their unique characteristics such as tunable band gaps that cover ultraviolet (UV), visible (Vis), and infrared (IR) bands ( $\lambda$ : 300 nm – 8  $\mu$ m) depending on their composition (e.g. ZnO, CdS, PbS, GaAs, and HgTe) and size.<sup>[115]</sup> Optical properties such as high absorption and emission are very attractive for various applications such as photovoltaics, photodetectors, and light-emitting diodes.<sup>[73, 116]</sup> Whereas inorganic semiconductors offer high-speed performance, Gr/QD system offer ultrathin and flexible active films with high responsivity that are important in biomedical applications. Even though there have been various studies to improve the efficiency and stability of CQD, there are still limitations regarding the patterning techniques compatible with conventional semiconductor processing to facilitate their integration into electronic devices.<sup>[117]</sup> The ligands required to stabilize films and facilitate charge transport are chemically fragile with respect to chemicals involved in conventional lithography processes such as photoresists, developers, and resist removers. Proposed methods allowing CQDs patterning include jet printing, dip-pen nanolithography, contact-printing, light-driven ligand crosslinking, assisted patterning, and direct extreme ultraviolet and electron-beam lithography.<sup>[118, 119]</sup> However, there is still a challenging trade-off between processing complexity, resolution, and cost. For example, direct patterning methods such as jet printing, dip-pen nanolithography, and contact printing have been extensively developed but they still fall short of current industrial demands in terms of the resolution, throughput rate, and uniformity. Light-driven ligand crosslinking patterning can achieve high resolution, but it requires specific light-sensitive ligands. Conventional UV photolithography has strong limitations



since the photoresist and developer react with the short-chain ligands on CQDs, causing performance degradation.

In this study, we develop an effective patterning technique that uses conventional UV photolithography and dry etching of CQDs by means of a poly(methyl methacrylate) (PMMA)/single layer graphene (SLG) passivation layer (PGPL) to prevent the damage induced on the CQD surface ligands by photolithography chemicals. This is extremely relevant since damaging of QD surface ligands can result in severe degradation of photocarrier transfer in the QD film and therefore on photodetection performance. There have been numerous reports showing the use of SLG as an impermeable layer to various liquids and gases, allowing the protection of chemically fragile structures.<sup>[119]</sup> Based on this report, we use SLG to protect the QDs ligands during the patterning process to successfully pattern PbS QD films reaching minimum features of 10  $\mu\text{m}$  by 10  $\mu\text{m}$  squares and line arrays with 3  $\mu\text{m}$  pitch. More importantly, we demonstrate the fabrication PbS QDs/SLG photodetectors with different SLG channel lengths (5, 10, 20, 50, 100, 200, and 500  $\mu\text{m}$ ) showing higher responsivity and avoiding performance degradation as compared to devices fabricated without the protective layer. Since the photogain increases as the device length decreases, we reach the high responsivity of  $10^8 \text{ AW}^{-1}$  with the smallest channel length of 5  $\mu\text{m}$ . Also, thirty-six PbS QDs on SLG photodetectors have been fabricated to test the reliability after the patterning process.

## 6.2 Results and Discussion

Figure 51 shows the process flow for patterning of CQDs on SLG with a PGPL via a conventional photolithography method to obtain CQD based photodetectors. The substrate has

predefined Au electrodes prepared by lithography and lift-off with a channel length of 5, 10, 20, 50, 100, 200, and 500  $\mu\text{m}$ , and with fixed width of 500  $\mu\text{m}$  on top of  $\text{SiO}_2$  as shown in Figure 51 (a). Then SLG layer as conductive channel was transferred on the substrate via PMMA supported wet transfer (Figure 51 (b)). The patterning of SLG using AZ1518 photoresist and oxygen plasma etching is described in the experimental section (Figure 51 (c)). SLG channels with fixed width of 100  $\mu\text{m}$  and varying channel lengths adapted to the 50–500  $\mu\text{m}$  long predefined electrodes were patterned (Figure 52 (a)). The patterned SLG substrate was coated by PbS CQDs via spin coating (Figure 51 (d)). The deposition of PbS CQDs and ligand exchange are described in the experimental section. After that, PGPL was transferred on top of the CQDs film following conventional PMMA/Gr transfer in aqueous solution (Figure 51 (e)). During PGPL transfer, the device is immersed in DI water, however, previous reports show that this process does not induce significant degradation of the light absorption of the PbS CQDs film.<sup>[18, 70, 71]</sup> AZ1518 UV photoresist was spin coated on top of the PGPL as shown in Figure 51 (f). PGPL prevents the photoresist from permeating into PbS CQDs due to low permeability of PMMA and SLG. The photoresist was patterned and developed using conventional UV photolithography (Figure 51 (g)). The etching process was done in two steps. First, the top PGPL was etched by the oxygen plasma. After that, the PbS CQDs were etched by a mixture of  $\text{H}_2/\text{CH}_4/\text{Ar}$ .<sup>[120]</sup> After etching process, PGPL layer was removed by immersing in acetone and cleaned by IPA and DI water. The conditions for etching SLG and PbS QDs and cleaning process are described in experimental section. The gas mixture of  $\text{CH}_4/\text{H}_2$  plasma dry etching commonly used for III-V and II-VI semiconducting materials. In the process,  $\text{CH}_4$  gas forms volatile metal organic species with lead, which is easily taken off from the surface by Ar ion, and

H<sub>2</sub> forms volatile hydride species with sulfur. Optical pictures of the final patterned PbS CQDs/SLG photodetectors are shown in Figure 52 (b). Our final devices have a bottom SLG that serve as charge collector, the PbS CQDs film that serves as light absorber, and the top PGPL that protects the QD during photolithography but also contributes to charge collection in this case. Figure 51 (i) – (k) show the scanning electron microscope (SEM) images of examples of different patterns of CQD films that illustrate the capabilities of our method to pattern CQD films. Figure 51 (i) shows a 2D array of 10 μm x 10 μm squares, Figure 51 (j) shows a line grid of 3 μm wide CQD films separated by 3 μm, and Figure 51 (k) shows the “UCSD Nanoengineering” legend. These patterned array of PbS CQDs shows no significant residue in regions where etching process occurred. The inset in Figure 51 (k) shows images of the Pb signal from EDX.

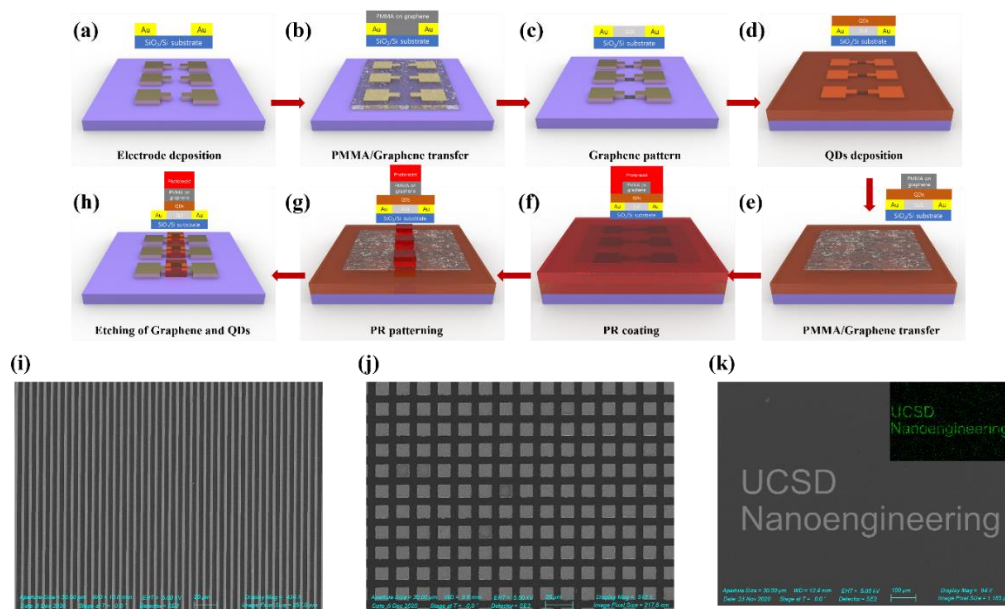


Figure 51 Schematic diagram of the patterning process for PbS CQDs using PGPL. (a) Au (100 nm)/Cr (10 nm) electrodes were deposited using e-beam evaporator with different channel lengths (5, 10, 20, 50, 100, 200, and 500  $\mu\text{m}$ ). (b) PMMA/SLG layer was transferred on the prepatterned-electrodes substrate via PMMA supported wet transfer method. (c) SLG was patterned by photolithography method with the same channel width (100  $\mu\text{m}$ ). (d) PbS CQDs were deposited by spin-coating method with TBAI ligand exchange. (e) PGPL was transferred on PbS CQDs on patterned SLG substrate. (f) Photoresist was coated on the substrate. (g) The patterning was executed by the conventional UV photolithography process. (h) Exposed PGPL and PbS CQDs were removed by oxygen plasma and  $\text{CH}_4/\text{H}_2/\text{Ar}$  plasma, respectively. After that, PGPL layer was removed by acetone, IPA, and DI water cleaning process (i) SEM image of 10  $\mu\text{m}$  x 10  $\mu\text{m}$  square array. (j) SEM image of 3  $\mu\text{m}$  line array. (k) SEM image of “UCSD Nanoengineering legend” words. Insets: Pb EDX signal from SEM.

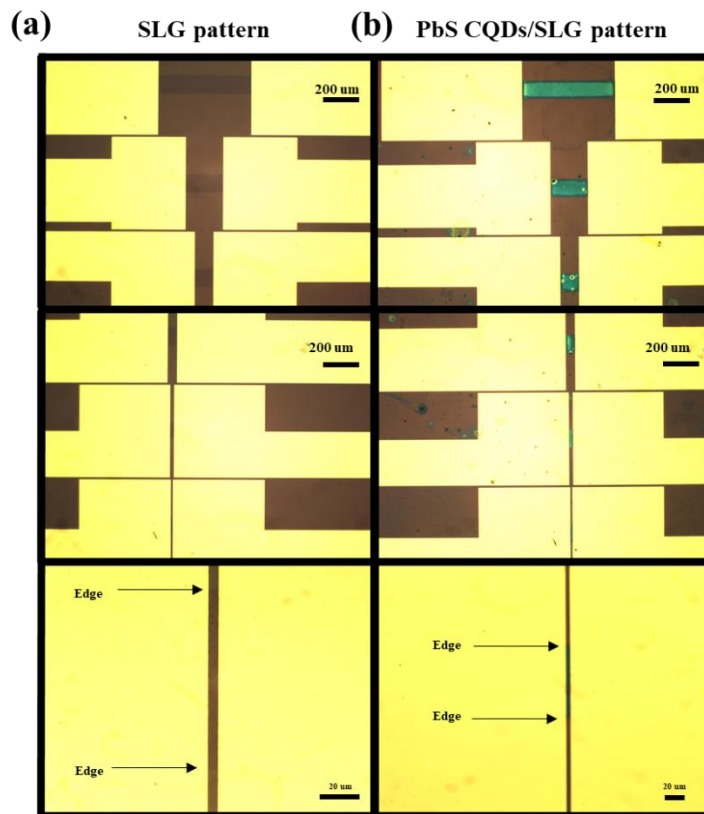


Figure 52 a) Optical images of patterned SLG. The length of SLG is 500, 200, and 100  $\mu\text{m}$  in first row from top to bottom, respectively, and 50, 20, and 10  $\mu\text{m}$  in second row, from top to bottom, respectively, and 5  $\mu\text{m}$  in third row and the width of all SLG channel is 100  $\mu\text{m}$ . b) Optical images of patterned PbS CQDs on patterned SLG.

In order to understand the possible effects of the photolithography process on the performance and chemistry of the CQDs, we investigated the UV-Vis spectroscopy and Fourier Transform Infra-Red spectroscopy (FTIR) of the CQDs as we performed lithography patterning with and without the protective layer. It is observed that first absorption peak of pristine PbS CQDs is 930 nm. However, after the patterning without the PGPL, there is a blue shift of  $\sim 35$  nm and a reduction in the first absorption peak as shown in Figure 53 (a). In contrast, when using the PGPL,

the blue shift is limited to  $\sim 6$  nm (Figure 53 (b) and the first exciton absorption peak is not reduced. We suggest that for the samples without PGPL, the spectrum modification is due to the formation of minibands in PbS QDs induced by electron coupling between adjacent QDs when the ligands are modified by the organic developer or photoresist.<sup>[121]</sup> FTIR is shown in Figure 53 (c), providing further insight on the surface chemistry of the CQDs during the lithography process and on the impact of the PGPL. FTIR spectra of the pristine (black trace) and patterned PbS CQDs with PGPL (red trace) indicate asymmetric C-H ( $2925$  and  $2956$   $\text{cm}^{-1}$ ) and symmetric C-H ( $2853$   $\text{cm}^{-1}$ ) vibrations, but no vibration modes between  $1400$  and  $1600$   $\text{cm}^{-1}$ .<sup>[122]</sup> On the other hand, FTIR spectrum of patterned PbS CQDs without PGPL shows weaker stretching modes around  $2900$   $\text{cm}^{-1}$ , with additional CH bending modes ( $1461$   $\text{cm}^{-1}$ ) not present in pristine and PGPL samples. The FTIR and UV-VIs spectra of the samples without PGPL indicate a modification of the ligands probably due to resist and developer processing. Therefore, we infer that PGPL plays an important role protecting the chemistry of the CQD during the lithographic process.

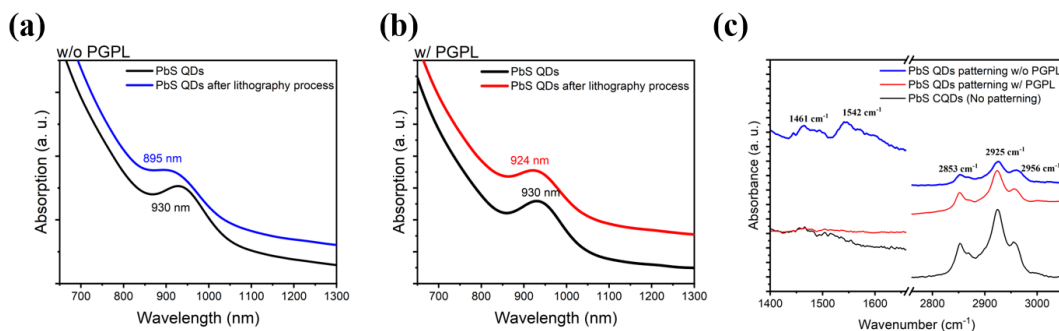


Figure 53 (a) UV-vis absorption spectra of PbS CQDs without PGPL, showing the shift of a resonance peak from 930 nm to 895 nm. (b) UV-vis absorption spectra of PbS CQDs with PGPL, representing the shift of a resonance peak from 930 nm to 924 nm. (c) FTIR spectra of photoresist, pristine PbS CQDs, and the patterned PbS CQDs with and without PGPL.

The impact of the PGPL on the photoresponse of hybrid SLG/CQDs photoconductive detectors was tested on devices with graphene channels of length of 100  $\mu\text{m}$  and width of 100  $\mu\text{m}$  (underneath SLG, Figure 51 (c)) under  $\lambda = 635 \text{ nm}$  illumination. The principle of operation of the devices is shown in Figure 54. Light is absorbed by QDs generating photocarriers, followed by charge separation. In the specific case of Gr and PbS-QDs, due to band alignment and interface built-in potential, electrons stay in the QDs while holes are transferred to graphene. The transferred holes change the graphene (p-type) conductivity while the electrons generate a photogating effect. Non-patterned PbS CQDs on SLG (reference devices), and patterned PbS CQDs on SLG with and without PGPL were tested. The thickness of the CQD film was  $\sim 150 \text{ nm}$  obtained by spin coating 5 CQD layers. More details about the sample preparation are given in the Experimental section. Figure 55 (a) shows the time-modulated response for the three devices. All cases show similar time modulated response with good time stability. Variations in the dark current base level can be due to variations in the resistance of SLG (Figure 56) probably associated to residues after PMMA/wet and SLG patterning. The reference performance is the device without CQD patterning, producing a photocurrent of  $50 \mu\text{A}$ . If the QDs are patterned without the PGPL, the photocurrent drops significantly to  $\sim 18 \mu\text{A}$  (blue trace). This is expected from the disorder and contamination induced by the photoresist during the patterning process. On the other hand, the patterned device with PGPL results in a higher photocurrent of  $\sim 63 \mu\text{A}$ . The dark current increases due the top graphene of the PGPL which contributes to the conductivity of the device. Furthermore, the top SLG of the PGPL increases the responsivity as it helps to collect photocarriers and increase the photocurrent as shown previously.<sup>[18]</sup> Photo-excited carriers on the surface of PbS CQDs can be efficiently collected by the

top graphene channel of the PGPL, instead of recombining while crossing the entire film thickness to reach the bottom SLG. However, it is important to remark that the critical role of the PGPL is to protect the ligands. Without the PGPL, lithography chemicals harm the ligands permanently, and even adding a PGPL after the lithography does not recover the photoresponse. This is shown in Figure 57, showing that without the PGPL, the lithography induces damages and poor performance that cannot be recovered adding the PGPL after the lithography. Therefore, the critical role of the PGPL is to protect the ligands during lithography. The enhanced collection with the top graphene of the PGPL is an added, but not essential, benefit. Regarding the time response, the devices show a long-time delay ( $> 1$  s) response is due to trap states in the QDs and at the QD/Gr interface as has been reported previously for hybrid Gr/QD systems.<sup>[13, 34, 94]</sup> Passivating layers can be used to reduce the response delay.<sup>[35, 74]</sup> Figure 58 shows 60 seconds time traces showing the stability of the photoresponse. Figure 55 (b) shows the spectral response, using Hg-Xe lamp light source and a monochromator, showing the similar trend of superior performance for devices with PGPL in the entire  $\lambda = 400 - 1000$  nm range. The photoresponsivity as a function of power is shown in Figure 55 (c), showing the expected trend in hybrid SLG/CQDs photodetectors of higher responsivity for lower power, which is due to higher recombination at higher light intensity. Through the wide range of intensities, the patterned devices with PGPL devices show superior performance. Figure 55 (d) shows the photoresponsivity for the shortest channel length  $5 \mu\text{m}$  with  $100 \mu\text{m}$  width. The  $5 \mu\text{m}$  length PbS QDs on SLG photodetector shows a record high responsivity of  $10^8 \text{ AW}^{-1}$ . This is expected as the photogain of the devices is proportional to the ratio of the lifetime  $\tau$  of the photo-induced carrier over carrier transit time  $\tau_l = \frac{L^2}{\mu V_{DS}}$ , where  $L$  is the channel length,  $\mu$  is the carrier



mobility, and  $V_{DS}$  is the drain-source voltage. As expected, the shorter 5  $\mu\text{m}$  long channel results in a higher photogain and therefore photoresponsivity.

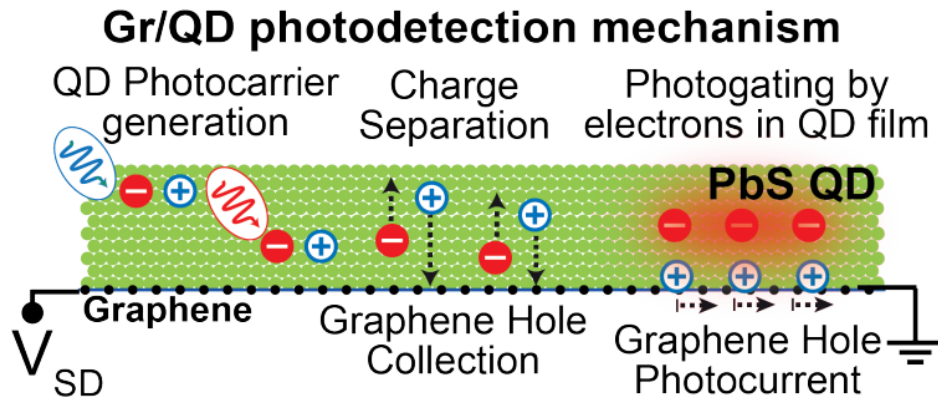


Figure 54 Light is absorbed by QDs generating photocarriers, followed by charge separation. In the specific case of Gr and PbS-QDs, due to band alignment and interface built-in potential, electrons stay in the QDs while holes are transferred to graphene. The transferred holes change the graphene (p-type) conductivity while the electrons generate a photogating effect.

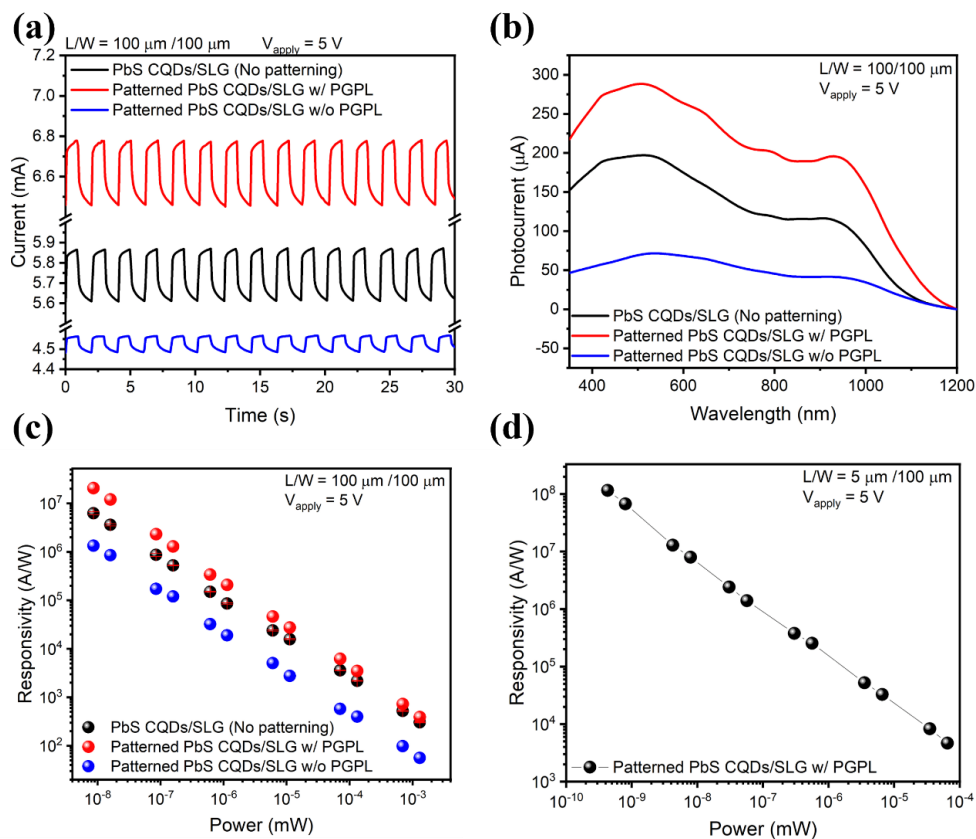


Figure 55 (a) Time response for on/off light switching for pristine PbS CQDs/patterned SLG, patterned PbS CQDs/SLG with PGPL, and without PGPL ( $V_{\text{bias}} = 5 \text{ V}$ ,  $\lambda = 635 \text{ nm}$ ,  $17 \text{ mW/cm}^2$ ). (b) Responsivity as function of wavelength, showing the highest response for patterned PbS CQDs/SLG with PGPL (Hg-Xe lamp with monochromator). (c) Responsivity versus power, showing an increase in responsivity as the power decreases ( $\lambda = 635 \text{ nm}$ ). (d) Responsivity as a function of power ( $\lambda = 635 \text{ nm}$ ), showing that the shortest channel length of  $5 \mu\text{m}$  reaches a responsivity of  $10^8 \text{ A/W}$ .

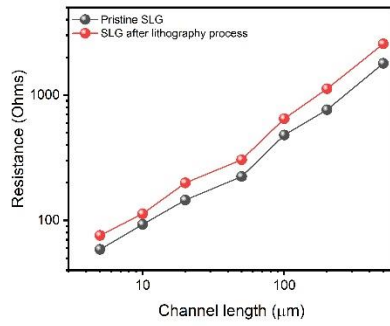


Figure 56 The resistance of various lengths SLG before and after lithography process.

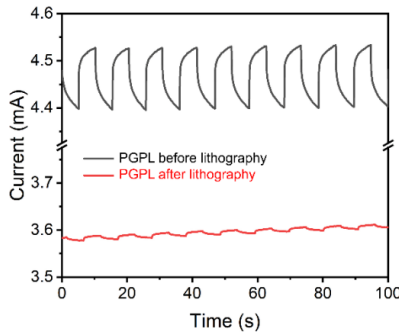


Figure 57 Photoresponse: PGPL before and after lithography. These results clearly show the use of lithography without the PGPL result in significant degradation of the photoresponse. Adding the PGPL with the top graphene layer after the lithography does not show any significant enhancement since the QD ligands are already damaged.

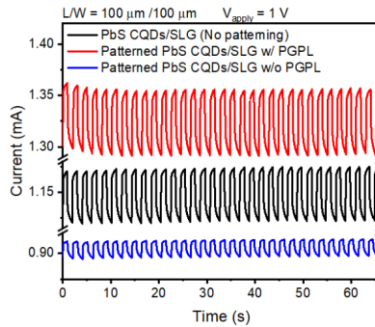


Figure 58 The 60-seconds time traces show the stability of the photoresponse.

Our patterning technique allows to fabricate an array of thirty-six PbS CQDs/SLG photodetectors with dimensions of 100  $\mu\text{m}$  by 100  $\mu\text{m}$ . Figure 59 (a) shows the optical images of the electrodes with patterned SLG and Figure 59 (b) shows the same chip after deposition and patterning of PbS CQDs with the PGPL protective layer. Patterning capabilities can be extremely important for hybrid QD/Gr image sensors arrays on CMOS platforms as has been reported elsewhere with pixel sizes of 3  $\mu\text{m}$  based only on Gr patterning achieving detectivities of  $10^{10}$ – $10^8$  Jones.<sup>[80]</sup> Adding the patterning of QDs can improve pixel resolution and reduce the noise, potentially getting to detectivities of  $10^{12}$  Jones achieved for individual detectors. We measured photoresponse on randomly selected six photodetectors on the chip. Figure 59 (c) shows the responsivity versus incident power and Figure 4 (d) shows the spectral response, illustrating a good uniformity in device characteristics. The detectivity ( $D^*$ ) is also investigated as shown in Figure 59 (e), showing that the devices can reach  $D^* \sim 10^{12}$  Jones at low powers ( $10^{-8}$  mW) at 40 Hz. The details on the noise measurements and detectivity calculations are shown in the Figure 60. The responsivity and detectivity of the devices improve significantly as the light intensity decreases. For large intensities, there is a significantly increase in charge recombination, reducing the number of photocarriers transferred from the QDs to Gr. This behavior has been observed in previous reports in QD/Gr photodetectors as well for QD only based photodetectors.<sup>[13, 34, 35, 73, 123]</sup> As described elsewhere, the amount of charges transferred from QDs to Gr has a sub-linear dependence on the light intensity, resulting in an overall decrease in responsivity as light intensity increases.<sup>[34, 73]</sup>

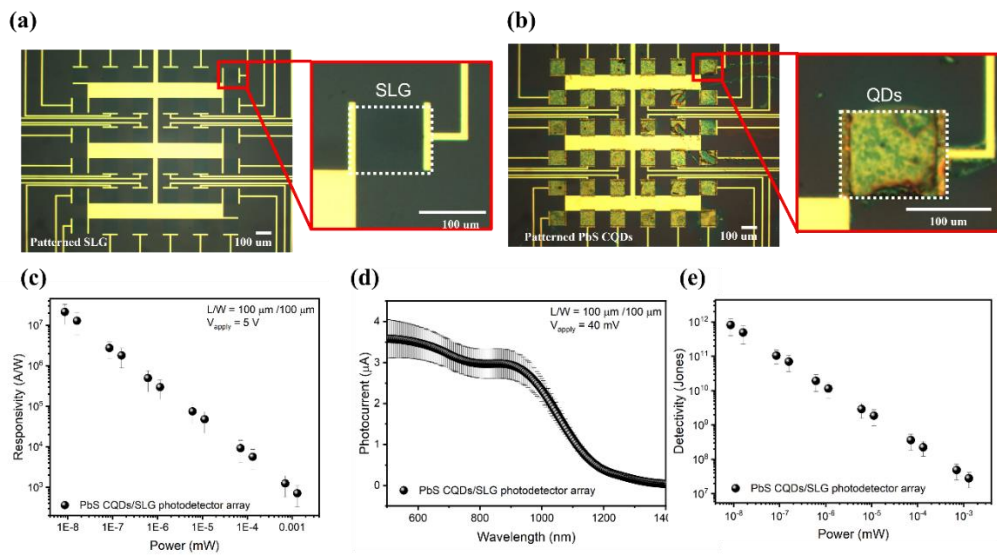


Figure 59 (a) Optical images of 100  $\mu\text{m}$  by 100  $\mu\text{m}$  patterned SLG. (b) Same devices after coating PbS CQDs/SLG, forming a photodetector array. (c) Responsivity as a function of power for PbS CQDs/SLG photodetector array, showing the small variations in the performance of the photodetectors in the array. (d) Photocurrent versus wavelength for the array, showing the reliable photocurrent response depending on the wavelength. (e) Detectivities versus power incident for PbS CQDs/SLG photodetector array at 40 Hz.

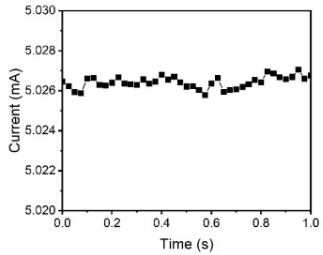
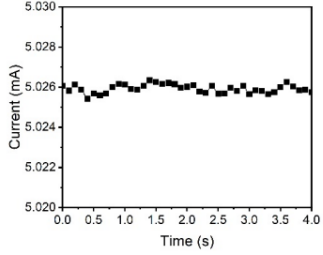
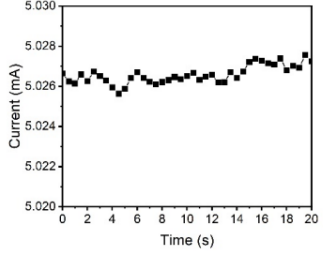
Device dimensions: Device Area ( $A_d$ ): $(100\mu\text{m})^2=0.0001 \text{ cm}^2$	
<p>Dark current trace at <math>\Delta f=40 \text{ Hz}</math>:</p> 	<p>Responsivity at 40 Hz: <math>7.32 \times 10^6 \text{ A/W}</math></p> <p>Current RMS noise at 40 Hz: 292 nA</p> <p><math>\text{NEP} = \text{Noise}_{\text{rms}} / \text{Responsivity} = 3.99 \times 10^{-14} \text{ W}</math></p> <p>Detectivity: <math>D^* = \frac{\sqrt{\Delta f A_d}}{\text{NEP}} = 1.59 \times 10^{12} \text{ Jones}</math></p>
<p>Dark current trace at <math>\Delta f=10 \text{ Hz}</math>:</p> 	<p>Responsivity at 10 Hz: <math>9.34 \times 10^6 \text{ A/W}</math></p> <p>Current RMS noise at 20 Hz: 210 nA</p> <p><math>\text{NEP} = \text{Noise}_{\text{rms}} / \text{Responsivity} = 2.25 \times 10^{-14} \text{ W}</math></p> <p>Detectivity: <math>D^* = \frac{\sqrt{\Delta f A_d}}{\text{NEP}} = 1.41 \times 10^{12} \text{ Jones}</math></p>
<p>Dark current trace at <math>\Delta f=2 \text{ Hz}</math>:</p> 	<p>Responsivity at 2 Hz: <math>1.28 \times 10^7 \text{ A/W}</math></p> <p>Current RMS noise at 20 Hz: 441 nA</p> <p><math>\text{NEP} = \text{Noise}_{\text{rms}} / \text{Responsivity} = 3.45 \times 10^{-14} \text{ W}</math></p> <p>Detectivity: <math>D^* = \frac{\sqrt{\Delta f A_d}}{\text{NEP}} = 0.41 \times 10^{12} \text{ Jones}</math></p>

Figure 60 Calculation of detectivity at incident light power of  $1.6 \times 10^{-8} \text{ mW}$  at 40, 10 and 2 Hz.

### 6.3 Conclusion

In conclusion, we report the high-resolution patterning of high-responsivity photodetectors based on PbS CQDs/SLG via conventional UV photolithography with PGPL as an impermeable layer that prevents the damage of the surface ligands of the PbS CQDs during the UV photolithography and dry etching process. The resolution of PbS CQDs patterning can reach a few microns. The photoresponse for 5  $\mu\text{m}$  length and 100  $\mu\text{m}$  width PbS CQDs/SLG photodetector has a high responsivity ( $>10^8 \text{ AW}^{-1}$ ) and detectivity ( $\sim 10^{12}$  Jones). Moreover, the array for PbS CQDs/SLG photodetectors shows reliable photoresponse for high responsivity and spectral response. The results provide easy and promising patterning process for CQDs based devices such as photodetectors.

### 6.4 Experimental section

PbS QDs synthesis: Lead oxide (0.94 g) was dissolved in 1-octadecene (25 ml) with an oleic acid (4 ml) in the three neck flask. Next, the flask was degassed under vacuum at 90°C for two hours to be dissolved. When the solution becomes clear, bis(trimethylsilyl) sulfide (420  $\mu\text{l}$ ) dissolved in 1-octadecene (12.8 ml) was injected in the solution. After that, we allowed the reaction to be done for 30 seconds and cooled down by putting the flask in ice water. The solution was centrifugated, followed by cleaning with toluene and acetone three times, and then dissolved in toluene (30mg/ml) after filtration with a 250 nm pore size filter.<sup>[12]</sup>

Graphene transfer: We purchased CVD-SLG on Cu coated with PMMA from Graphenea (Spain). The backside of Cu was etched by oxygen plasma. It was transferred to the substrate by wet

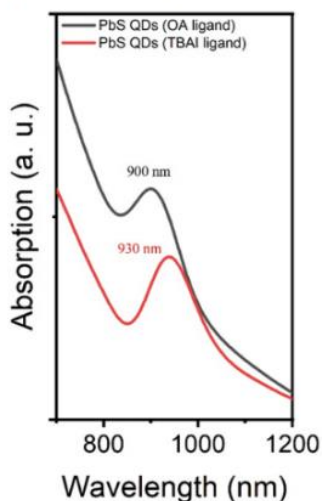
method. Cu was removed by ammonium persulfate solution. After Cu was completely etched, PMMA/SLG layer was transferred to DI water to remove etching residues. Then, PMMA/SLG layer was transferred onto an Au patterned electrode SiO<sub>2</sub>/Si substrate and dried for two hours at room temperature. Finally, PMMA layer was removed by acetone and cleaned with isopropyl alcohol and DI water.

Device fabrication: 1) Graphene patterning: PMMA/SLG layer was patterned by (i) spin coating of a ~2 μm thick AZ1518 photoresist (3000 rpm, 45 s), (ii) irradiation of UV and (iii) developing process using AZ300 MIF solution. Then dry etching was used to pattern the SLG conductive channel by oxygen plasma dry etching (100 mTorr, 75W RIE, and 50 sccm of O<sub>2</sub> for 5 min) and PMMA was removed by acetone, iso-propyl alcohol (IPA), and DI water shown in Figure 51 (c). 2) PbS CQDs coating: PbS QDs films were prepared by a spin coat method. 100 μl of PbS QDs in toluene was deposited on the substrate with 2,500 rpm for 10 sec. 30 mM tetrabutylammonium iodide (TBAI) solution in methanol was added for a ligand exchange by incubation for 30 sec and followed by cleaning in methanol. The effect of the ligand exchange from OA to TBAI is shown in Figure 61, showing the poor performance in photoresponse with OA and the drastic improved response after exchanging to TBAI. The ligand exchange also induces a red-shift of  $\Delta\lambda=30$  nm in the absorption exciton peak. The active areas of the photodetectors are defined by the area between electrodes, which have a width of 500 μm and a variety of channel lengths (5, 10, 20, 50, 100, 200, and 500 μm). 3) PbS CQDs etching: Dry etching was used to pattern the PbS CQDs film by the mixture of H<sub>2</sub>, CH<sub>4</sub>, and Ar gases. The conditions for etching 150 nm PbS CQDs are 35 mTorr pressure, 400W ICP, 150W RIE, 70 sccm of H<sub>2</sub> gas, 10 sccm of CH<sub>4</sub> gas, and 10 sccm



of Ar gas for 45 sec.

UV/Vis before and after ligand exchange.



Photocurrent before and after ligand exchange

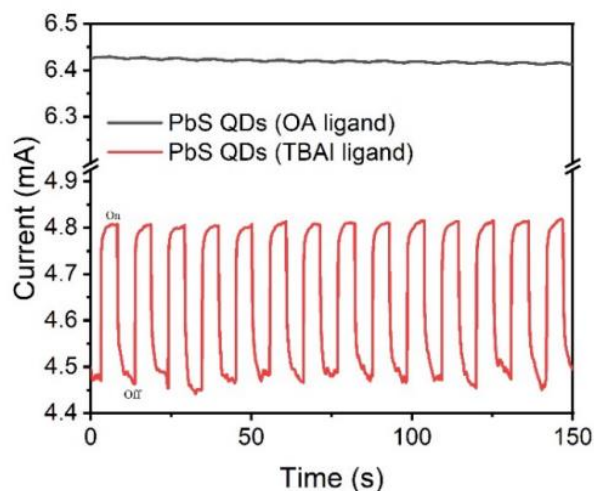


Figure 61 UV/Vis absorption and photocurrent before and after ligand exchange from oleic acid (OA) to TBAI. Ligand exchange is crucial to facilitate the charge transport along the QD film and therefore the charge collection by the SLG. The ligand exchange induces a red-shift in the absorption. However, the photocurrent is drastically improved after the ligand exchange, showing the importance of the surface ligands ligand exchange.

#### Optoelectronic characterization

The power of  $\lambda=635$  nm and 1.2 mW laser diode (CPS635R, Thorlabs) was measured by a standard silicon photodetector (S120VC, Thorlabs). The power intensity of the laser was achieved by absorptive neutral density filters (NE503A, NE510A, NE520A, and NE530A, Thorlabs). Current-voltage and current-time data were measured through a Keithley 2400 source meter. Noise measurements for detectivity were extracted from RMS noise of dark current traces. Spectral response was measured using a Keithley 2400 source meter under a 500 Watts MercuryXenon lamp and filters (66485-500HX-R1, USFW-100, Newport) with a monochromator (CS260-RG-3-FH-D,

Newport). Materials Characterization The vibrational modes of PbS QDs were analyzed by FTIR spectroscopy (Nicolet 6700). The structural information of Gr was carefully investigated by employing Raman spectroscopy (Renishaw). The absorption spectra of PbS QDs are analyzed by the UV-Vis spectroscopy (UH4150, Hitachi).

Chapter 6, in full, is a reprint of the material as it appears in “High resolution patterning of PbS quantum dots/Graphene photodetectors with high responsivity via photolithography with graphene passivation layer”, Seungbae Ahn, Wenjun Chen, and Oscar Vazquez-Mena, *Nanoscale advance*, accepted. The dissertation author was the primary investigator and author of this paper.

## Bibliography

- [1] F. Zhuge, Z. Zheng, P. Luo, L. Lv, Y. Huang, H. Li, T. Zhai, *Advanced Materials Technologies* 2017, 2, 1700005.
- [2] Z. Huang, J. E. Carey, M. Liu, X. Guo, E. Mazur, J. C. Campbell, *Applied Physics Letters* 2006, 89, 033506.
- [3] J. Wang, S. Lee, *Sensors (Basel)* 2011, 11, 696; S. S. Kang, D.-M. Geum, K. Kwak, J.-H. Kang, C.-H. Shim, H. Hyun, S. H. Kim, W. J. Choi, S.-H. Choi, M.-C. Park, J. D. Song, *Scientific Reports* 2019, 9, 12875; A. Rogalski, *Reports on Progress in Physics* 2005, 68, 2267.
- [4] N. Nasiri, A. Tricoli, in *Industrial Applications of Nanomaterials*, (Eds: S. Thomas, Y. Grohens, Y. B. Pottathara), Elsevier, 2019, 123.
- [5] N. Singh, R. M. Mehra, A. Kapoor, T. Soga, *Journal of Renewable and Sustainable Energy* 2012, 4, 013110; M. A. Hegazy, A. M. Abd El-Hameed, *NRIAG Journal of Astronomy and Geophysics* 2014, 3, 82; G. Shen, M. Chen, P. Guyot-Sionnest, *The Journal of Physical Chemistry Letters* 2017, 8, 2224; J. M. Pietryga, R. D. Schaller, D. Werder, M. H. Stewart, V. I. Klimov, J. A. Hollingsworth, *Journal of the American Chemical Society* 2004, 126, 11752.
- [6] I. Moreels, K. Lambert, D. Smeets, D. De Muynck, T. Nollet, J. C. Martins, F. Vanhaecke, A. Vantomme, C. Delerue, G. Allan, Z. Hens, *ACS Nano* 2009, 3, 3023.
- [7] P. N. Goswami, D. Mandal, A. K. Rath, *Nanoscale* 2018, 10, 1072.
- [8] O. Lopez-Sanchez, D. Lembke, M. Kayci, A. Radenovic, A. Kis, *Nature Nanotechnology* 2013, 8, 497.
- [9] X. Song, Y. Zhang, H. Zhang, Y. Yu, M. Cao, Y. Che, H. T. Dai, J. Yang, X. Ding, J. Yao, *Nanotechnology* 2021.
- [10] Y. Zhang, M. Cao, X. Song, J. Wang, Y. Che, H. Dai, X. Ding, G. Zhang, J. Yao, *The Journal of Physical Chemistry C* 2015, 119, 21739.
- [11] D. Zhang, L. Gan, Y. Cao, Q. Wang, L. Qi, X. Guo, *Adv Mater* 2012, 24, 2715.
- [12] S. Ahn, H. Chung, W. Chen, M. A. Moreno-Gonzalez, O. Vazquez-Mena, *The Journal of Chemical Physics* 2019, 151, 234705.
- [13] G. Konstantatos, M. Badioli, L. Gaudreau, J. Osmond, M. Bernechea, F. P. G. de Arquer, F. Gatti, F. H. L. Koppens, *Nature Nanotechnology* 2012, 7, 363.

- [14] C. Xie, C. Mak, X. Tao, F. Yan, *Advanced Functional Materials* 2017, 27, 1603886.
- [15] D. Kufer, G. Konstantatos, *ACS Photonics* 2016, 3, 2197.
- [16] Z. Yin, H. Li, H. Li, L. Jiang, Y. Shi, Y. Sun, G. Lu, Q. Zhang, X. Chen, H. Zhang, *ACS Nano* 2012, 6, 74.
- [17] H. Liu, Y. Liu, D. Zhu, *Journal of Materials Chemistry* 2011, 21, 3335; Z.-S. Wu, G. Zhou, L.-C. Yin, W. Ren, F. Li, H.-M. Cheng, *Nano Energy* 2012, 1, 107.
- [18] W. Chen, J. Castro, S. Ahn, X. Li, O. Vazquez-Mena, *Advanced Materials* 2019, 31, 1807894.
- [19] B. D. Boruah, A. Misra, *RSC Advances* 2015, 5, 90838; M. J. Grotevent, C. U. Hail, S. Yakunin, D. Bachmann, M. Calame, D. Poulidakos, M. V. Kovalenko, I. Shorubalko, *Advanced Science* 2021, 8, 2003360.
- [20] F. W. Wise, *Accounts of Chemical Research* 2000, 33, 773.
- [21] A. Kongkanand, K. Tvrđy, K. Takechi, M. Kuno, P. V. Kamat, *Journal of the American Chemical Society* 2008, 130, 4007.
- [22] L. Cademartiri, E. Montanari, G. Calestani, A. Migliori, A. Guagliardi, G. A. Ozin, *Journal of the American Chemical Society* 2006, 128, 10337.
- [23] L. Bakueva, S. Musikhin, M. A. Hines, T.-W. F. Chang, M. Tzolov, G. D. Scholes, E. H. Sargent, *Applied Physics Letters* 2003, 82, 2895.
- [24] I. Robel, V. Subramanian, M. Kuno, P. V. Kamat, *Journal of the American Chemical Society* 2006, 128, 2385; J. M. Caruge, J. E. Halpert, V. Wood, V. Bulović, M. G. Bawendi, *Nature Photonics* 2008, 2, 247.
- [25] I. L. Medintz, H. T. Uyeda, E. R. Goldman, H. Mattoussi, *Nature Materials* 2005, 4, 435.
- [26] I. Moreels, Y. Justo, B. De Geyter, K. Haestraete, J. C. Martins, Z. Hens, *ACS Nano* 2011, 5, 2004; I. Kang, F. W. Wise, *J. Opt. Soc. Am. B* 1997, 14, 1632.
- [27] J. M. Luther, J. Gao, M. T. Lloyd, O. E. Semonin, M. C. Beard, A. J. Nozik, *Advanced Materials* 2010, 22, 3704.
- [28] S. A. McDonald, G. Konstantatos, S. Zhang, P. W. Cyr, E. J. D. Klem, L. Levina, E. H. Sargent, *Nature Materials* 2005, 4, 138.

- [29] S. Chinnathambi, N. Shirahata, *Science and Technology of Advanced Materials* 2019, 20, 337; A. Benayas, F. Ren, E. Carrasco, V. Marzal, B. del Rosal, B. A. Gonfa, Á. Juarranz, F. Sanz-Rodríguez, D. Jaque, J. García-Solé, D. Ma, F. Vetrone, *Advanced Functional Materials* 2015, 25, 6650.
- [30] C.-H. M. Chuang, P. R. Brown, V. Bulović, M. G. Bawendi, *Nature Materials* 2014, 13, 796.
- [31] A. Stavrinadis, S. Pradhan, P. Papagiorgis, G. Itskos, G. Konstantatos, *ACS Energy Letters* 2017, 2, 739.
- [32] X. Lan, O. Voznyy, F. P. García de Arquer, M. Liu, J. Xu, A. H. Proppe, G. Walters, F. Fan, H. Tan, M. Liu, Z. Yang, S. Hoogland, E. H. Sargent, *Nano Letters* 2016, 16, 4630.
- [33] J. Xu, O. Voznyy, M. Liu, A. R. Kirmani, G. Walters, R. Munir, M. Abdelsamie, A. H. Proppe, A. Sarkar, F. P. García de Arquer, M. Wei, B. Sun, M. Liu, O. Ouellette, R. Quintero-Bermudez, J. Li, J. Fan, L. Quan, P. Todorovic, H. Tan, S. Hoogland, S. O. Kelley, M. Stefiak, A. Amassian, E. H. Sargent, *Nature Nanotechnology* 2018, 13, 456.
- [34] Z. Sun, Z. Liu, J. Li, G.-a. Tai, S.-P. Lau, F. Yan, *Advanced Materials* 2012, 24, 5878.
- [35] I. Nikitskiy, S. Goossens, D. Kufer, T. Lasanta, G. Navickaite, F. H. L. Koppens, G. Konstantatos, *Nature Communications* 2016, 7, 11954.
- [36] G. Konstantatos, E. H. Sargent, *Infrared Physics & Technology* 2011, 54, 278.
- [37] X. Lan, S. Masala, E. H. Sargent, *Nature Materials* 2014, 13, 233; J. Tang, E. H. Sargent, *Advanced Materials* 2011, 23, 12.
- [38] D. Zhitomirsky, O. Voznyy, S. Hoogland, E. H. Sargent, *ACS Nano* 2013, 7, 5282.
- [39] G. H. Carey, L. Levina, R. Comin, O. Voznyy, E. H. Sargent, *Advanced Materials* 2015, 27, 3325.
- [40] J. Zhang, R. W. Crisp, J. Gao, D. M. Kroupa, M. C. Beard, J. M. Luther, *The Journal of Physical Chemistry Letters* 2015, 6, 1830.
- [41] G. Borin Barin, Y. Song, I. de Fátima Gimenez, A. G. Souza Filho, L. S. Barreto, J. Kong, *Carbon* 2015, 84, 82.
- [42] S. Abe, R. K. Capek, B. De Geyter, Z. Hens, *ACS Nano* 2013, 7, 943.

- [43] L. Yuan, R. Patterson, W. Cao, Z. Zhang, Z. Zhang, J. A. Stride, P. Reece, G. Conibeer, S. Huang, *RSC Advances* 2015, 5, 68579.
- [44] U. Holzwarth, N. Gibson, *Nature Nanotechnology* 2011, 6, 534.
- [45] D. F. Swinehart, *Journal of Chemical Education* 1962, 39, 333.
- [46] C. Yim, M. O'Brien, N. McEvoy, S. Winters, I. Mirza, J. G. Lunney, G. S. Duesberg, *Applied Physics Letters* 2014, 104, 103114.
- [47] F. P. Koffyberg, K. Dwight, A. Wold, *Solid State Communications* 1979, 30, 433.
- [48] F. P. G. d. Arquer, D. V. Talapin, V. I. Klimov, Y. Arakawa, M. Bayer, E. H. Sargent, *Science* 2021, 373, eaaz8541; A. K. Rath, M. Bernechea, L. Martinez, G. Konstantatos, *Advanced Materials* 2011, 23, 3712; Y. Cao, A. Stavriniadis, T. Lasanta, D. So, G. Konstantatos, *Nature Energy* 2016, 1, 16035; E. H. Sargent, *Nature Photonics* 2012, 6, 133; S. Pradhan, M. Dalmases, A.-B. Baspinar, G. Konstantatos, *Advanced Functional Materials* 2020, 30, 2004445; S. Pradhan, F. Di Stasio, Y. Bi, S. Gupta, S. Christodoulou, A. Stavriniadis, G. Konstantatos, *Nature Nanotechnology* 2019, 14, 72; V. Adinolfi, E. H. Sargent, *Nature* 2017, 542, 324; G. Konstantatos, I. Howard, A. Fischer, S. Hoogland, J. Clifford, E. Klem, L. Levina, E. H. Sargent, *Nature* 2006, 442, 180.
- [49] B.-S. Kim, D. C. J. Neo, B. Hou, J. B. Park, Y. Cho, N. Zhang, J. Hong, S. Pak, S. Lee, J. I. Sohn, H. E. Assender, A. A. R. Watt, S. Cha, J. M. Kim, *ACS Applied Materials & Interfaces* 2016, 8, 13902.
- [50] J. P. Clifford, G. Konstantatos, K. W. Johnston, S. Hoogland, L. Levina, E. H. Sargent, *Nature Nanotechnology* 2009, 4, 40.
- [51] R. Saran, R. J. Curry, *Nature Photonics* 2016, 10, 81.
- [52] K. J. Williams, W. A. Tisdale, K. S. Leschkies, G. Haugstad, D. J. Norris, E. S. Aydil, X. Y. Zhu, *ACS Nano* 2009, 3, 1532.
- [53] K. S. Jeong, J. Tang, H. Liu, J. Kim, A. W. Schaefer, K. Kemp, L. Levina, X. Wang, S. Hoogland, R. Debnath, L. Brzozowski, E. H. Sargent, J. B. Asbury, *ACS Nano* 2012, 6, 89.
- [54] Y. Liu, M. Gibbs, J. Puthussery, S. Gaik, R. Ihly, H. W. Hillhouse, M. Law, *Nano Letters* 2010, 10, 1960.
- [55] D. Zhitomirsky, O. Voznyy, L. Levina, S. Hoogland, K. W. Kemp, A. H. Ip, S. M. Thon, E. H. Sargent, *Nature Communications* 2014, 5, 3803; E. M. Y. Lee, W. A. Tisdale, *The Journal of Physical Chemistry C* 2015, 119, 9005; D. D. Wanger, R. E. Correa, E. A. Dauler, M. G. Bawendi,

Nano Letters 2013, 13, 5907; Y. J. Jeong, J. Jang, J. H. Song, H. Choi, S. Jeong, S. J. Baik, J. Opt. Soc. Korea 2015, 19, 272; P. H. Rekemeyer, C.-H. M. Chuang, M. G. Bawendi, S. Gradečak, Nano Letters 2017, 17, 6221.

[56] L. Turyanska, O. Makarovskiy, S. A. Svatek, P. H. Beton, C. J. Mellor, A. Patané, L. Eaves, N. R. Thomas, M. W. Fay, A. J. Marsden, N. R. Wilson, *Advanced Electronic Materials* 2015, 1, 1500062.

[57] X. Song, Y. Zhang, H. Zhang, Y. Yu, M. Cao, Y. Che, H. Dai, J. Yang, X. Ding, J. Yao, *Nanotechnology* 2017, 28, 145201.

[58] C. Ingrosso, G. V. Bianco, M. Corricelli, R. Comparelli, D. Altamura, A. Agostiano, M. Striccoli, M. Losurdo, M. L. Curri, G. Bruno, *ACS Applied Materials & Interfaces* 2015, 7, 4151.

[59] A. Sahoo, P. Reiss, E. Quesnel, B. Hyot, *Nanotechnology* 2021, 32, 405205.

[60] R. Dutta, A. Pradhan, P. Mondal, S. Kakkar, T. P. Sai, A. Ghosh, J. K. Basu, *ACS Applied Materials & Interfaces* 2021, 13, 24295.

[61] K. W. Kemp, C. T. O. Wong, S. H. Hoogland, E. H. Sargent, *Applied Physics Letters* 2013, 103, 211101.

[62] D. V. Talapin, C. B. Murray, *Science* 2005, 310, 86.

[63] J.-H. Choi, A. T. Fafarman, S. J. Oh, D.-K. Ko, D. K. Kim, B. T. Diroll, S. Muramoto, J. G. Gillen, C. B. Murray, C. R. Kagan, *Nano Letters* 2012, 12, 2631; Y. Gao, M. Aerts, C. S. S. Sandeep, E. Talgorn, T. J. Savenije, S. Kinge, L. D. A. Siebbeles, A. J. Houtepen, *ACS Nano* 2012, 6, 9606.

[64] I. Moreels, K. Lambert, D. De Muynck, F. Vanhaecke, D. Poelman, J. C. Martins, G. Allan, Z. Hens, *Chemistry of Materials* 2007, 19, 6101.

[65] C. Xia, W. Wu, T. Yu, X. Xie, C. van Oversteeg, H. C. Gerritsen, C. de Mello Donega, *ACS Nano* 2018, 12, 8350.

[66] K. S. Novoselov, A. K. Geim, S. V. Morozov, D. Jiang, Y. Zhang, S. V. Dubonos, I. V. Grigorieva, A. A. Firsov, *Science* 2004, 306, 666; K. S. Novoselov, A. K. Geim, S. V. Morozov, D. Jiang, M. I. Katsnelson, I. V. Grigorieva, S. V. Dubonos, A. A. Firsov, *Nature* 2005, 438, 197; K. S. Novoselov, V. I. Fal'ko, L. Colombo, P. R. Gellert, M. G. Schwab, K. Kim, *Nature* 2012, 490, 192; A. S. Mayorov, R. V. Gorbachev, S. V. Morozov, L. Britnell, R. Jalil, L. A. Ponomarenko, P. Blake, K. S. Novoselov, K. Watanabe, T. Taniguchi, A. K. Geim, *Nano Letters* 2011, 11, 2396; D. S. L. Abergel, V. Apalkov, J. Berashevich, K. Ziegler, T. Chakraborty, *Advances in Physics* 2010, 59, 261;

- J. Zheng, X. Xu, Y. Zhang, Q. Xie, X. Wu, K. Yu, W. Wei, *Thin Solid Films* 2020, 709, 138129.
- [67] F. Bonaccorso, Z. Sun, T. Hasan, A. C. Ferrari, *Nature Photonics* 2010, 4, 611.
- [68] C. B. M. and, C. R. Kagan, M. G. Bawendi, *Annual Review of Materials Science* 2000, 30, 545; Y. Yin, A. P. Alivisatos, *Nature* 2005, 437, 664; G. Konstantatos, E. H. Sargent, *Nature Nanotechnology* 2010, 5, 391; H. Zhao, T. Zhang, M. Chaker, D. Ma, *Journal of Nanoscience and Nanotechnology* 2010, 10, 4897.
- [69] D. Zhang, L. Gan, Y. Cao, Q. Wang, L. Qi, X. Guo, *Advanced Materials* 2012, 24, 2715.
- [70] W. Chen, S. Ahn, C. Rangel, O. Vazquez-Mena, *Frontiers in Materials* 2019, 6.
- [71] W. Chen, S. Ahn, M. Balingit, J. Wang, M. Lockett, O. Vazquez-Mena, *Nanoscale* 2020, 12, 4909.
- [72] W. Ouyang, J. Chen, J.-H. He, X. Fang, *Advanced Electronic Materials* 2020, 6, 2000168; R. Tang, S. Han, F. Teng, K. Hu, Z. Zhang, M. Hu, X. Fang, *Advanced Science* 2018, 5, 1700334; N. Gao, X. Fang, *Chemical Reviews* 2015, 115, 8294.
- [73] S. Ahn, W. Chen, M. A. Moreno-Gonzalez, M. Lockett, J. Wang, O. Vazquez-Mena, *Advanced Electronic Materials* 2020, 6, 2000014.
- [74] D. Kufer, T. Lasanta, M. Bernechea, F. H. L. Koppens, G. Konstantatos, *ACS Photonics* 2016, 3, 1324.
- [75] P. R. Brown, D. Kim, R. R. Lunt, N. Zhao, M. G. Bawendi, J. C. Grossman, V. Bulović, *ACS Nano* 2014, 8, 5863.
- [76] O. Voznyy, D. Zhitomirsky, P. Stadler, Z. Ning, S. Hoogland, E. H. Sargent, *ACS Nano* 2012, 6, 8448; S. J. Oh, N. E. Berry, J.-H. Choi, E. A. Gaulding, T. Paik, S.-H. Hong, C. B. Murray, C. R. Kagan, *ACS Nano* 2013, 7, 2413.
- [77] D. Kufer, I. Nikitskiy, T. Lasanta, G. Navickaite, F. H. L. Koppens, G. Konstantatos, *Advanced Materials* 2015, 27, 176.
- [78] Q. Nian, L. Gao, Y. Hu, B. Deng, J. Tang, G. J. Cheng, *ACS Appl Mater Interfaces* 2017, 9, 44715.
- [79] N. Huo, S. Gupta, G. Konstantatos, *Advanced Materials* 2017, 29, 1606576.
- [80] S. Goossens, G. Navickaite, C. Monasterio, S. Gupta, J. J. Piqueras, R. Pérez, G. Burwell,



I. Nikitskiy, T. Lasanta, T. Galán, E. Puma, A. Centeno, A. Pesquera, A. Zurutuza, G. Konstantatos, F. Koppens, *Nature Photonics* 2017, 11, 366.

[81] W. Chen, J. Castro, S. Ahn, X. Li, O. Vazquez-Mena, *Adv Mater* 2019, 31, e1807894.

[82] S. Ahn, W. Chen, O. Vasquez-Mena, *Nanoscale Advances* 2021.

[83] X. Peng, J. Wickham, A. P. Alivisatos, *Journal of the American Chemical Society* 1998, 120, 5343.

[84] G. Katsukis, J. Malig, C. Schulz-Drost, S. Leubner, N. Jux, D. M. Guldi, *ACS Nano* 2012, 6, 1915.

[85] T. Hanrath, D. Veldman, J. J. Choi, C. G. Christova, M. M. Wienk, R. A. J. Janssen, *ACS Applied Materials & Interfaces* 2009, 1, 244; M. Law, J. M. Luther, Q. Song, B. K. Hughes, C. L. Perkins, A. J. Nozik, *Journal of the American Chemical Society* 2008, 130, 5974.

[86] I. S. Liu, H.-H. Lo, C.-T. Chien, Y.-Y. Lin, C.-W. Chen, Y.-F. Chen, W.-F. Su, S.-C. Liou, *Journal of Materials Chemistry* 2008, 18, 675.

[87] A. C. Ferrari, J. C. Meyer, V. Scardaci, C. Casiraghi, M. Lazzeri, F. Mauri, S. Piscanec, D. Jiang, K. S. Novoselov, S. Roth, A. K. Geim, *Physical Review Letters* 2006, 97, 187401.

[88] L. Li, X. Zheng, J. Wang, Q. Sun, Q. Xu, *ACS Sustainable Chemistry & Engineering* 2013, 1, 144; H. Shinohara, Y. Yamakita, K. Ohno, *Journal of Molecular Structure* 1998, 442, 221.

[89] C. Ingrosso, G. V. Bianco, V. Pifferi, P. Guffanti, F. Petronella, R. Comparelli, A. Agostiano, M. Striccoli, I. Palchetti, L. Falciola, M. L. Curri, G. Bruno, *Journal of Materials Chemistry A* 2017, 5, 9307.

[90] A. A. Ganesan, A. J. Houtepen, R. W. Crisp, *Applied Sciences* 2018, 8, 1867.

[91] Y.-J. Yu, Y. Zhao, S. Ryu, L. E. Brus, K. S. Kim, P. Kim, *Nano Letters* 2009, 9, 3430.

[92] R. D. Harris, S. Bettis Homan, M. Kodaimati, C. He, A. B. Nepomnyashchii, N. K. Swenson, S. Lian, R. Calzada, E. A. Weiss, *Chemical Reviews* 2016, 116, 12865.

[93] E. T. Vickers, T. A. Graham, A. H. Chowdhury, B. Bahrami, B. W. Dreskin, S. Lindley, S. B. Naghadeh, Q. Qiao, J. Z. Zhang, *ACS Energy Letters* 2018, 3, 2931.

[94] G. Konstantatos, L. Levina, A. Fischer, E. H. Sargent, *Nano Letters* 2008, 8, 1446.

- [95] Q. Nian, L. Gao, Y. Hu, B. Deng, J. Tang, G. J. Cheng, *ACS Applied Materials & Interfaces* 2017, 9, 44715; B. Yang, J. Chen, L. Cui, W. Liu, *RSC Advances* 2015, 5, 59204.
- [96] P. A. George, J. Strait, J. Dawlaty, S. Shivaraman, M. Chandrashekhar, F. Rana, M. G. Spencer, *Nano Letters* 2008, 8, 4248.
- [97] C. Ingrosso, M. Corricelli, F. Bettazzi, E. Konstantinidou, G. V. Bianco, N. Depalo, M. Striccoli, A. Agostiano, M. L. Curri, I. Palchetti, *Journal of Materials Chemistry B* 2019, 7, 768.
- [98] R. X. He, P. Lin, Z. K. Liu, H. W. Zhu, X. Z. Zhao, H. L. W. Chan, F. Yan, *Nano Letters* 2012, 12, 1404.
- [99] T. Mueller, F. Xia, P. Avouris, *Nature Photonics* 2010, 4, 297.
- [100] R. D. Jansen-van Vuuren, A. Armin, A. K. Pandey, P. L. Burn, P. Meredith, *Advanced Materials* 2016, 28, 4766.
- [101] D. Pan, E. Towe, S. Kennerly, *Applied Physics Letters* 1998, 73, 1937; F. González-Posada, R. Songmuang, M. Den Hertog, E. Monroy, *Nano Letters* 2012, 12, 172; X. Gong, M. Tong, Y. Xia, W. Cai, J. S. Moon, Y. Cao, G. Yu, C.-L. Shieh, B. Nilsson, A. J. Heeger, *Science* 2009, 325, 1665; R. Tang, S. Han, F. Teng, K. Hu, Z. Zhang, M. Hu, X. Fang, *Adv Sci (Weinh)* 2018, 5, 1700334; W. Ouyang, F. Teng, J.-H. He, X. Fang, *Advanced Functional Materials* 2019, 29, 1807672; A. K. Rana, M. Kumar, D.-K. Ban, C.-P. Wong, J. Yi, J. Kim, *Advanced Electronic Materials* 2019, 5, 1900438; W. Ouyang, F. Teng, M. Jiang, X. Fang, *Small* 2017, 13, 1702177; Y. Zhang, X. Zhao, J. Chen, S. Li, W. Yang, X. Fang, *Advanced Functional Materials* 2020, 30, 1907650; K. Hu, F. Teng, L. Zheng, P. Yu, Z. Zhang, H. Chen, X. Fang, *Laser & Photonics Reviews* 2017, 11, 1600257; Z. Long, X. Xu, W. Yang, M. Hu, D. V. Shtansky, D. Golberg, X. Fang, *Advanced Electronic Materials* 2020, 6, 1901048.
- [102] K. Deng, L. Li, *Advanced Materials* 2014, 26, 2619.
- [103] H. Tan, Y. Fan, Y. Zhou, Q. Chen, W. Xu, J. H. Warner, *ACS Nano* 2016, 10, 7866.
- [104] D. H. Shin, S.-H. Choi, *Micromachines* 2018, 9, 350.
- [105] C. Xie, F. Yan, *ACS Applied Materials & Interfaces* 2017, 9, 1569.
- [106] Z. Zhang, H. Huang, X. Yang, L. Zang, *The Journal of Physical Chemistry Letters* 2011, 2, 2897; L. Hu, D.-B. Li, L. Gao, H. Tan, C. Chen, K. Li, M. Li, J.-B. Han, H. Song, H. Liu, J. Tang, *Advanced Functional Materials* 2016, 26, 1899.
- [107] P. Xu, Q. Tang, Z. Zhou, *Nanotechnology* 2013, 24, 305401.

- [108] S. Pak, Y. Cho, J. Hong, J. Lee, S. Lee, B. Hou, G.-H. An, Y.-W. Lee, J. E. Jang, H. Im, S. M. Morris, J. I. Sohn, S. Cha, J. M. Kim, *ACS Applied Materials & Interfaces* 2018, 10, 38264.
- [109] L. Gao, C. Chen, K. Zeng, C. Ge, D. Yang, H. Song, J. Tang, *Light: Science & Applications* 2016, 5, e16126.
- [110] M. Peng, X. Xie, H. Zheng, Y. Wang, Q. Zhuo, G. Yuan, W. Ma, M. Shao, Z. Wen, X. Sun, *ACS Appl Mater Interfaces* 2018, 10, 43887.
- [111] D. K. Hwang, Y. T. Lee, H. S. Lee, Y. J. Lee, S. H. Shokouh, J.-h. Kyhm, J. Lee, H. H. Kim, T.-H. Yoo, S. H. Nam, D. I. Son, B.-K. Ju, M.-C. Park, J. D. Song, W. K. Choi, S. Im, *NPG Asia Materials* 2016, 8, e233.
- [112] Z. Ren, J. Sun, H. Li, P. Mao, Y. Wei, X. Zhong, J. Hu, S. Yang, J. Wang, *Advanced Materials* 2017, 29, 1702055.
- [113] C. H. Chuang, P. R. Brown, V. Bulović, M. G. Bawendi, *Nat Mater* 2014, 13, 796; C. Pacholski, A. Kornowski, H. Weller, *Angew Chem Int Ed Engl* 2002, 41, 1188.
- [114] X. Li, W. Cai, J. An, S. Kim, J. Nah, D. Yang, R. Piner, A. Velamakanni, I. Jung, E. Tutuc, S. K. Banerjee, L. Colombo, R. S. Ruoff, *Science* 2009, 324, 1312.
- [115] A. P. Litvin, I. V. Martynenko, F. Purcell-Milton, A. V. Baranov, A. V. Fedorov, Y. K. Gun'ko, *Journal of Materials Chemistry A* 2017, 5, 13252; J. M. Pietryga, Y.-S. Park, J. Lim, A. F. Fidler, W. K. Bae, S. Brovelli, V. I. Klimov, *Chemical Reviews* 2016, 116, 10513; S. B. Hafiz, M. Scimeca, A. Sahu, D.-K. Ko, *Nano Convergence* 2019, 6, 7; S. Gunapala, S. Bandara, C. Hill, D. Ting, J. Liu, S. Rafol, E. Blazejewski, J. Mumolo, S. Keo, S. Krishna, Y. Chang, C. Shott, *Long-wavelength infrared (LWIR) quantum dot infrared photodetector (QDIP) focal plane array*, Vol. 6206, SPIE, 2006.
- [116] C. R. Kagan, E. Lifshitz, E. H. Sargent, D. V. Talapin, *Science* 2016, 353, aac5523.
- [117] R. Wang, Y. Shang, P. Kanjanaboos, W. Zhou, Z. Ning, E. H. Sargent, *Energy & Environmental Science* 2016, 9, 1130; H. Moon, C. Lee, W. Lee, J. Kim, H. Chae, *Advanced Materials* 2019, 31, 1804294.
- [118] G. Azzellino, F. S. Freyria, M. Nasilowski, M. G. Bawendi, V. Bulović, *Advanced Materials Technologies* 2019, 4, 1800727; S. Biswas, F. Brinkmann, M. Hirtz, H. Fuchs, *Nanofabrication* 2015, 2, 19; H. Keum, Y. Jiang, J. K. Park, J. C. Flanagan, M. Shim, S. Kim, *ACS Nano* 2018, 12, 10024; C. D. Dieleman, W. Ding, L. Wu, N. Thakur, I. Bepalov, B. Daiber, Y. Ekinci, S. Castellanos, B. Ehrler, *Nanoscale* 2020, 12, 11306.

- [119] J. Yang, D. Hahm, K. Kim, S. Rhee, M. Lee, S. Kim, J. H. Chang, H. W. Park, J. Lim, M. Lee, H. Kim, J. Bang, H. Ahn, J. H. Cho, J. Kwak, B. Kim, C. Lee, W. K. Bae, M. S. Kang, *Nature Communications* 2020, 11, 2874; W. Zhou, L. Zheng, X. Cheng, W. Zhou, X. Xiao, K. Xu, W. Xin, P. Ye, Y. Yu, *Journal of Materials Science: Materials in Electronics* 2020, 31, 5900.
- [120] M. A. Foad, C. D. W. Wilkinson, C. Dunscomb, R. H. Williams, *Applied Physics Letters* 1992, 60, 2531; G. Yang, B. Weng, *Materials Science in Semiconductor Processing* 2021, 124, 105596.
- [121] S. Ayneband, M. Mohammadi, K. Thorwarth, R. Hany, F. A. Nüesch, M. D. Rossell, R. Pauer, J.-M. Nunzi, A. Simchi, *ACS Omega* 2020, 5, 15746.
- [122] B.-S. Kim, J. Hong, B. Hou, Y. Cho, J. I. Sohn, S. Cha, J. M. Kim, *Applied Physics Letters* 2016, 109, 063901.
- [123] G. Konstantatos, J. Clifford, L. Levina, E. H. Sargent, *Nature Photonics* 2007, 1, 531.